Investigation of Grinding Wheel Wear Using a White Chromatic Sensor

by

Andrew McDonald

Submitted in partial fulfilment of the requirements
for the degree of Master of Applied Science

at

Dalhousie University
Halifax, Nova Scotia
December 2015

Table of Contents

List of Tables

List of Figures

vii

Abstract

This thesis involves the measuring of grinding wheel wear using an improved grinding wheel scanner. The positional resolution of the scanner has been improved from 26.5 μm to 0.65 μm with the addition of a second encoder. A vision based homing system was designed, and is able to track the position of the grinding wheel with a resolution of 2 μm. The implementation of a real-time controller improved the reliability of component synchronization and data acquisition. A slip compensation algorithm was written to correct the slip between grinding and friction wheels. The algorithm was proven to be able to compensate the slip to within the resolution of the sensor used. The positional repeatability of the scanner was measured to have average percent differences of 1.3% and 0.8% for the x and y directions, respectively. The homing system was measured to be repeatable within standard deviations of 27.6 μm and 19.3 μm for the x and y directions, respectively. The grinding wheel scanner measurements were then compared to SEM images and the surface areas of distinct features were measured to be within 11% of one another. The scanner was then used to study the wear of non-grooved and grooved grinding wheels. Analysis methods were developed to consistently extract parameters from the measured wheel surface. The extracted parameters were then used to calculate the G-ratios for the non-grooved and grooved wheels, which were found to be 6849 and 10215, respectively during steady state wear. A comparison of the power and forces to the uncut chip thickness was able to show the effect of the failure modes and clearly represented the size effect.

List of Abbreviations and Symbols Used

SEM   Scanning Electron Microscope

ANSI   American National Standards Institute

CBN   Cubic Boron Nitride

M Grit number

d_g grain diameter

d_s wheel diameter

v_s wheel velocity

v_w workpiece velocity

a depth of cut

l_c contact length

h_m uncut chip thickness

L grain spacing

CMM   Coordinate Mapping Machine

WLI   White Light Interferometer

CPR   Counts Per Revolution

s arc length

r arc radius

θ central angle

WD   Working Distance

FOV   Field of View

Pmag   Primary Magnification

α search line angle

cRIO   Compact Reconfigurable I/O

FPGA   Field Programmable Gate Arrays

RT   Real-Time

QR   Quick Response

Ra	Arithmetic average
x_f	x-direction feature distance
y_f	y-direction feature distance
D_f	total feature distance
φ	feature angle
σ	standard deviation
b_p	particle width
C	cutting edge density

Acknowledgements

I am very thankful for everyone who has helped with my research and would like to take this opportunity to thank them. First and foremost, I want to thank my supervisors, Dr. Andrew Warkentin and Dr. Robert Bauer for their guidance and constant encouragement throughout my time at Dalhousie. I simply would not have had the same experience here if it weren't for them. I would also like to thank Dr. Ted Hubbard and Dr. Stephen Corbin for providing me with their expertise and time by agreeing to be on my examining committee.

Many thanks go to my colleague and friend, Al-Mokhtar Mohamed for never hesitating to assist me, and for his considerable help during the experimental stage of my work. I would also like to thank the Mechanical Engineering staff, namely Peter Jones and Jon MacDonald who were always pleasant in dealing with any issues that arose in my work.

Finally, I would like to thank my family and loved ones for their continuing support while I pursued this degree. I would not have been able to do it without them.

Chapter 1. Introduction

Grinding is a metal removal process, and as in any machining process, it involves the use of a tool to remove unwanted material from a workpiece. In grinding, the tool is a wheel that consists of very hard abrasive grains bonded together. Grinding plays an important role in manufacturing and is used to produce high quality parts with excellent surface finish and to close tolerances [1]. A very appealing aspect of grinding is its ability to machine a wide number of workpieces, especially hard and tough materials. Products that require grinding span nearly all aspects of everyday life from large turbine blades for an airplane engine to the prescription glasses that are worn by millions of people around world.

1.1 Motivation

In other machining processes the effect of tool geometry can be quantified. In grinding, the tool is the wheel itself, and due to the complexity of its microtopography it is very hard to define the geometry of the tool. It is known that the wheel's condition is directly related to the power, workpiece roughness and workpiece temperature but these relationships have not yet been fully quantified. In order to effectively study and understand the grinding wheels surface and its effect on the process outcomes, tools are needed that can monitor the changes in the wheels surface topography throughout the process.

1.2 Objectives

The objective of this thesis work was to:
- Improve the current grinding wheel scanner's resolution and reliability.
- Design and implement a homing system for the grinding wheel scanner.
- Quantify the improved scanner's repeatability and validate it's capability to accurately measure a grinding wheel surface.
- Investigate the wear of grooved and non-grooved grinding wheels using the improved grinding wheel scanner.

1.3 Organization of Thesis

This work contains 6 chapters. Chapter 2 will provide the essential grinding process information that is needed to follow the work of this thesis. It will cover the composition of a grinding wheel, the kinematics of the process and the types of grinding wheel wear mechanisms. Current grinding wheel surface characterization methods are then discussed. Chapter 3 describes the old grinding wheel scanner and discusses its issues. Solutions to these issues, which have been developed and implemented, are then described. Chapter 4 contains the validation of the modified scanner, beginning with the repeatability of 2D profile and 3D area scans of test surfaces. The scanners capability to measure the grinding wheel surface is then validated by comparing measurements to digital and scanning electron microscope (SEM) images. A comparison of ground and unground grains is also used for further validation. Chapter 5 contains a wear study which was performed to investigate the wear of grooved and non-grooved grinding wheels. An analysis method was developed in order to extract parameters from the scanner measurement. Comparisons of the two wheels' extracted parameters are then performed to quantify the differences in their wear. Chapter 6 then summarizes the work included in this thesis and offers recommendations for future work.

Chapter 2. Background and Literature Review

This chapter will serve as the foundation for the content covered throughout the entirety of this thesis. The essential topics which will be covered are the composition of grinding wheels, the kinematics of the grinding process, and common wheel wear mechanisms. Different methods for measuring grinding wheel topography will then be reviewed. The methods are separated into three categories contact, non-contact and in-process.

2.1 The Grinding Wheel

The grinding wheel is a key component in the grinding process as its surface acts as the cutting tool. Grinding wheels are made up of abrasive grains that are held together using a bonding material. In between the grains and bonding material there are spaces referred to as pores. The three aspects of a grinding wheel are clearly shown in Figure 2.1.
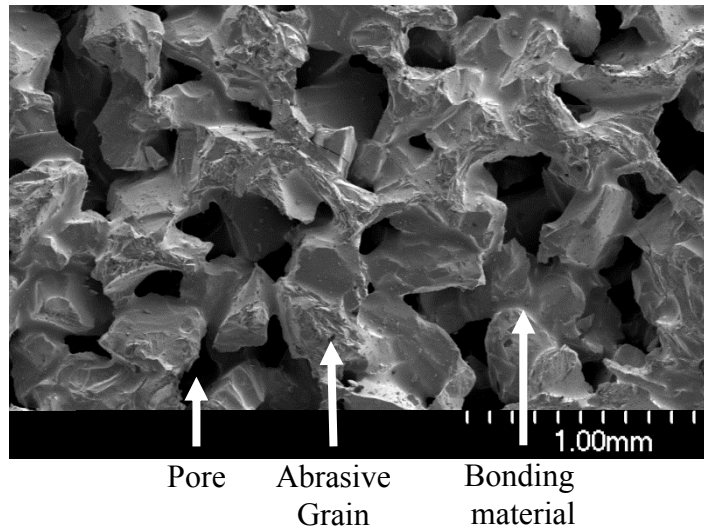
Figure 2.1 SEM of grinding wheel showing porous voids, abrasive grains and bonding material

Grinding wheels can be classified using an American National Standards Institute (ANSI) standardized marking system [2]. The marking system defines the wheel by its abrasive type, grade, structure and bond material. In Figure 2.1 the abrasive shown is an aluminum oxide which is the most common type used. Other abrasives that are typically used

consist of silicon carbide, cubic boron nitride (CBN) and diamond. The latter two are referred to as super-abrasives due to their superior hardness and resistance to wear. The size of the abrasive plays a large role in the surface finish and achievable material removal rates. Small grains generally produce a finer workpiece surface finish while large grains can increase the material removal rate [3]. The grain size is defined by a grit number M and can be used in the following relationship to estimate the average grain diameter d_g in *mm* [4].

$$d_g = 15.2M^{-1} \tag{2.1}$$

The most common bond type used in grinding wheels, and the type used throughout this thesis is a vitrified bond. The grade of a wheel refers to its hardness. The more bonding material, the harder a wheel is. The wheels structure indicates the amount of abrasive grains that are in the wheel.

2.2 Grinding Kinematics

The kinematics of grinding is illustrated in Figure 2.2 to show the basic geometrical relationship during chip formation. The grinding wheel of diameter d_s is rotated at a peripheral velocity v_s and brought into contact with the workpiece, which is translating at a velocity of v_w. The relative height difference between the bottom of the grinding wheel and unground workpiece surface is equal to the depth of cut a. The arc length formed between the wheel and workpiece is referred to as the contact length l_c. The feed per cutting point, f, is the horizontal distance that one grain travels while in the cutting zone. The combination of the wheel's rotating motion and workpiece's translating motion results in an increasing uncut chip thickness shown in black in Figure 2.2. The resulting maximum uncut chip thickness is represented as h_m.
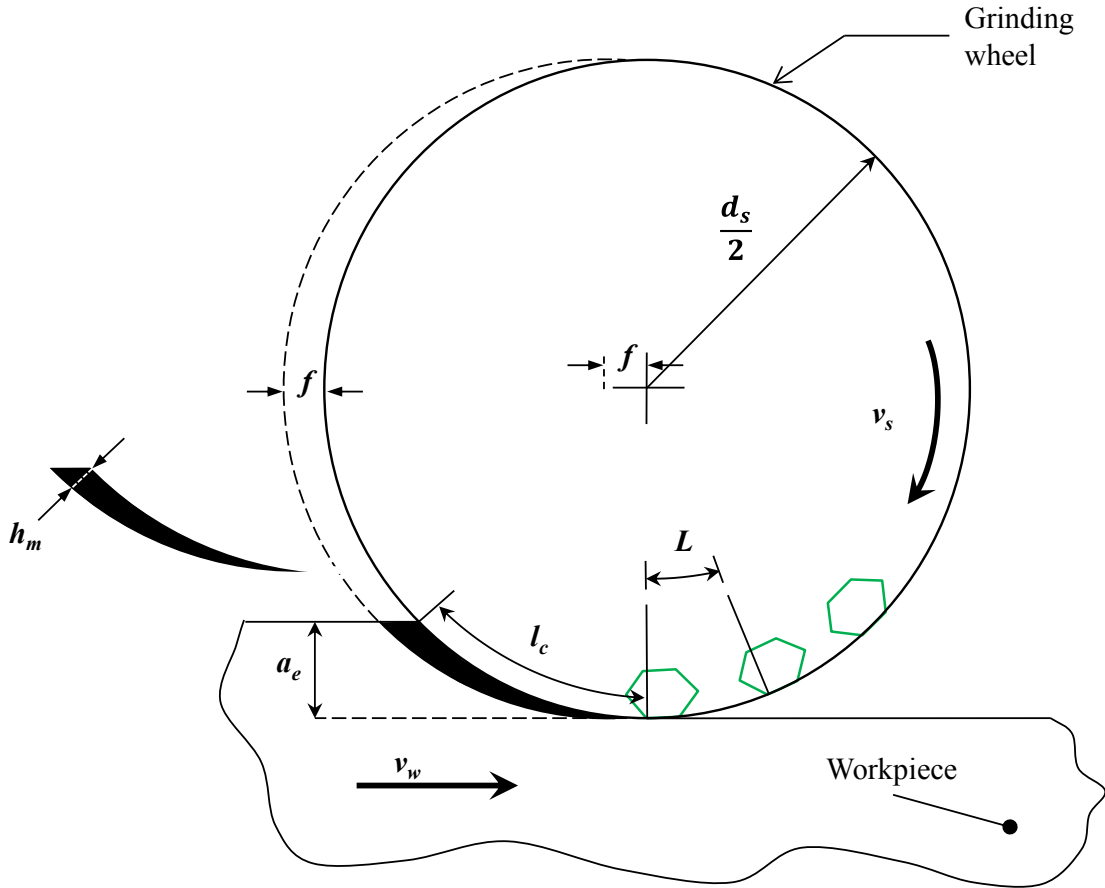
Figure 2.2 Illustration of grinding kinematics

The maximum uncut chip thickness can be calculated using Equation [4]. This equation was derived based on the assumption that the grains are all the same size, and have the same spacing and protrusion height. In reality the grains are known to be randomly spaced, sized, oriented and protruding from the wheel surface.

$$h_m = 2L \frac{v_w}{v_s} \left(\frac{a}{d_s}\right)^{\frac{1}{2}}$$

(2.2)

All of the terms in Equation (2.2) are seen depicted in Figure 2.2. All parameters except for the grain spacing L can be easily determined from the grinding kinematics. While

approximations of the grain spacing do exist, due to the complexity of the wheel's surface the only true way to obtain the parameter is from direct measurement.

2.3 Wear Mechanisms

The grinding of material inevitably leads to wheel wear. As the wheel wears, its geometry and therefore the geometry of the cutting tool changes, which can have a significant effect on the process outcomes. Important parameters such as grinding efficiency, workpiece surface finish and material properties are all affected by the wear [5]. There are three dominant wear mechanisms during the grinding process. They are attritious wear, grain fracture and bond fracture [6, 7, 8, 9]. The three mechanisms are shown in Figure 2.3.
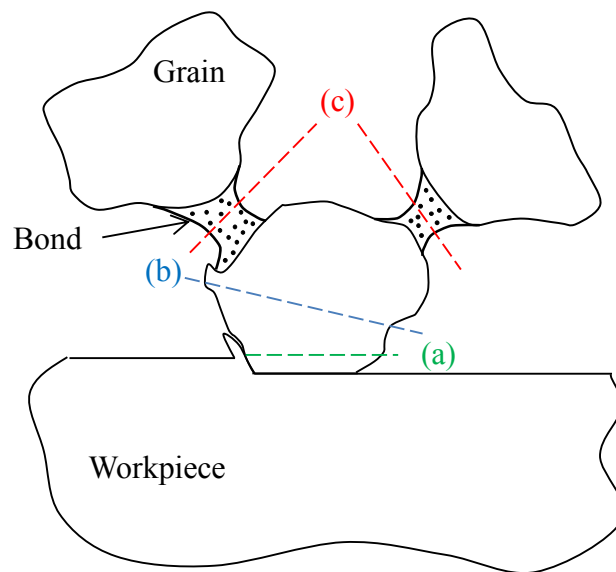
Figure 2.3 Illustration of wear mechanisms including; (a) attritious wear, (b) grain fracture and (c) bond fracture [4, 6, 8, 9]

Attritious wear is the result of the grain rubbing against the workpiece. The rubbing action between grain and workpiece results in high pressures and temperatures on the grain tips causing them to become dull and eventually forming wear flats [10]. As the number and size of wear flats increase, increasing frictional energy causes the temperature to rise. Eventually the metallurgical properties of the workpiece can change

and workpiece burn can occur [1]. Attritious wear is considered the most important form of wear because as wear flats develop, the forces acting on the grains increase, which lead to fracture wear [7].

The two types of fracture wear, grain and bond, are illustrated in Figure 2.3. Fracture wear is a result of the forces acting upon the grain becoming too large and either the grain, or the bond break. When grain fracture occurs, only a fragment of the grain is broken and new cutting edges can be exposed in a process referred to as "self-sharpening". Bond fracture is the complete dislodgement of a grain as the forces become too high for the bonding material to withstand. In both cases, fracture wear results in the wheel surface becoming irregular and in turn causes the workpiece surface finish and accuracy to deteriorate.

2.4 Wheel Surface Measurement Methods

It is well known that the wheel's topography, both macro and micro, play a large role in the grinding process. The wheel's macrotopography consist of the basic wheel shape and is responsible for the workpiece geometry [1]. The microtopography of a grinding wheel comprises of the distribution of abrasive grains over the wheel surface and their morphology [4] and is responsible for such things as workpiece roughness, energy, wheel life, and removal rates [1]. Much research has been performed to study the effect of the wheel topography on the grinding process and a multitude of methods have been developed in order to characterize different parameters. This section will discuss those methods in three categories: contact, non-contact and in-process methods.

2.4.1 Contact Methods

Contact methods involve direct contact between the grinding wheel and the measurement apparatus. The two methods discussed are stylus and imprints.

The use of a stylus, which is similar to standard surface roughness measurements, has been incorporated by several researches to measure the surface of the wheel. In this method a stylus coupled with a displacement transducer is dragged along the wheels

circumference producing a profile of the wheel topography. Wheel surface measurements acquired by a stylus have been used to characterize multiple topographical characteristics including: number of cutting edges [11, 12, 13], active surface area [14] and grain sharpness and wheel coarseness [11, 13]. Figure 2.4 illustrates the setup used by Xie et al. [15] in which a coordinate mapping machine (CMM) was used to characterize the protrusion height and rake angle of the wheel's grains.
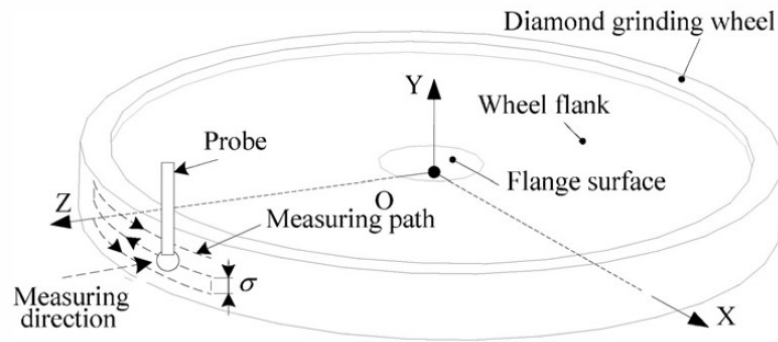
Figure 2.4 Stylus method schematic [15]

A significant drawback inherent in stylus measurements is that the size of the stylus tip limits the resolution of the measurement, and the small features of the grains are not picked up [16]. It is also difficult for the stylus to obtain measurements below the outermost layer of the surface without getting hung-up and caught in the crevices. The measurement method is also limited in scanning speed. If the stylus moves too fast it can lose contact with the wheel surface, resulting in the loss of detail throughout the measurement [17]. Additionally, using the stylus or probe on a very rough hard surfaces such as grinding wheel surfaces can cause accelerated wear to the stylus [18].

Another contact measurement technique used to obtain topographical data of grinding wheels is the imprint method. The wheel is rolled over a second surface and the imprint that is left behind is examined. Different mediums have been used to roll the wheel over including soot [19], dye [20], lead tape [21] and carbon paper [22]. The principle was that cutting edges would leave a noticeable feature on that surface. The number of cutting

points can be evaluated from the features left on the rolled surface. While fairly simple, this method results in inaccurate measures and is time consuming [23].

2.4.2 Non-Contact Methods

Several non-contact measurement methods have been developed in order to characterize the wheel without the drawbacks associated with contacting the wheel including inaccuracies and rapid wear. Non-contact measurements vary greatly, in both method and complexity, from an LED and phototransistor to a 3D confocal laser scanning microscope.

SEM images provide a very detailed image of the grinding wheel surface with excellent depth of field. Researches have used SEM to study the grain geometry [24], cutting edge density [25], dressing effects [26] and active surface [27]. It is even possible to acquire a 3D measurement from an SEM by using stereo photographs and a triangulation process [28]. The drawback to an SEM is that it requires a small sample size and, therefore, the grinding wheel must be destroyed preventing any further process monitoring.

Conventional optical microscopes have also been used in the characterization of the wheel surface. Lachance et al. [29] developed a system that could measure wear flats automatically from microscopic images without removing the wheel from the machine using a custom positioning system and image processing techniques. Their design is shown in Figure 2.5. Feng and Chen [30] were able to monitor the wheel loading using microscopic images and image processing with a similar method to Lachance et al.
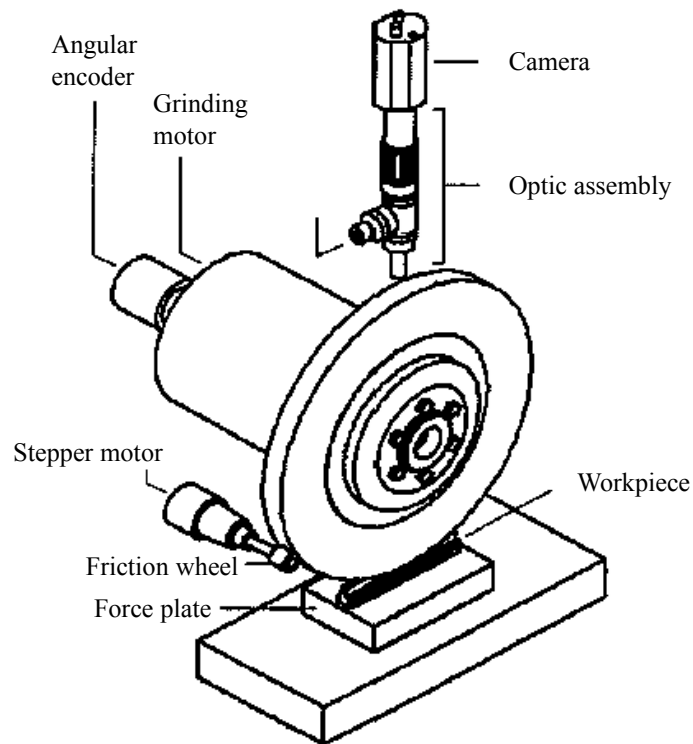
Figure 2.5 Wear flat measurement system [29]

Fathima et al. [31] used an LED and phototransistor to measure the profile around the circumference of the wheel to study the basic shape of the wheel. The setup is shown in Figure 2.6, as the wheel is rotated it interrupts the light traveling to the phototransistor. The interruption pattern is used to describe the wheel surface.
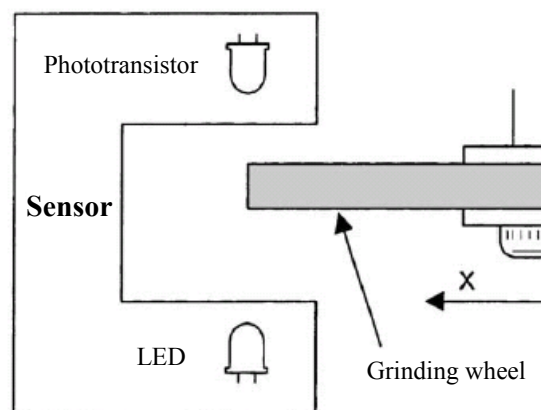
Figure 2.6 Wheel profile sensor [31]

Auto-focusing systems have been incorporated with lasers to measure the distance from the object using theory that when in focus, the light intensity measured will be higher than when out of focus [32]. White light interferometers (WLI) have also been used to obtain a variety of grain topography parameters [33, 34, 35, 36]. WLI works on the principle that if the distance to one light source is known, the interference pattern between it and another light source can be used to determine the distance to the second source. Generally, small samples are required for this method although Hecker et al. [33] used a combination of a WLI and the imprint method to scan an imprinted surface of the grinding wheel in order to compensate for the curvature of the wheel in larger scans. The incorporation of the imprint method however, introduces the same aforementioned issues.

Confocal laser scanning microscopes have recently been implemented into grinding research. They have the ability to acquire optical images and 3D topographical data at the same time. Tahvilian et al. [37] used the digital image to create a mask of the grains in the scan, which allowed for the removal of bonding material from 3D topographical data. Small samples were again required for this work, resulting in the destruction of the wheel.

Darafon et al. [38] developed a system capable of scanning an entire grinding wheel with the use of a white light chromatic sensor and a custom positioning control system. This same system is the basis of this thesis and will be discussed in detail in the following chapter.

2.4.3 In-Process Methods

As the name implies, in-process measurements are taken during grinding process and do not involve any interruptions. The methods that are commonly used are force dynamometer, thermocouple and acoustic monitoring.

The dynamometer and thermocouple methods are based on the same principle. As a cutting edge passes over the sensor a force or thermal pulse will be measured [4]. When measuring the force, a razor thin workpiece is mounted on the dynamometer so that

individual force pulses may be identified. Based on the kinematics of the process and number of pulses measured the cutting edge density can be derived. The measured pulses are often not clearly separated causing difficulty in interpreting the data [4]. The thermocouple technique is very similar, except the sensor is embedded in the workpiece [4].

Acoustic monitoring has also been used to measure the wheel in several different ways. Acoustic emissions have been monitored during the process and proven to successfully define a worn grinding wheel [39]. By mounting an acoustic emission sensor on a dressing tool, Weingaertner and Boaron [40] were able to count the number of cutting edges on a grinding wheel and map their location.

2.5 Summary

This chapter introduced the essential information in order to completely comprehend the findings of this work. The grinding wheel itself was discussed, and then the kinematics of the operation was covered with information on how to calculate the uncut chip thickness. Next the three main grinding wear mechanisms were discussed which were attritious, grain and bond fracture. Grinding wheel surface measuring techniques were then discussed in three categories: contact, non-contact and in-process.

Chapter 3. Grinding Wheel Scanner

This chapter will introduce, in detail, the grinding wheel scanner which has been previously developed. The three major issues that have been observed with the scanner, namely: poor resolution, lack of a homing procedure and controller reliability, will be discussed. The issues were then resolved and their solutions include an additional encoder, the design of a vision based homing system and the implementation of a real-time controller.

3.1 Measurement Principle

The main component of the grinding wheel scanner is a Nanovea CHR-150 Axial Chromatism sensor. It is the device used to obtain the topographical data of the grinding wheel. Axial Chromatism is an optical measuring technique that takes advantage of the different wavelengths of light. A white light source is separated into its spectral components as it passes through a lens with a high degree of chromatic aberration. As seen in Figure 3.1, the color of light transmitted back to the sensor is dependent on the distance of the object in focus. A pinhole and diffraction grating configuration ensure that only focused light is transmitted back to the CCD strip, which is used to determine the measured distance.

Optical fiber cable →

Optical pen

CHR-150

Objective
lens

Beam
splitter

Collimating
lens

Pinhole

Diffraction
grating

Linear
CCD

Light source

Measurement
Range

Measured distance

Wheel surface
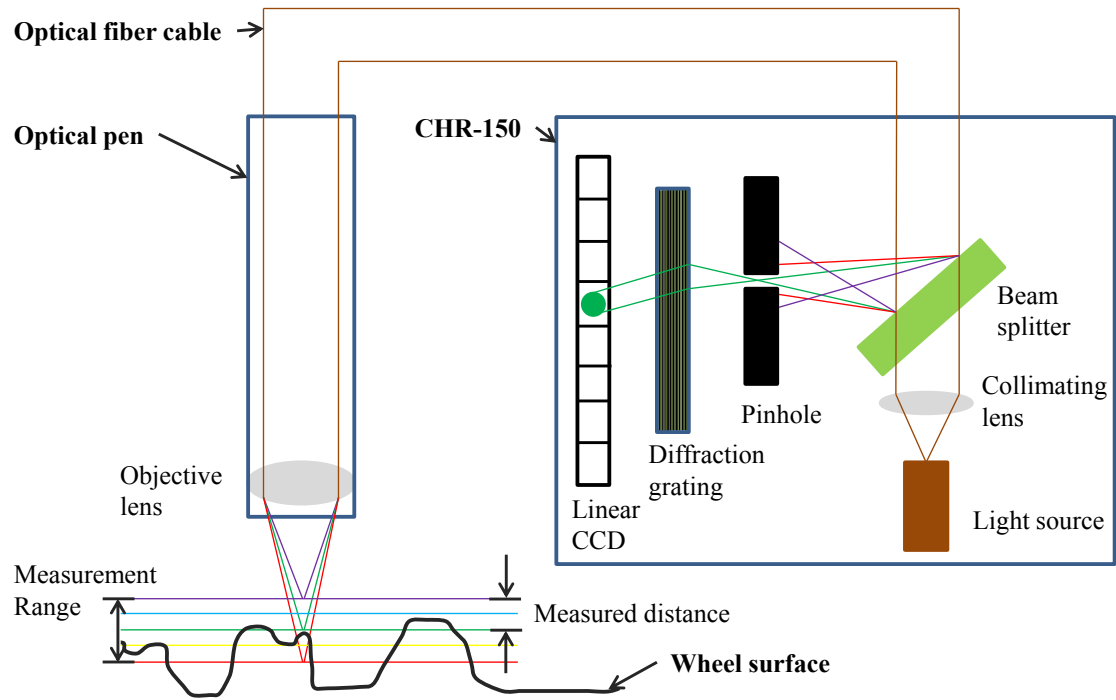
Figure 3.1 CHR-150 Schematic (adapted from [41, 42])

3.2 Scanning Method

The grinding wheel scanner was designed so that the optical pen from the previously discussed section can scan an entire wheel. In order to accomplish this, positioning systems we're established in the x, y, and z coordinates which can be seen in Figure 3.2. The x-axis drive system is comprised of a SILVERPAK 17C stepper motor connected to a friction wheel by a 50:1 planetary gearbox. When the friction wheel is brought into contact with the wheels surface they both rotate. In order to monitor the position of the grinding wheel as it is rotated there is a Teledyne-Gurley Series 825 rotary encoder attached to the number 40 tapered vertical spindle on which the grinding wheel sits. The optical pen is attached to a Parker Series 4000 stage and ZaberTLA28A linear actuator to achieve motion along the y-axis. The optical pen itself obtains the z-axis information but a custom horizontal lead-screw stage was designed to move the pen within its working distance. There is also a digital camera attached to another horizontal stage with 40° separation between the two.
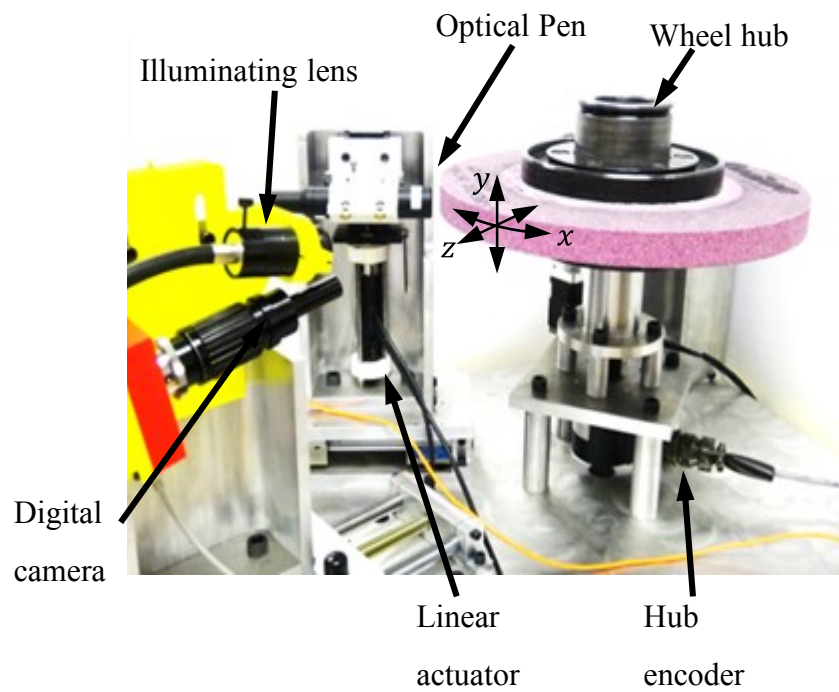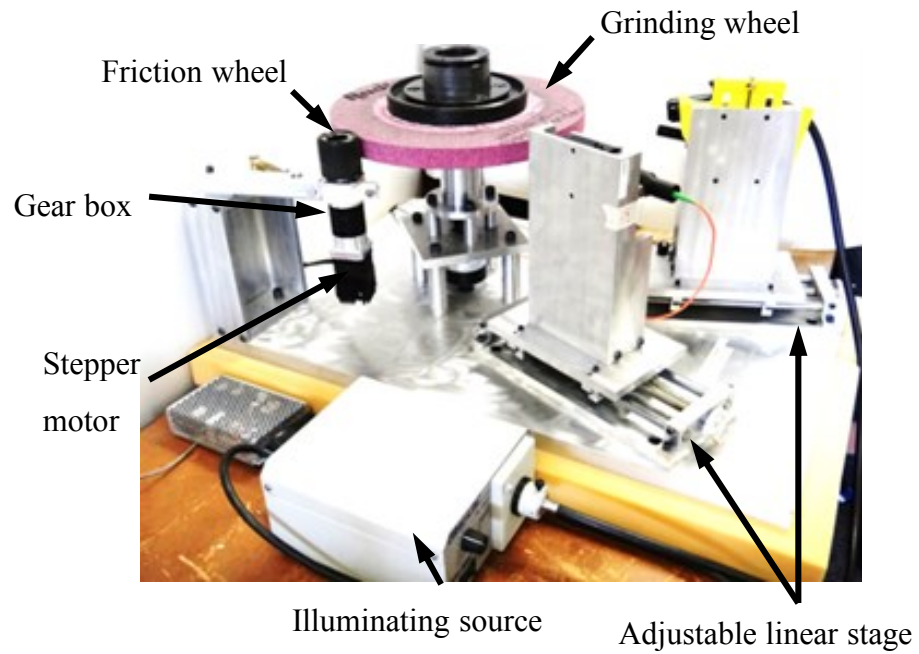
Figure 3.2 Grinding wheel scanner [38]

3.3 Scanner Issues

The previously developed scanner had three significant problems. The following section will discuss those problems which were: resolution, homing and reliability.

3.3.1 Resolution

The encoder connected to the hub of the grinding wheel is an incremental quadrature encoder. Quadrature encoders work by fastening a code disk to a rotating shaft as shown in Figure 3.3. The code disk is comprised of both opaque and transparent sections. Two light sensors (A and B) are constantly reading for a light signal. As the disk rotates light from the two light sources is either blocked by the opaque sections or passes through the transparent sections to the light sensor. By analyzing the output signals the position and velocity of the encoder can be determined. Figure 3.3 depicts the operation of an encoder and its output signals.
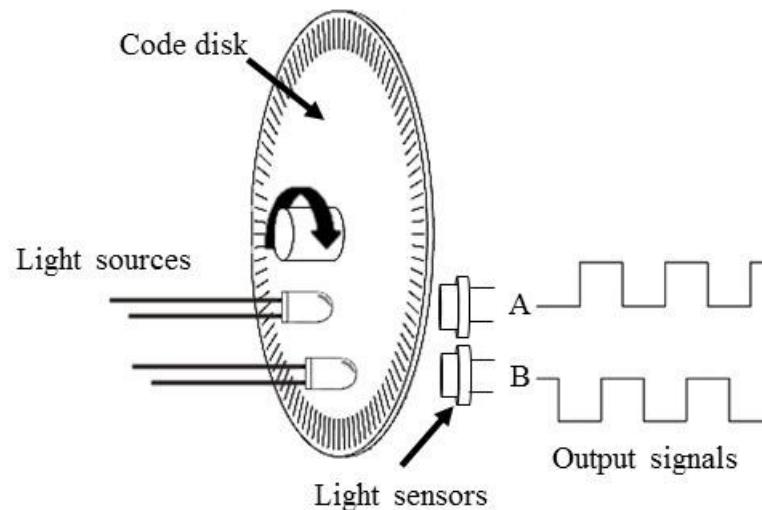
Figure 3.3 Depiction of encoder functionality (adapted from [43])

The resolution of an encoder is directly related to the number of windows that its code disk has. The scanner's hub encoder consists of 12000 windows. Using an encoder in quadrature mode produces four counts per each cycle. Therefore the hub encoder produces a total of 48000 counts per revolution (CPR). While this may seem like a high

resolution, when factoring in the diameter of grinding wheel the final resolution is diminished significantly. As seen in Figure 3.4, the arc length s, which is equivalent to the resolution of the x-axis position of the scanner, is dependent on both the central angle θ and the radius r.
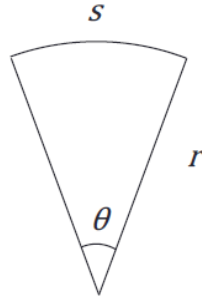
Figure 3.4 Arc Length

The central angle was determined to be 0.0075° with the following relationship:

$$\theta = \frac{360°}{CPR} \tag{3.1}$$

With the largest radius of the grinding wheel being 203 *mm*, the worst-case scenario resolution in the x-direction was found to be 26.5 *μm* using the following equation:

$$s = 2\pi r \theta \tag{3.2}$$

This resolution results in numerous data points being taken during the same encoder value if the sampling interval is set to a value below 26.5 *μm*. To account for this fault, data was previously resampled assuming constant velocity of the wheel [38]. This method however did not account for slip, which is an inherent issue when using a friction wheel. External vibrations from someone bumping the table or even walking by could affect the contact between the grinding wheel and friction wheel. Preferably, the physical resolution of the scanner's x-axis would be closer to that of the resolution of the optical pens which are 4 *μm* and 1.4 *μm* for the 1200 *μm* and 130 *μm* pens, respectively.

3.3.2 Homing

The end goal of the grinding wheel scanner is to monitor the effect of the grinding process on the wheel's surface micro-topography and vice versa. Without a homing system this wheel monitoring can prove difficult, as the location of the scanned area is lost if the grinding wheel is removed from the scanner and replaced. The addition of a homing system would allow for repeated scanning of the same area between multiple grinding tests.

3.3.3 Reliability

The largest concern with the previous scanner was its control reliability. All of the components were originally operated using a LabVIEW program on a desktop computer. The control system needs to be able to control all components and acquire measurements synchronously and with very precise timing. Using a computer to control all components proved to be problematic in several situations. The computer's top priority is not to control the scanner and, therefore, it could become bogged down with performing other tasks. The computer repeatedly would crash while running the LabVIEW program, indicating that the control and acquisition was straining the computer's limits. The third party encoder board also required the computer to be constantly running several background programs in LabVIEW in order to acquire the encoder position. This third party software would often fail, causing the motor to spin uncontrollably until the power was shut off to the system. Together, these problems rendered the scanning system problematic. Entire measurements and their resulting time could be wasted if any of these issues arose during a scan.

3.4 Friction Wheel Encoder

To resolve the issue of a lack of resolution in the x-direction, an encoder was attached to the drive shaft of the friction drive motor. The new encoder is a US Digital E5 series with 4000 counts per revolution. With the addition of the 50×1 gearbox this encoder gives 2×10^5 counts per revolution. Placing an encoder directly on the drive system greatly increases the resolution due to the relatively small size of the friction wheel. The friction

wheel has a diameter of 41 *mm*. Using the added encoder as the x-position gives a constant resolution of 0.65 *μm*, which is finer than either of the optical sensors. The added encoder also allows for tracking the relative motion between the two wheels, which can be used to monitor slip as will be discussed in Section 4.1.1.

3.5 Vision Based Homing

There is a need to be able to remove the grinding wheel and place it back in the exact same position. The desired resolution of the homing system is to be within the sensor resolution, which is 1.4 and 4 *μm* for the 130 and 1200 *μm* optical pens, respectively. The homing system must be able to withstand the harsh environment in the grinding machine and also not affect the balancing of the grinding wheel. A vision based homing system was determined to be the optimal method due to its small target requirement and relatively small space needed. The two key components to homing the grinding wheel scanner are the hardware and software which will be discussed in this section. The setup can be seen in Figure 3.5, which includes the target and the camera.
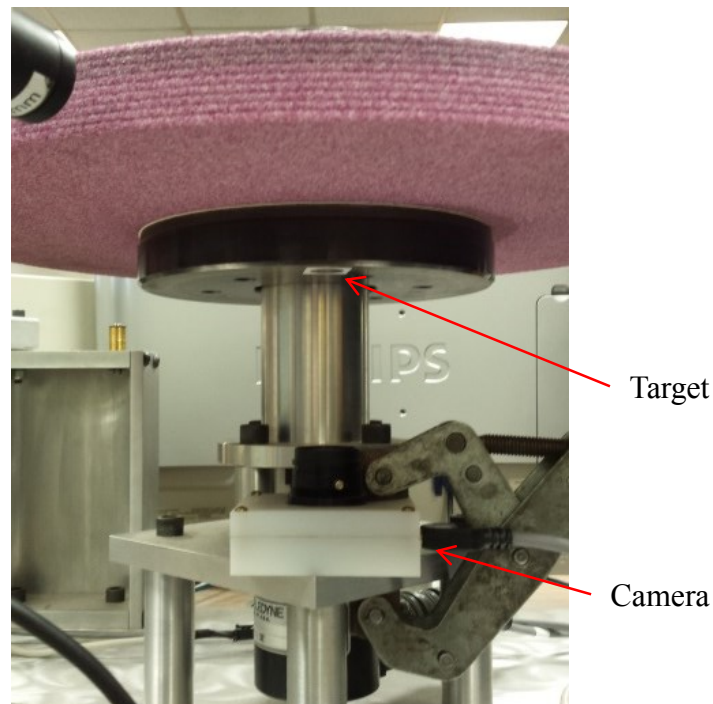
Figure 3.5 Homing system setup

3.5.1 Homing Hardware

When dealing with imaging there are many factors that affect the resolution of the system. Using imaging to home the grinding wheel scanner requires an understanding of how cameras work and the different parameters to take into consideration. Figure 3.6 depicts the essential parameters that were taken into account during the design of the system. The fundamental imaging parameters are as follows [44]:

- Field of view (FOV): The total area that the image covers.
- Resolution: The smallest resolvable feature in the image.
- Sensor size: The size of sensor is an important limit in the system resolution.
- Working distance (WD): The distance from the lens to the object.
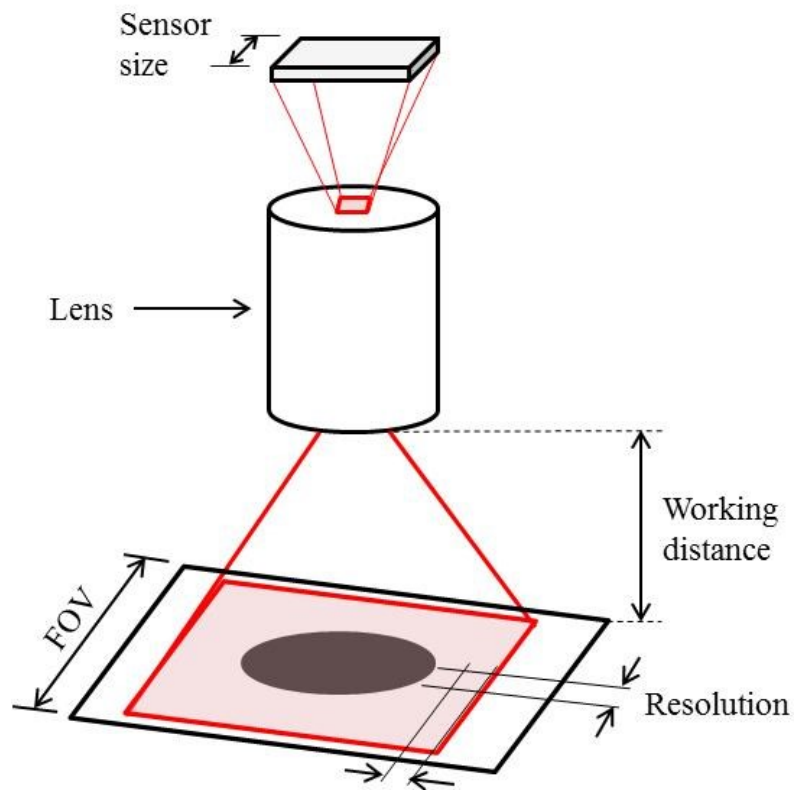
Figure 3.6 Essential imaging parameters (adapted from [44])

A Point Grey Dragonfly2 series camera was used for the application. The two main components in the camera system are the imaging sensor and the lens. The sensor determines the spatial resolution of the system, meaning the smallest feature it can detect. can be used to calculate the resolution of a camera.

$$Camera\ resolution = 2 \times pixel\ size \tag{3.3}$$

The pixel size of the camera was 7.4 μm, giving it a resolution of 14.8 μm. The sensor by itself is incapable of producing a usable image for the homing process and requires a lens to magnify the object of interest. For this application the lens was selected based on a working distance constraint. After evaluating the free space within the complete volume of the system, the optimum location for the homing mechanism was determined to be underneath the grinding wheel. It was deemed necessary to place the homing target on the hub rather than the wheel itself. In order to see the hub, the camera had to be placed on the plate seen in Figure 3.5, which left a maximum working distance of 12.5 cm.

The camera itself has a height of 1.5 cm, leaving 11 cm between the camera and hub as the maximum working distance for the application. A 12 mm fixed focal length lens was selected for the system which has a minimum working distance of 20 cm. By applying a 1 cm spacer into the system's optics, the minimum working distance was reduced to 8 cm. The sensor is roughly 4.9 mm and the lens configuration gives a final field of view of 3.24 cm, which can be used in the following equation to calculate the primary magnification of 0.15 for the system:

$$Pmag = \frac{Sensor\ size}{FOV} \tag{3.4}$$

After applying the optics to the systems, its final resolution is diminished due to the magnification. Equation (3.5) is used to determine the system's resolution of 100 μm.

$$System\ resolution = \frac{Camera\ resolution}{Pmag} \tag{3.5}$$

The selected target was a black, 1.5 *cm* circle printed on white vinyl adhesive. The vinyl was selected to ensure that the target would stay in place while being exposed to the elements in the grinding machine, mainly the oil based coolant at high velocities.

3.5.2 Software

LabVIEW's image analysis software was used to perform the image acquisition and processing. A custom LabVIEW program was then developed in order to home the machine. The first step in the homing program is to search and locate the circle. LabVIEW's match pattern sub-VI is used to determine whether the circle is in the frame or not. This function looks for edges in the image and determines whether or not they match a template, which was set as the target. Once the circle is detected, a "locate circular edge" function is used to determine the center of the circle with sub-pixel resolution. This function works by creating a spoke wheel search field defined by two radii and spacing. Figure 3.7 (a) depicts the search wheel's parameters and Figure 3.7 (b) shows a screen shot of the real-time circle tracking in progress.
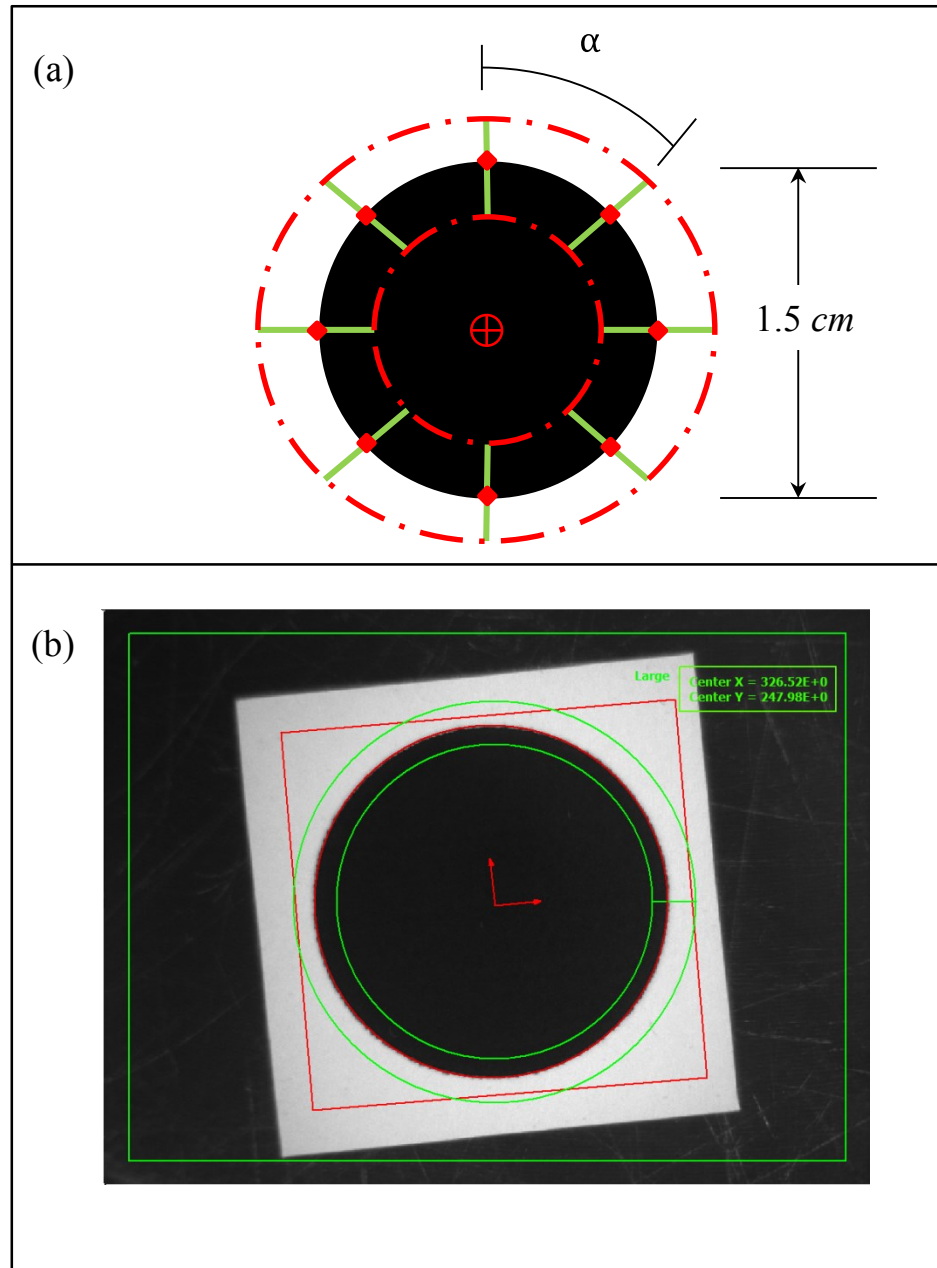
Figure 3.7 Circle tracking (a) search algorithm and (b) real-time example

The search lines in Figure 3.7 (a) are 45° apart to simplify the illustration. Each search line, shown in green, finds an edge along itself. By using search lines that are separated by 1°, the program fits a circle to 360 data points, thus obtaining sub-pixel resolution. Each search line also uses a sub-pixel algorithm to find the edge of the circle. The edge detection algorithm that the LabVIEW functions use can accurately detect edges to 1/25

of a pixel size, which gives is equivalent roughly 2 *µm* [45]. This value agrees with observations, since when the wheel is stationary the center position value varies ± .04 pixels. To home the grinding wheel, the friction wheel drives the grinding wheel until the center of the target is located in the correct position.

3.6 Real-Time Controller

The reliability of the scanning system was a primary concern. The computer was unable to acquire all measurements and information synchronously, and simultaneously control the positioning system on its own. A designated controller was therefore implemented in order to separate the computer's processing tasks from the control of the scanner. National Instruments' CompactRIO (cRIO) controller series offered multiple appealing aspects for the application. The cRIO series combines a Field-Programmable-Gate-Array (FPGA) with a real-time (RT) controller.

3.6.1 FPGA Overview

FPGAs are reconfigurable silicon chips that consist of logic cells and programmable switches. The logic cells and switches can be individually programmed to perform desired functions using hardware rather than software. There are several benefits to using an FPGA rather than a microprocessor found in a computer. Running programs through hardware rather than in software results in faster hardware I/O and parallel processing capabilities [46]. Both benefits played large roles in the selection of the FPGA rather than using a microprocessor. When acquiring measurements as precise as the grinding wheel scanner the speed of the I/O is crucial to record reliable measurements. With the addition of the motor encoder, there are two pulse trains to monitor and the motor pulses will be changing up to 40 times faster than the hub encoder. The system also needs to be well synchronized to ensure that it is acquiring the correct data from all the components simultaneously. The FPGA's parallel processing capabilities allow for a reliable synchronization, as the components are not all fighting for processing power.

3.6.2 Controller

The selected controller was the CRIO-9076 model shown in Figure 3.8 . It has an integrated 4 slot LX45 FPGA chassis and 400MHz real time processor. The LX45 has 43661 reconfigurable logic cells discussed in the previous section. The chassis accompanies National Instruments I/O modules. In order to control the scanner, three modules were needed. From left to right in Figure 3.8 they are: an NI 9401 Digital I/O for the encoder readings, an NI 9870 for serial communication to the sensor and y-axis actuator, and an NI 9502 to control the friction drive motor. One open slot remains for future expansion. The real time processor is the connection between the hardware I/O to the PC. It performs the synchronized data acquisition from the FPGA, processes the data, and then writes it to a flash drive connected to the USB port on the controller. The FPGA is constantly communicating with the hardware and, when necessary, the processor retrieves the required data.
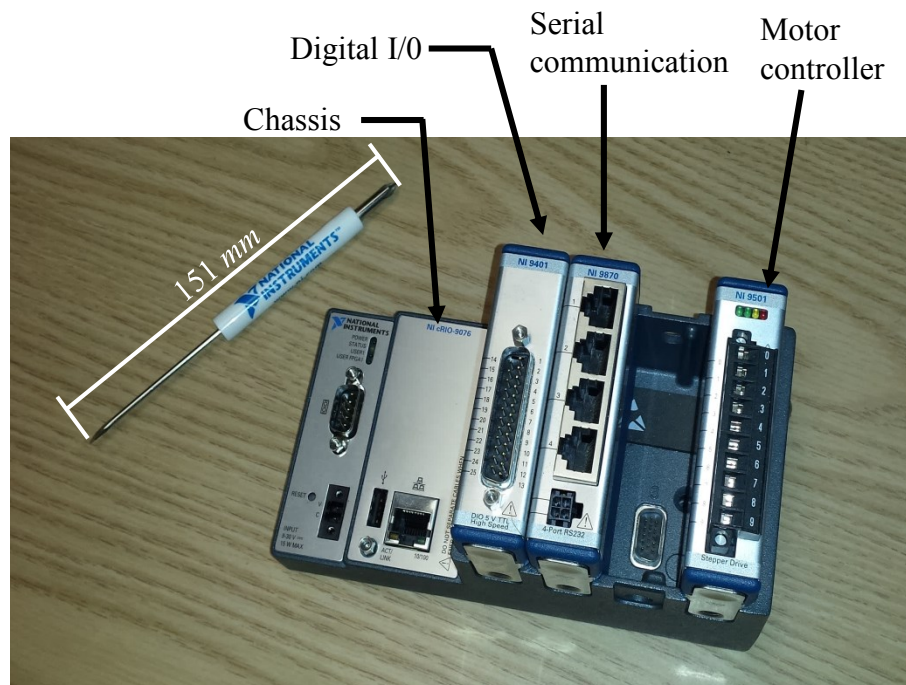
Figure 3.8 cRIO Controller with modules

3.6.3 Software

Custom LabVIEW programs were developed to control the scanner. Using a cRIO required three levels of code to be developed: FPGA, Real-Time, and Host PC. The Host PC contains the user interface to control the entire system. The desired sampling interval and sampling rate are used to determine the motor speed and direction. The speed and size of the scan are then sent to the RT program, which communicates to and controls the FPGA program. As the scan progresses, data from the sensor and two encoders are sent from the FPGA to RT level to be analyzed and logged.

3.7 Summary

This chapter presented the previously developed grinding wheel scanner which uses a chromatic sensor to obtain topographical surface measurements from the grinding wheel. The issues that were hindering the scanner were then discussed including resolution, lack of a homing procedure and control system reliability. Solutions to these issues were then established. An additional encoder placed directly on the motor creates a theoretical constant x-direction resolution of 0.65 μm, which is 40 times more accurate than the previous generation scanner. A vision based homing system was then developed which uses a circular target adhered to the hub of the grinding wheel. A camera that is held stationary on the position system is then used to monitor the position of the camera. Sub-pixel approximation was used to reduce the resolution of the homing system from 98 μm to 2 μm. A real-time controller was then implemented into the system. This new controller runs separately from the host computer which allows for control of all components without fighting for PC computing power. The controller also offers FPGA capabilities which allow for constant and simultaneous control and communication to all scanner components.

Chapter 4. Validation

This chapter presents the validation of the grinding wheel scanner. The primary concern of the validation was the positioning system since the optical sensor has already been factory calibrated. The validation began with two and three dimensional scans of simple well-defined test surfaces. The test surfaces were required due to the complexity of an actual grinding wheel surface. Once the positional accuracy was validated a grinding wheel surface was measured and compared with scanning electron microscope (SEM) measurements. 3D analysis software was then used to compare the surfaces of worn and fresh grains.

4.1 Profile Scan

One scan of a grinding wheel can consist of tens of thousands of individual profiles and in order to validate the scanner the first step is to ensure that it could repeatedly scan one profile. A metal grinding wheel with grooves scribed in it was used for the positioning system validation as seen in Figure 4.1 below.
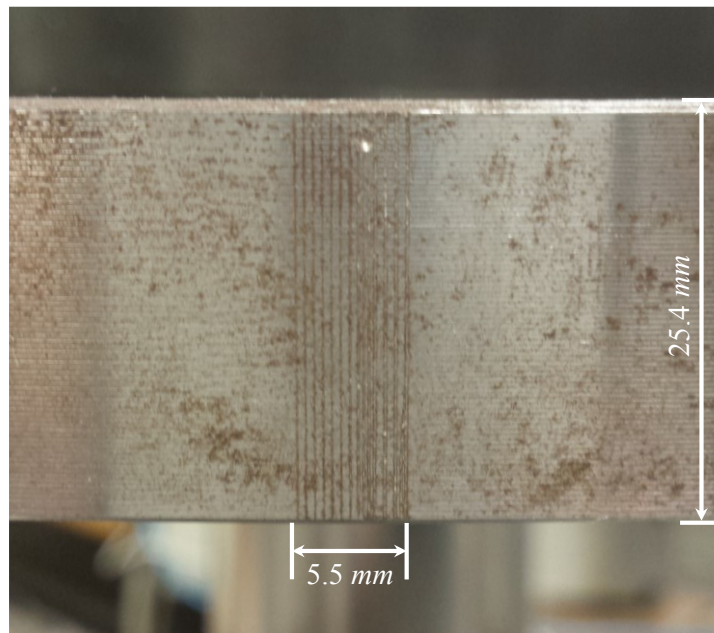
Figure 4.1 Etched grooves

4.1.1 Slip Compensation

Using the 1.2 *mm* optical pen the grooves were scanned repeatedly 20 times at a velocity 1.5 *mm/sec* and a sampling rate of 300 *Hz* in order to achieve a sampling interval along the metal grinding wheel of 5 *µm*. The vertical stage was kept at the same height to ensure the same profiles were being scanned. In order to emulate an actual area scan the friction wheel was kept in continuous contact with the wheel for these experiments, and the scanner was not homed between profiles. Figure 4.2 shows five of the profile measurements.
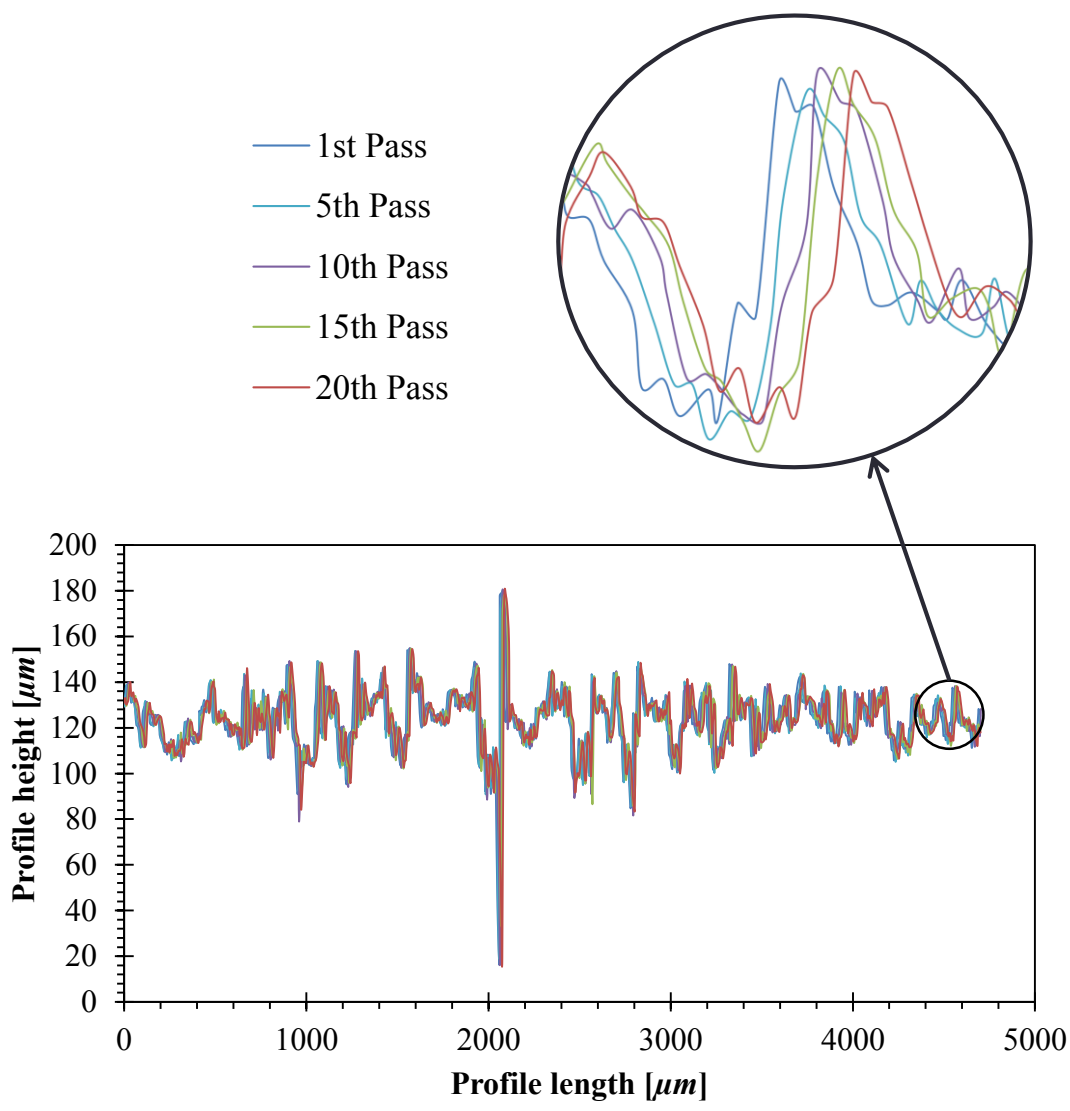
Figure 4.2 Etched grooves profile scan

If the scanner was working perfectly then all of the profiles would be identical. Figure 4.2 clearly shows that the two scans are not identical. Each pass progressively is being shifted to the right which indicates that there could have been slippage between the friction wheel and metal wheel. To further investigate the potential for slip, both the friction wheel and grinding wheel encoders were monitored throughout the scans. If slip was occurring between the two wheels then their respected encoders should be able to capture the slippage. Figure 4.3 shows two encoder pulse trains for the first and 20th pass. Since the resolution of the hub encoder was much lower than that of the friction wheel it is possible to plot them as a function of each other.
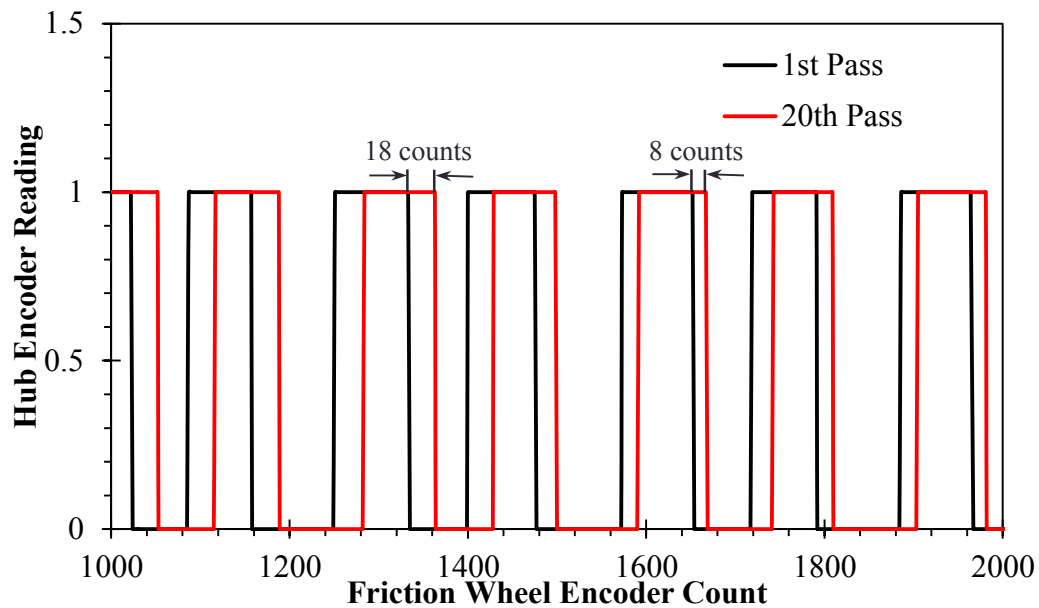
Figure 4.3 Non-constant slippage seen in encoder pulse trains

As shown in Figure 4.3, the same lagging effect can be seen between the 1st and 20th passes, which confirms that there was indeed slip. Another important point to note from Figure 4.3 is that the difference is not constant throughout the scan. In order to correct for the varying amount slip throughout a profile both encoder readings were simultaneously recorded. A MATLAB program was then created to align each successive pulse train with the first profile. By monitoring the motor pulse count for each shift in hub encoder

reading it is possible to measure the difference at each hub pulse based on the motor encoder count. The difference can then be used to shift the current profile back in line with first profile. Since each hub encoder pulse value has several corresponding data points and the slip was not constant throughout it was necessary to linearly interpolate between the current pulse difference and the following difference values. Figure 4.4 shows the effect of interpolating the shift value. The black triangles and red squares depict measurements being taken for the 1st and 20th pass, respectively.
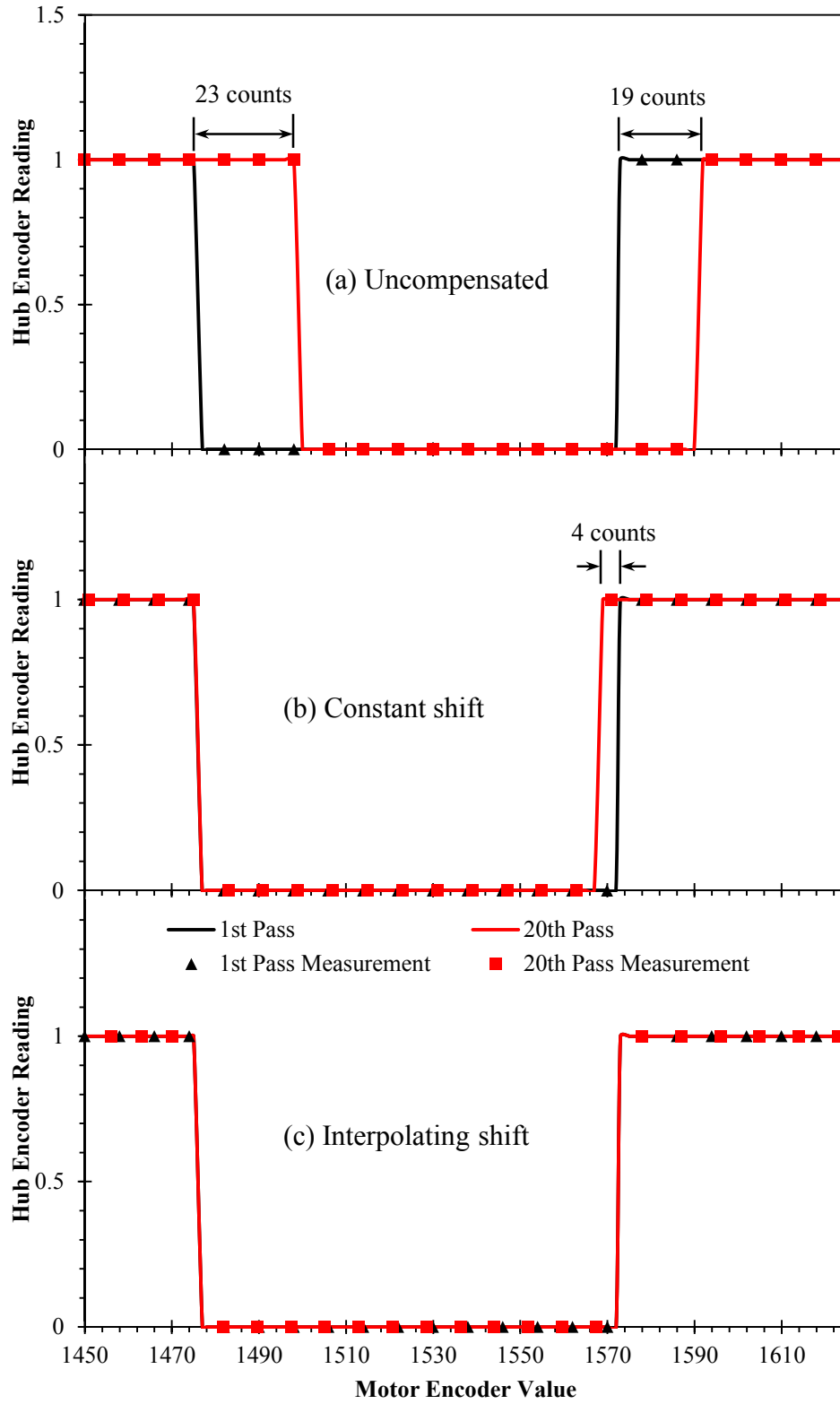
Figure 4.4 Pulse train comparison for (a) uncompensated, (b) constant shift and (c) interpolating shift

It can be seen in Figure 4.4 (a) that the first pulse had a difference of 23 friction wheel encoder counts while the second pulse was only off by 19 counts. In Figure 4.4 (b) the 20th scan was shifted back by a constant value equal to the difference at the first pulse, which results in another shift of 4 counts pulses remaining at the end. To account for this, the linear interpolating shift can be seen in Figure 4.4 (c). Figure 4.5 shows a plot of the corrected profiles
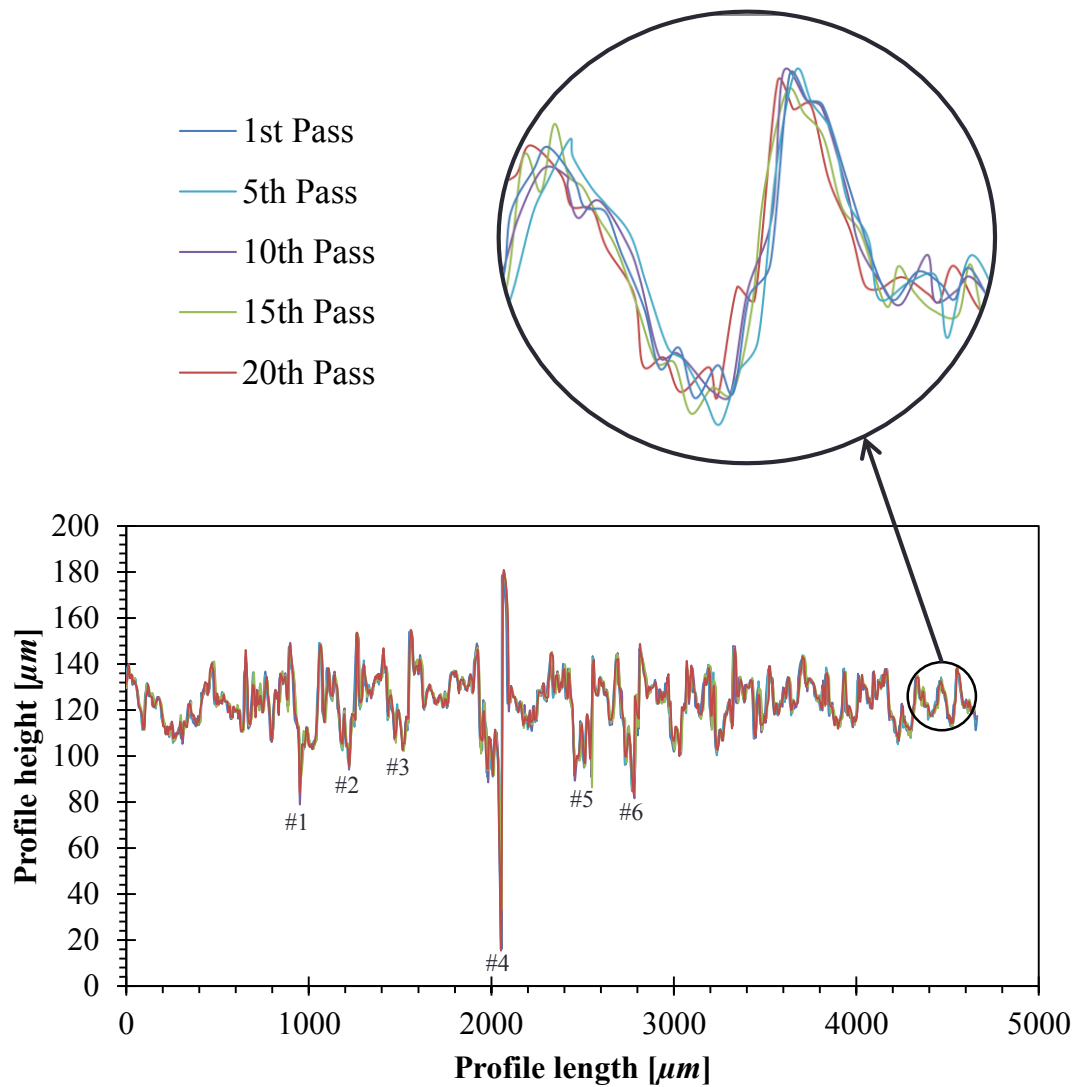
Figure 4.5 Corrected groove profiles

The alignment of the grooves in Figure 4.5 clearly presents an improvement from Figure 4.2. Figure 4.5 also shows the numbered grooves from 1 to 6. In order to quantify the capability of the slip compensation algorithm, the largest differences at six of the grooves were recorded for both the original and compensated scans. An example of the method is shown in Figure 4.6, in which the largest differences of groove number 4 are being measured for the uncompensated and compensated scans.
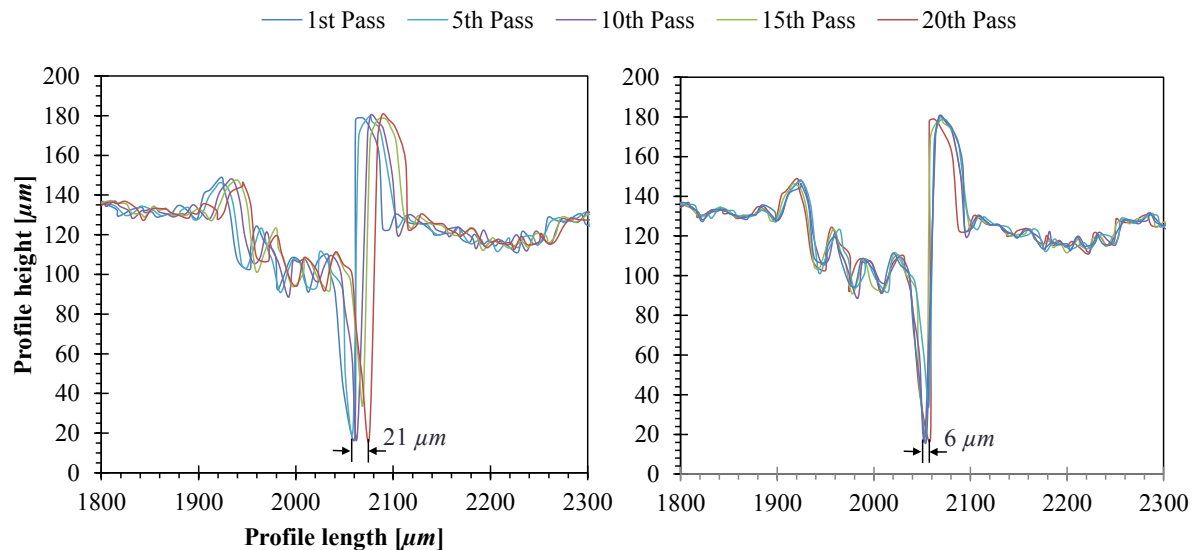
Figure 4.6 Measuring of largest difference for groove number 4

The results for the six grooves are summarized in Table 4.1 Throughout the 20 passes the average maximum uncorrected difference of the profiles was 17.8 μm. It is important to bear in mind that this experiment was only performed over 20 passes and a scan of a grinding wheel could have tens of thousands profiles and therefore the total slip would be much greater. After slip compensation the difference went down to 5.7 μm. This remaining error was most likely due to the resolution of the pen which is 4 μm and the fact that the sampling interval itself was 5 μm. Vibrations from people walking by could also cause slight deviations in the scans.

Table 4.1 Maximum differences of groove locations

Peak number	1	2	3	4	5	6	Average difference
Uncorrected difference $[\mu m]$	22.0	15.0	19.0	21.0	14.0	16.0	17.8
Corrected difference $[\mu m]$	7.0	6.0	5.0	6.0	4.0	6.0	5.7

To further investigate this difference, the same set of experiments was performed with the 130 μm pen. The scanning parameters were kept the same, and since the resolution of this pen is 1.4 μm, it can determine if the resolution of the pen is causing the observed error in the corrected difference. Figure 4.7 shows the uncorrected and corrected groove number 4 scanned with the 130 μm pen.
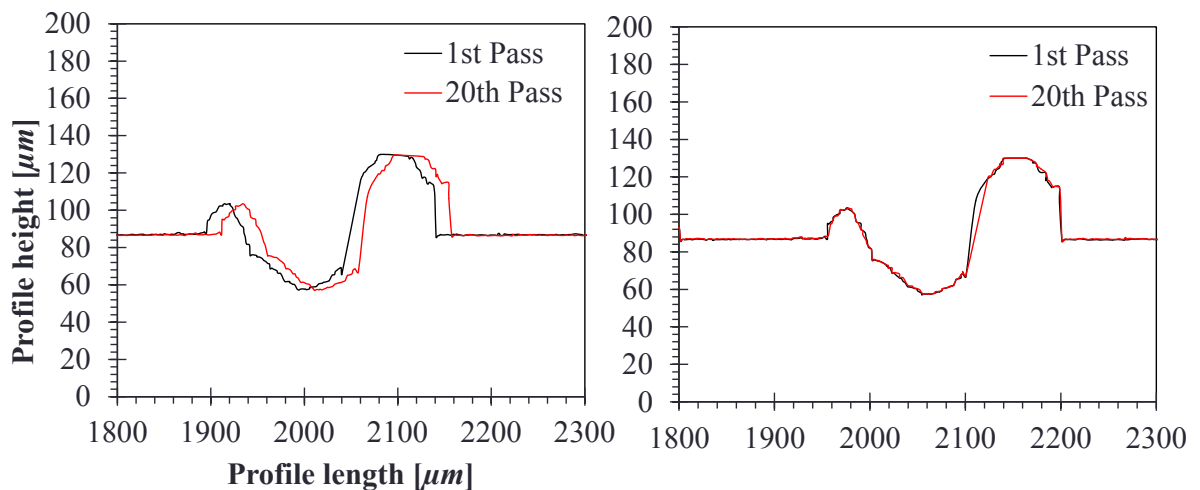
Figure 4.7 Groove comparison with 130 µm pen

As can be seen in Figure 4.7, the difference is much smaller than with the 1.2 *mm* pen. The correct profiles are nearly indistinguishable, but when measured have an average

difference of 2 μm, which proves that the errors seen with the 1.2 *mm* pen are largely due to the pen's spot size.

4.2 QR Scan

The next step was to validate the grinding wheel scanner's ability to take repeatable three-dimensional scans. A target was chosen that had surface features of known geometry so that repeatable measurements could be taken. The chosen target was a Quick Response (QR) code that represents "Dalhousie Mechanical Engineering". The QR code is a high contrast target that allows for the intensity readings from the CHR-150 sensor to be used rather than axial depth. The axial resolution of the optical pen is predetermined and calibrated; therefore, it is not controllable and is not a concern in the validation of the positioning system. A flat target makes for true measurement of the x and y directions, which were the main concern for this test. The QR code was printed as a 3 x 3 mm square so that the features being scanned would be within the size range of features of concern on an actual grinding wheel. It was then adhered to the metal replica wheel as seen in Figure 4.8.

(Dalhousie Mechanical Engineering)
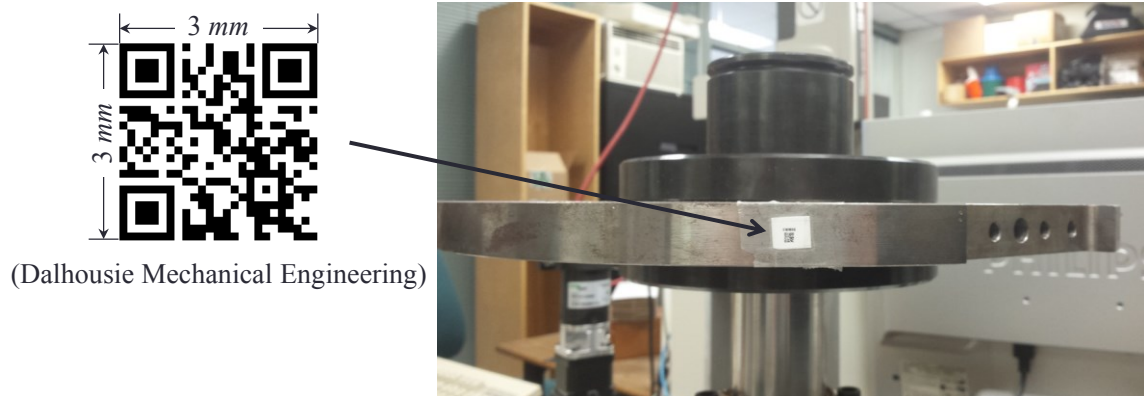
Figure 4.8 QR code

During experimentation with actual grinding wheels, the wheel will have to be removed from the scanner and placed into the grinding machine. In order to simulate grinding experiments being performed, the replica wheel was removed from the scanner after each scan. It was then placed back on the spindle to be homed. This procedure was repeated

four times with each pen in order to characterize the system completely. The scans were taken with sampling intervals of 5 *μm* in each direction.

4.2.1 QR Data Processing and Analysis

In order to use these measurements for validation the data needed to be processed accordingly. The first step in processing is to correct for any slip that has occurred during the scan. This step also functions as further validation for the slip compensation algorithm previously discussed. Figure 4.9 shows a comparison of an original and corrected intensity scan.
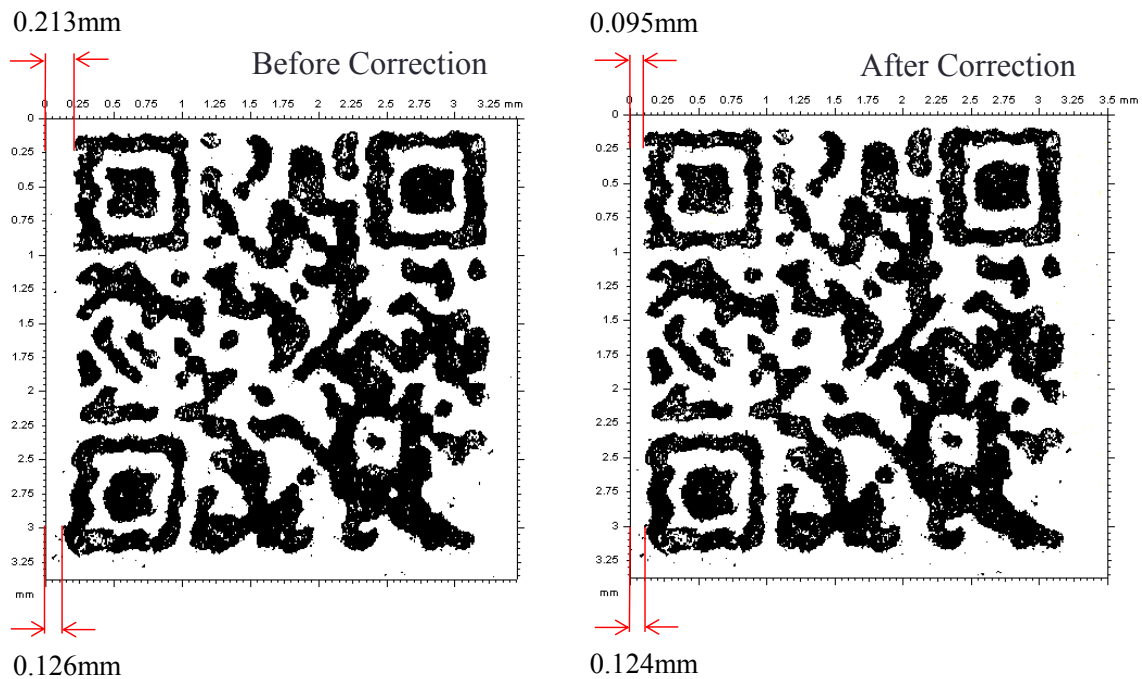
Figure 4.9 QR code slip compensation

Before correction it appeared as though the top and bottom left hand edges of the code were offset by 0.087 *mm* to the right. It can be seen from the compensated scan that the offset should have actually been 0.029 *mm* to the left, which concludes that 0.116 *mm* of slip has been corrected. The 0.116 *mm* of slip accounts for 3% of the total 3.5 *mm* scanned. The slip is relatively easy to see when using the QR code, but due to the randomness of the grinding wheel it is important to validate the slip compensation with a

known feature. Another aspect to note from Figure 4.9 is that the waviness of the features is likely due to the resolution of the printer and the roughness of the paper used, not the scanner or slip compensation. To confirm that the waviness is indeed real, a digital photo of the QR code was taken and can be seen in Figure 4.10 (a). By applying a threshold to the image the background was removed to appear more like the scanned data which can be seen in Figure 4.10 (b).

(a) Digital image

(b) Thresholded digital image   (c) Grinding wheel scanner
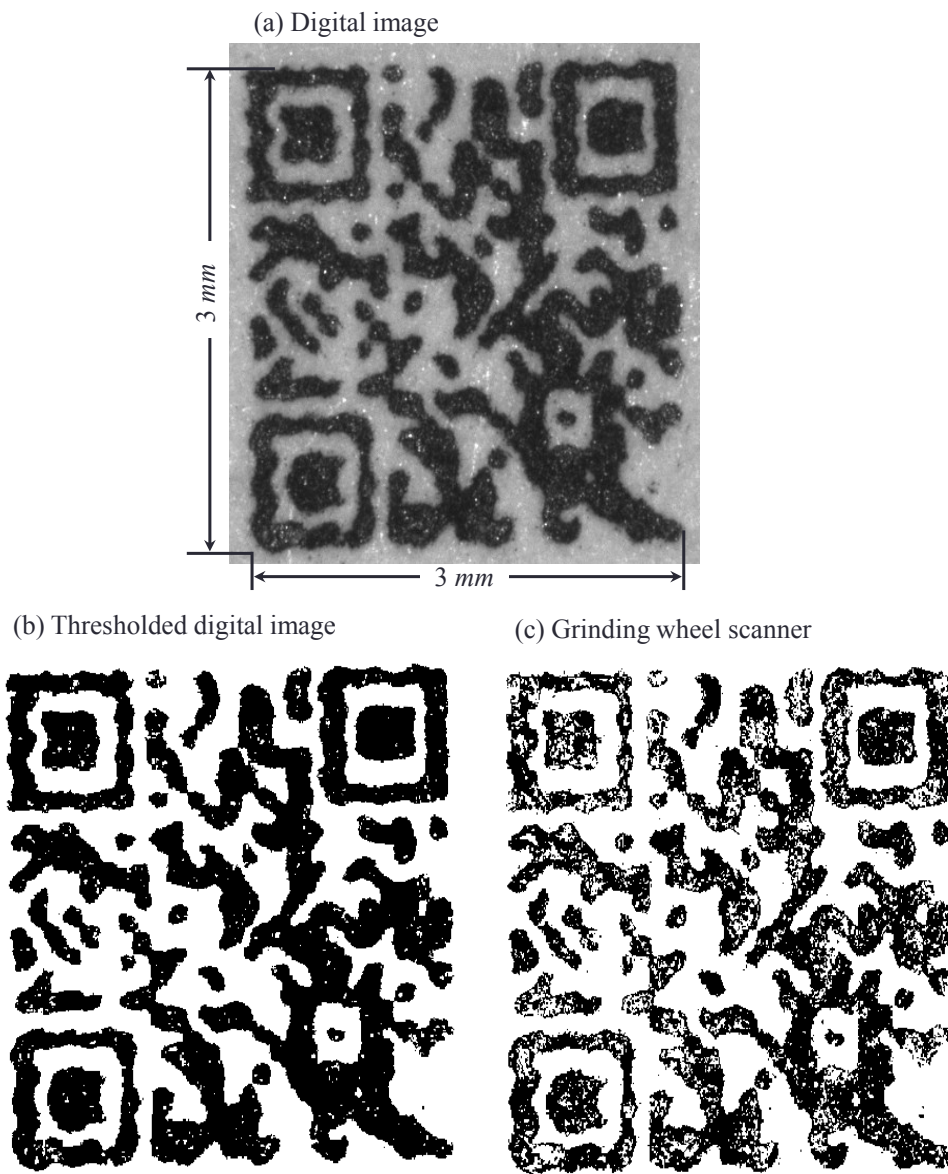
Figure 4.10 QR code comparison using (a,b) digital camera and (b) grinding wheel scanner

The waviness of the scan is clearly seen in the digital images as well. A large difference that is noticeable between Figure 4.10 (b) and (c) is that the camera had significantly more black in it than the scan did. This difference is most likely a result of the roughness of the paper once again. All of the features however look very similar in shape and size.

With the slip compensation validated using the digital image the next step was to develop a method to analyze the scans. The goal of this method is to validate and quantify the scanner's repeatability by comparing the distances between certain features and also the area of the same features. By converting the scan data into digital images it is then possible to use LabVIEW's image-processing software to analyze the subsequent scans. The pixel sizes in the images are directly related to the scan sample interval, which in this case was 5 μm in the x and y directions. Figure 4.11 demonstrates the four main steps in the process.

The aforementioned white areas seen in the Figure 4.11 (a) were first filled using a hole filling function as can be seen in Figure 4.11 (b). This function creates well-defined features that are able to provide a more robust analysis. Next an edge detection based pattern matching function was used to locate the centroids of 10 features. These features are shown with red boxes around them in Figure 4.11 (c). With all of the features located, it was then possible to analyze the data by performing a projection calculation, which is demonstrated in Figure 4.11 (d).
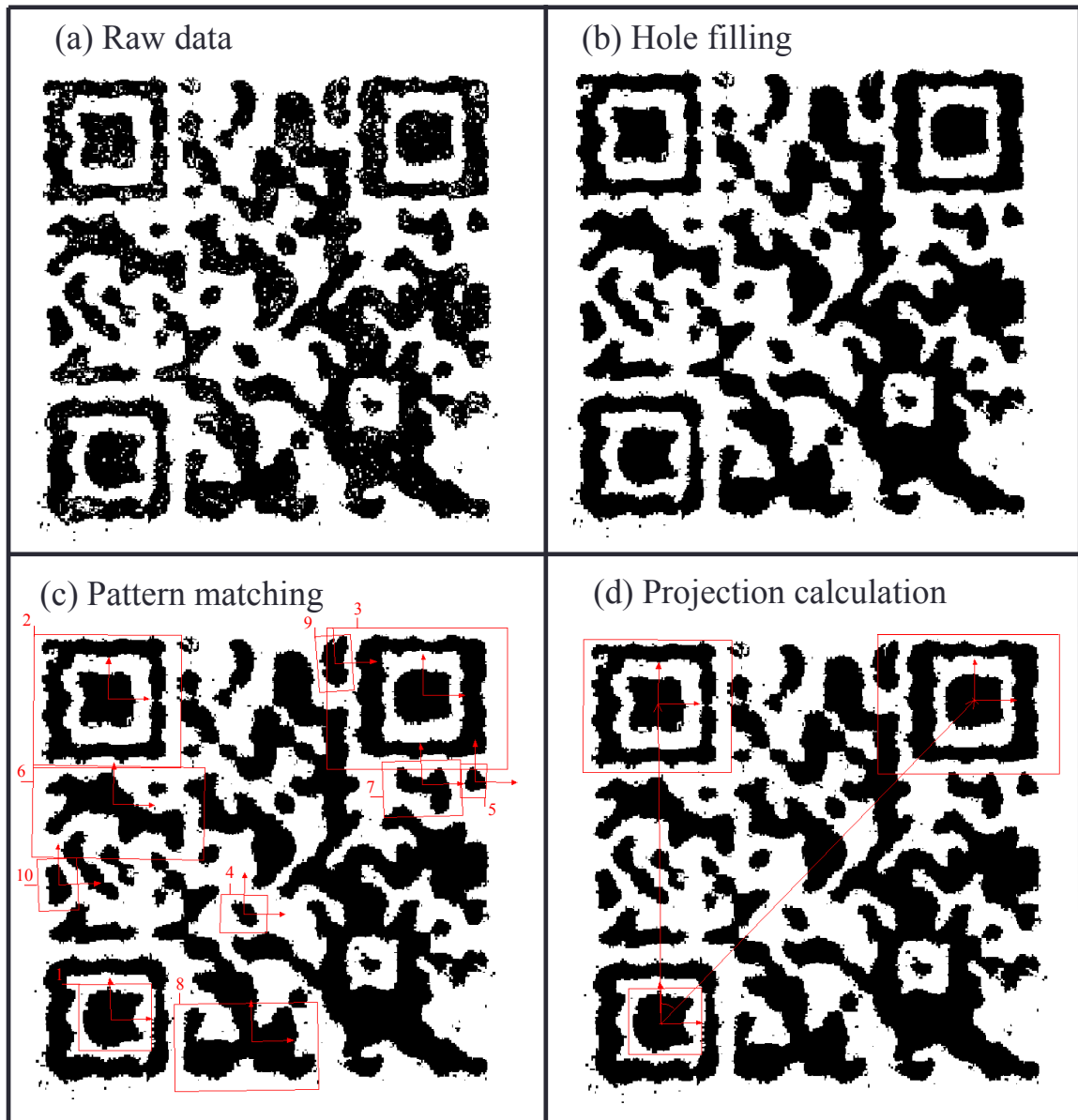
Figure 4.11 Depiction of image processing steps from (a) raw data, (b) hole filled, (c) pattern matching to (d) projection calculations

The selected features shown in Figure 4.11 (c) were chosen so that the majority of the scan was incorporated in the analysis. A coordinate system must first be established in order to complete the projection calculations and compare the distances between the features in all scans. The coordinate system ensures that the results are not influenced by

misalignments from the homing, which is not the primary objective of these tests. Figure 4.12 shows the coordinate system used throughout the analysis.
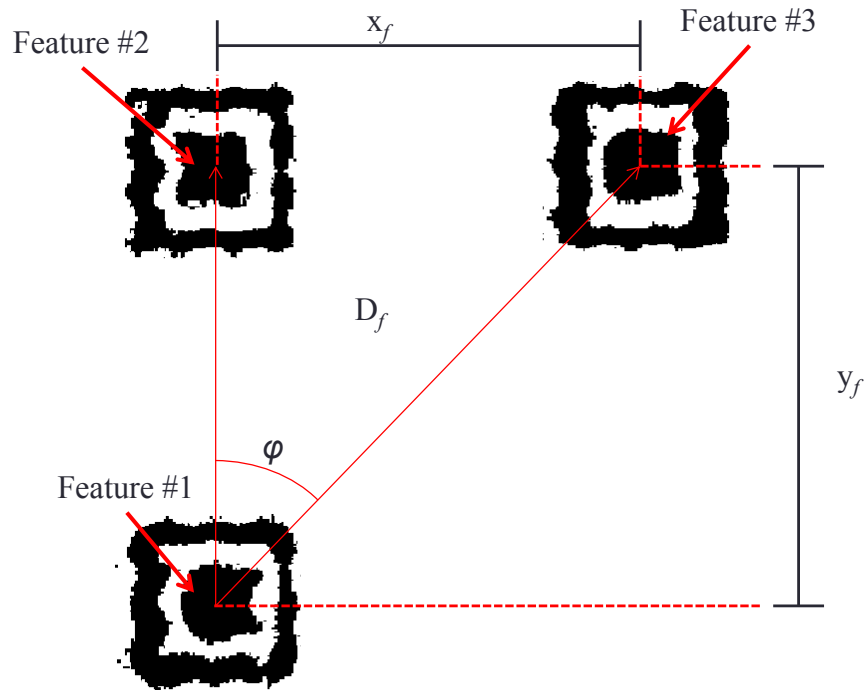
Figure 4.12 Coordinate system for projection calculations

Figure 4.12 demonstrates the distance and angle being measured for feature #3. Feature #1 represents the origin and the line between features #1 and #2 is used as a reference for all angles. Using the measure of the angle between the reference and the feature of concern φ and the distance from the origin to the same feature D_f, relative x and y distances to the feature (x_f and y_f) can then be calculated using the following projection equations:

$$x_f = D_f \cdot \sin(\varphi) \tag{4.1}$$

$$y_f = D_f \cdot \cos(\varphi) \tag{4.2}$$

4.2.2 QR Analysis Results

The analysis method previously described was used in order to quantify the repeatability of the grinding wheel scanner. The x and y distance calculations from the 1200 μm pen scan can be seen in Table 4.2 and Table 4.3. The mean distance $\bar{x}$ of the n scans were calculated for each feature in both the x and y directions. Their respected standard deviations σ were then calculated using Equation (4.3). The x and y direction had average standard deviations of 9.3 and 5.9 μm respectively, which gave percent errors from the mean of 2.1 and 1.0 %.

$$\sigma = \sqrt{\frac{\sum_{i=1}^{n}(x_i - \bar{x})^2}{n}} \qquad (4.3)$$

The x-direction values tend to deviate more which is likely due to the device being driven along the x-axis. When put into perspective with realistic grain sizes, the true effect of these errors can be understood. For example, using 300 μm for an average grain size of the wheel, these errors only account for 3 % in the x-direction and 2 % in the y-direction of one grain.

Table 4.2 1200 μm pen, x-direction results

Feature #	Distance in x-direction [μm]				Mean [μm]	σ [μm]	Error [%]
	Scan 1	Scan 2	Scan 3	Scan 4			
3	1529.2	1564.9	1551.1	1556.5	1550.5	13.2	0.9
4	885.5	896.4	883.8	884.2	887.5	5.2	0.6
5	2309.9	2357.3	2348.4	2338.4	2338.5	17.8	0.8
6	18.2	18.8	22.0	15.0	19.1	1.7	9.1
7	1999.9	2015.3	1991.9	2004.7	2002.9	8.5	0.4
8	896.4	918.6	915.6	920.7	912.8	9.7	1.1
9	1454.6	1473.1	1453.9	1461.5	1460.8	7.7	0.5
10	-328.8	-303.5	-310.4	-327.4	-317.5	10.9	3.4
Average						9.3	2.1

Table 4.3 1200 *μm* pen, y-direction results

Feature #	Distance in y-direction [*μm*]				Mean [*μm*]	σ [*μm*]	Error [%]
	Scan 1	Scan 2	Scan 3	Scan 4			
3	1836.2	1820.6	1825.2	1821.0	1825.8	6.3	0.4
4	677.3	668.9	678.2	686.1	677.6	6.1	0.9
5	1486.6	1481.6	1486.0	1506.3	1490.2	9.6	0.6
6	1368.6	1364.0	1372.5	1371.9	1369.3	3.4	0.3
7	1495.0	1470.8	1479.3	1493.7	1484.7	10.1	0.7
8	-141.6	-160.6	-150.3	-142.7	-148.8	7.6	5.1
9	2257.3	2257.8	2262.8	2260.3	2259.6	2.2	0.1
10	859.2	855.7	860.6	858.5	858.5	1.8	0.2
Average						5.9	1.0

The same experiment was also performed with the 130 *μm* pen in order to provide further validation and determine the effect of sensor spot size on the measurements. The results for the four scans can be seen in Table 4.4 and Table 4.5. It can be seen that the standard deviation in both the x and y directions have decreased to 8.1 and 5.7 *μm* respectively with the average percent errors being 1.3 and 0.8 %. Since all measurement parameters were kept constant throughout all experiments the slight improvements seen are presumed to be due to the decrease in sensor spot size.

Table 4.4 130 *μm* pen, x-direction results

Feature #	Distance in x-direction [*μm*]				Mean [*μm*]	σ [*μm*]	Error [%]
	Scan 1	Scan 2	Scan 3	Scan 4			
3	1566.3	1548.2	1560.8	1565.3	1560.1	7.2	0.5
4	878.2	875.9	870.2	896.5	880.2	9.9	1.1
5	2332.4	2352.4	2359.2	2355.7	2349.9	10.4	0.4
6	28.5	32.3	29.4	30.0	30.1	1.4	4.6
7	1995.3	2013.4	2030.5	2013.2	2013.1	12.4	0.6
8	892.9	886.6	897.7	919.8	899.3	12.5	1.4
9	1449.5	1435.7	1451.2	1445.0	1445.4	6.0	0.4
10	-319.6	-328.3	-315.8	-319.1	-320.7	4.6	1.4
Average						8.1	1.3

Table 4.5 130 *μm* pen, y-direction results

Feature #	Distance in y-direction [*μm*]				Mean [*μm*]	σ [*μm*]	Error [%]
	Scan 1	Scan 2	Scan 3	Scan 4			
3	1819.2	1824.1	1818.6	1831.2	1823.3	5.0	0.3
4	669.8	670.0	662.8	666.6	667.3	2.9	0.4
5	1485.4	1494.7	1481.5	1502.8	1491.1	8.3	0.6
6	1371.5	1372.6	1378.7	1371.7	1373.7	3.0	0.2
7	1480.2	1498.1	1480.6	1491.6	1487.6	7.6	0.5
8	-149.3	-139.1	-151.0	-142.9	-145.6	4.8	3.3
9	2271.6	2277.1	2270.5	2255.1	2268.6	8.2	0.4
10	843.2	850.2	855.2	859.3	852.0	6.0	0.7
Average						5.7	0.8

Another parameter of concern for the grinding wheel scanner is the size of the features scanned. The image analysis program was also capable of outputting the areas of the features. By performing the same analysis procedure as for the distances, the area measurements were compared for further validation. The results for the four scans taken with each optical pen were compared and summarized in Table 4.6 and Table 4.7.

By looking at the results it can be seen that the scanner was able to scan the areas within a very accurate range. When scanned with the 1200 *μm* pen the area measurements deviated an average of 1345.6 *μm*^{2} and had an average error of 2.0 % from the mean value. The 130 *μm* pen resulted in an average deviation and percent error of 548.1 *μm*^{2} and 0.7%, respectively. The 130 *μm* pen's significant improvement in repeatability is likely due to the difference in spot sizes. The 130 *μm* pen's spot size is 65% smaller than the 1200 *μm* pen, and there was an overall reduction of 60% in the deviation and 66% in error from the mean over all features. The smaller spot size evidently provides a higher resolution of the edges of the features. This observation can be used to explain why the results seen in the distance measurements were fairly similar. Although the 2.8 *μm* spot size does provide a more a more detailed edge, the effect is roughly the same on all sides which has little effect on the centroid of that feature. When compared to the average grain size 300 *μm,* these deviations only account for 1.9 and 0.8 % of the total area.

Table 4.6 1200 μm pen, area results

Feature #	Measured Area [×$10^4\mu m^2$]				Mean [×$10^4\mu m^2$]	σ [×$10^4\mu m^2$]	Error [%]
	Scan 1	Scan 2	Scan 3	Scan 4			
1	10.35	10.04	9.54	9.73	9.91	0.31	3.1
2	11.41	11.41	11.75	11.75	11.58	0.17	1.5
3	10.52	10.42	10.31	10.21	10.36	0.12	1.1
4	1.48	1.56	1.48	1.55	1.52	0.04	2.4
5	1.25	1.27	1.21	1.15	1.22	0.05	3.8
6	19.95	19.75	19.55	19.36	19.65	0.22	1.1
7	5.65	5.54	5.37	5.10	5.42	0.21	3.8
8	25.71	25.45	25.45	25.71	25.58	0.13	0.5
9	4.19	4.19	4.19	4.02	4.15	0.07	1.8
10	3.09	3.09	3.06	3.00	3.06	0.04	1.2
Average						0.13	2.0

Table 4.7 130 μm pen, area results

Feature #	Measured Area [×$10^4\mu m^2$]				Mean [×$10^4\mu m^2$]	σ [×$10^4\mu m^2$]	Error [%]
	Scan 1	Scan 2	Scan 3	Scan 4			
1	10.78	10.57	10.79	10.65	10.70	0.04	0.9
2	10.58	10.71	10.54	10.74	10.64	0.08	0.8
3	10.92	11.12	10.88	10.93	10.96	0.09	0.8
4	1.47	1.46	1.47	1.47	1.47	0.01	0.3
5	1.20	1.20	1.20	1.20	1.20	0.00	0.0
6	20.31	20.32	20.04	20.12	20.20	0.12	0.6
7	5.95	6.03	6.02	5.98	5.99	0.03	0.5
8	26.04	25.97	26.08	26.01	26.03	0.04	0.2
9	4.42	4.36	4.33	4.34	4.36	0.04	0.8
10	3.00	2.93	3.05	3.03	3.00	0.04	1.5
Average						0.05	0.7

Another measure that was also extracted from the image processing analysis program was the overall capability of the homing system. Monitoring the coordinates of the origin feature's centroid for each scan allows for a comparison of the relative x and y positions. Since the centroids of the features were not highly affected by the optical pen it is

reasonable to analyze all measurements together. Table 4.8 shows the x and y coordinates of feature #1 throughout both sets of experiments. The average deviation seen along x-axis was 27.6 μm and 19.3 μm along the y-axis. This result means that the system is capable of homing to within roughly the size of a human hair. Acknowledging the amount of sources for error in such a system these values were deemed to be acceptable.

Table 4.8 Homing capability

		X Position [μm]	Y Position [μm]
1200 μm Pen	Scan 1	521.3	2498.5
	Scan 2	484.4	2499.3
	Scan 3	549.7	2484.0
	Scan 4	523.6	2508.7
130 μm Pen	Scan 1	518.4	2527.7
	Scan 2	508.8	2537.1
	Scan 3	467.2	2541.2
	Scan 4	553.8	2501.8
Mean		515.9	2512.3
σ		27.6	19.3

Overall, the QR code tests provided sufficient evidence that the positioning system of the grinding wheel scanner is more than capable of scanning a grinding wheel. The resulting percent errors for both pens are summarized in Table 4.9. It also confirmed that given the considerable amount of sources of error, the homing system works appreciably well. Using a smooth metal wheel presumably gives a worst-case scenario repeatability measurement. The x-axis positioning is based on a friction drive system and the coefficient of friction of smooth metal is drastically lower than that of a coarse grinding wheel.

Table 4.9 QR repeatability summary

Pen	X Position [%]	Y Position [%]	Area [%]
1200 μm	2.1	1.0	2.0
130 μm	1.3	0.8	0.7

4.3 Grinding Wheel Validation

With the repeatability of the scanner now quantified based on position, it is time to incorporate the main component: the grinding wheel. The randomness in size and shape of the grains adds a layer of difficulty to the validation process and, therefore, much of the validation is performed by comparisons.

4.3.1 Pen Selection

Two optical pens have been used thus far to validate the system but for grain monitoring it would not be practical to continue using both pens. Since the measurement principle is based on the reflectivity of the white light, it is possible that the pens could result in different measurements when looking at the same area. In order to test this theory, the same area was scanned on a WA 46J vitrified aluminum oxide grinding wheel using both pens. The grinding wheel was made up of Al_2O_3 abrasive grains with an average size of 0.32 mm in diameter, held together by a vitreous bond. The wheel had a 32% porosity. Figure 4.13 shows the top 75 μm of the two scanned areas.
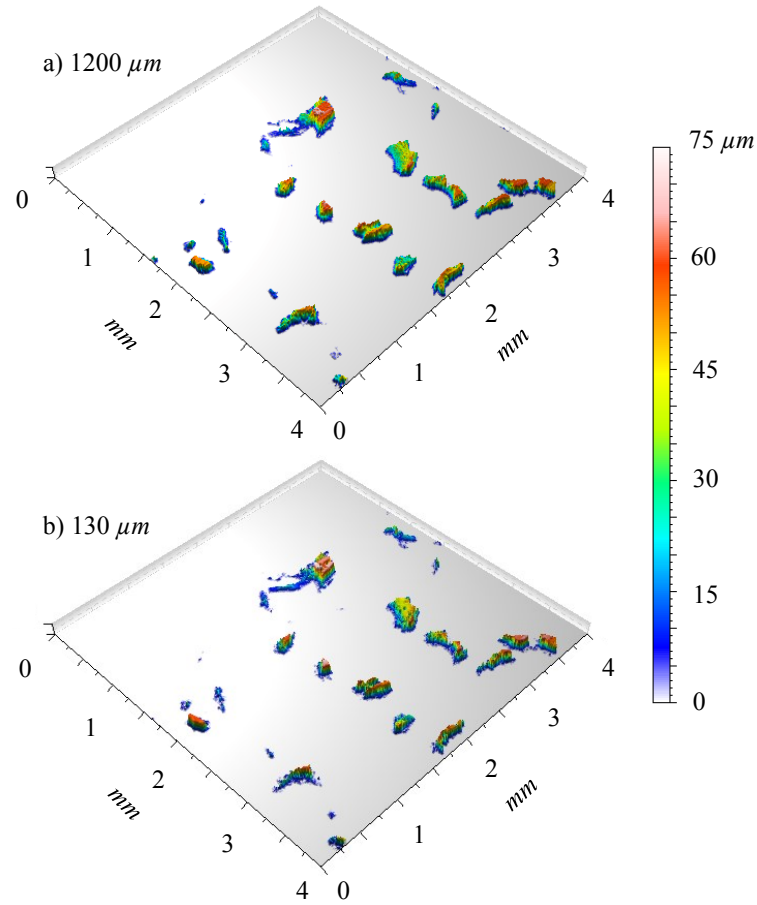
Figure 4.13 Grinding wheel topography with (a) 1200 *μm* pen and (b) 130 *μm* pen

Despite the fact that the 130 *μm* pen can measure to a depth of 130 *μm,* the scan in Figure 4.13 shows only the top 75 *μm* due the difficulty in manually adjusting the standoff distance perfectly. It is evident from Figure 4.13 that both pens have measured the same area and, at first glance the two scans look very similar. The differences between the two pens become more obvious by examining smaller areas of the scan. Figure 4.14 shows a comparison between areas scanned with the 1200 and 130 *μm* pens and a digital photo taken of the same area.

Area 1	Area 2
(a)	
(b)	
(c)	
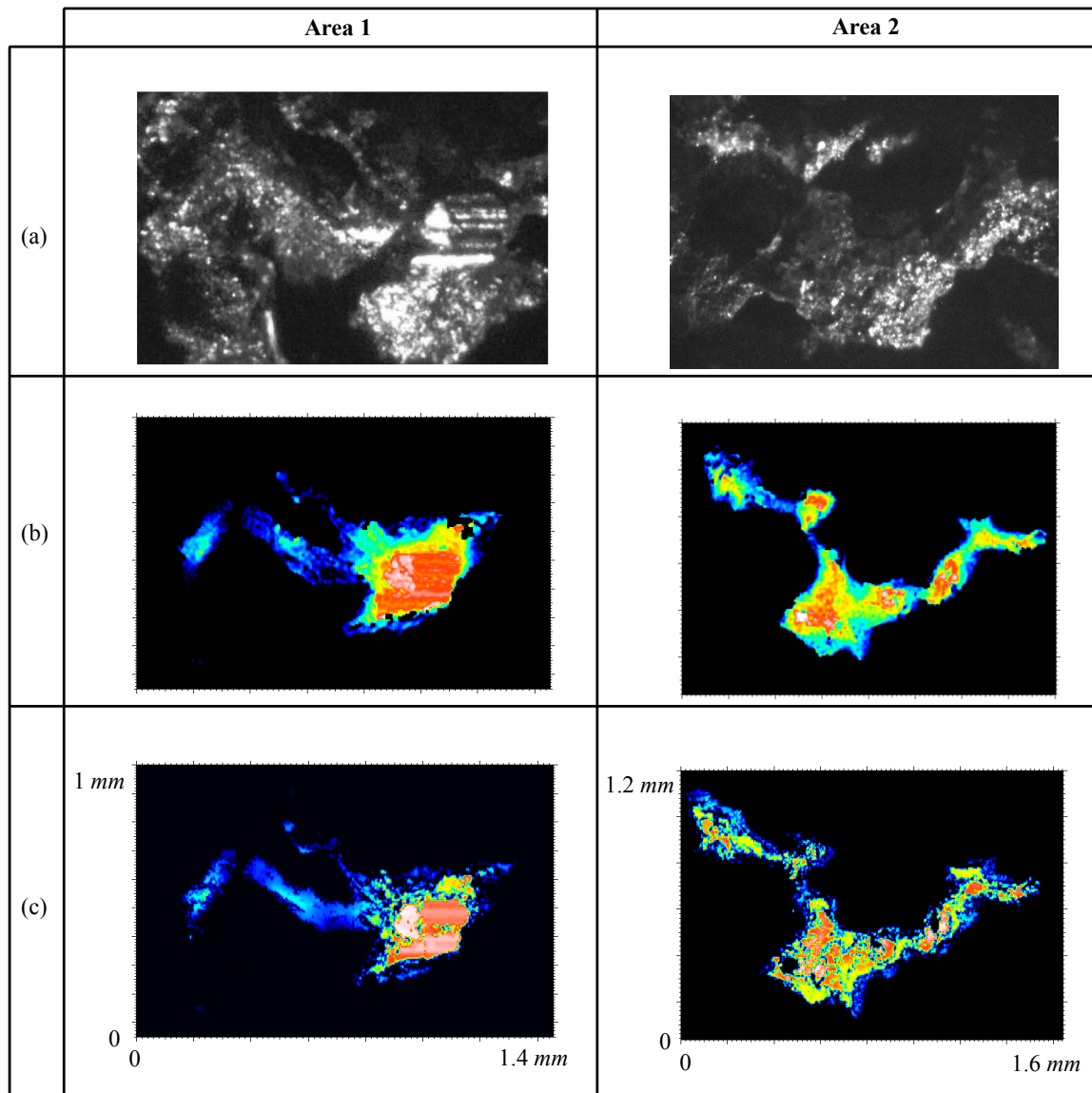
Figure 4.14 Comparison of scanned grains with (a) digital image, (b) 1200 μm pen and (c) 130 μm pen

By comparing the scanned areas in Figure 4.14(b) and (c) to the digital image in Figure 4.14 (a) it is clear that both pens capture the shape and distinctive features of the grains accurately, however, the two pens result in significantly different looking scans. The 130 μm pen is much more sensitive than the 1200 μm and for that reason there appear to be many small broken up portions throughout the grains. Due to the 130 μm pen's small measurement range it also proves very difficult adjust the distance of the pen to ensure

the entire scan will be within the range of the pen whereas the 1200 *μm* pen has a larger range to accommodate for the randomness of the grains. Another aspect to consider is that it is currently unknown at what depth into the wheel is meaningful for research purposes. All of these factors contributed in the decision that the remaining scans for this work will be taken with the 1200 *μm* optical pen.

4.3.2 Scan Validation

The main objective of the grinding wheel scanner is to be able to monitor the grains throughout grinding experiments. With the pen selected, a preliminary surface grinding experiment was performed in order to validate the scanner's capabilities in measuring the grinding wheel grains. The experiment was performed on a Blohm Planomat grinder with a 4140 steel workpiece. The grinding wheel was trued and dressed using a diamond single point-dressing tool. The dressing depth was 1 *μm* and an overlap ratio of 3 was used. The wheel was then used to grind the workpiece with a 10 *μm* depth of cut. The workpiece velocity was 0.21 *m/s* and the tangential wheel velocity was 25 *m/s*. The workpiece was 6.35 *mm* wide and 156 *mm* long, resulting in 9.9 *mm³* of material being removed each pass with a material removal rate of 13 *mm³/sec*. A total of 2500 passes were performed in order to ensure the wheel had been sufficiently worn. The grinding wheel scanner was then used to measure two 5x6.5 *mm* areas of the wheels surface, one worn and one unworn. The sampling interval was 5 *μm* in each direction. Figure 4.15 below shows the difference between an unworn and worn section of the wheel.
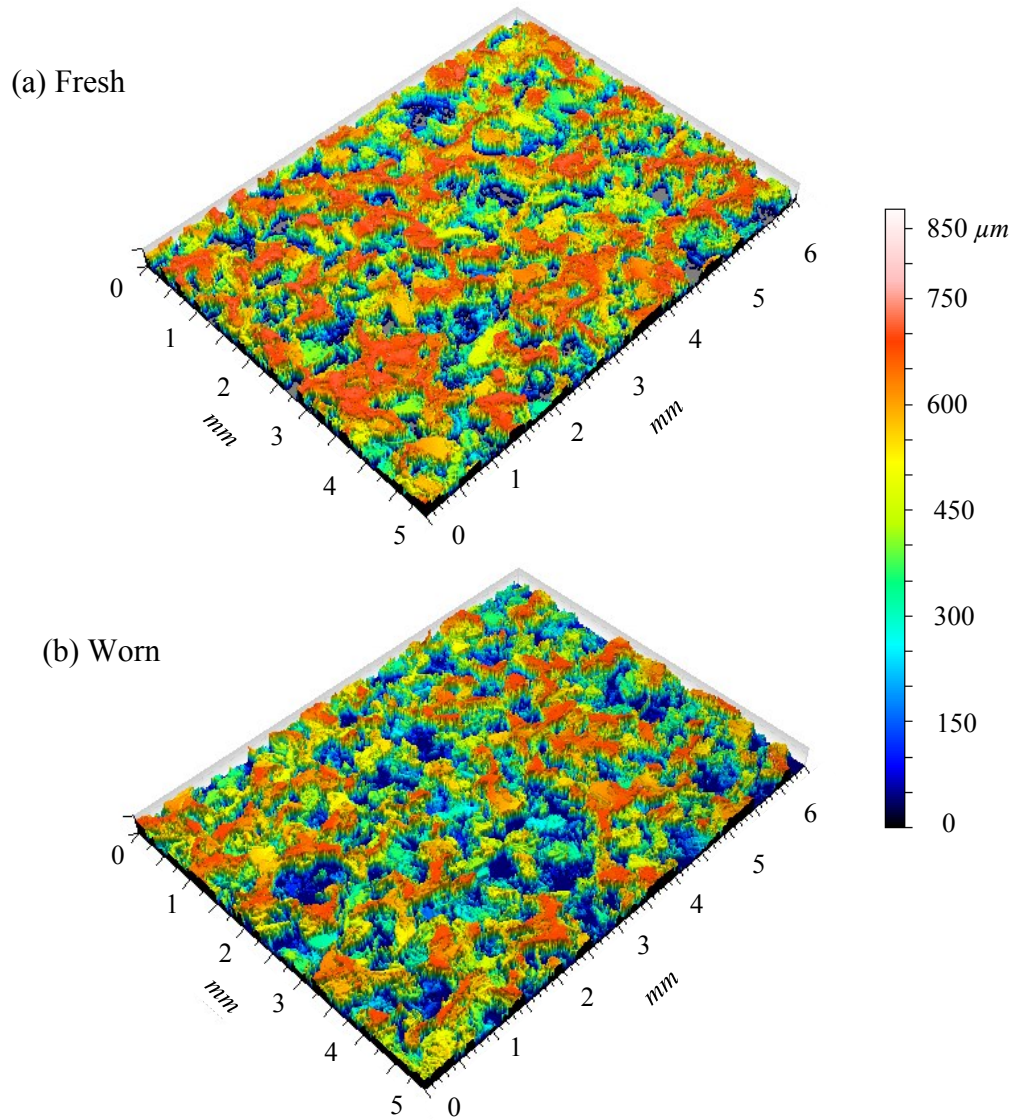
Figure 4.15 Grinding wheel topographies for (a) fresh and (b) worn sections.

Visually comparing the two images one can see that the newly dressed portion in Figure 4.15 (a) has significantly more amount of red or high areas. To say that two scans look different however does not fully validate the system. The measured portion of the wheel was cut out using a Pro.Point Turbo Diamond Cutting Blade and then scanned using a Hitachi S-4700 Field-Emission SEM. Figure 4.16 shows a comparison of a scanned area to an image from the SEM for a fresh section of the wheel.
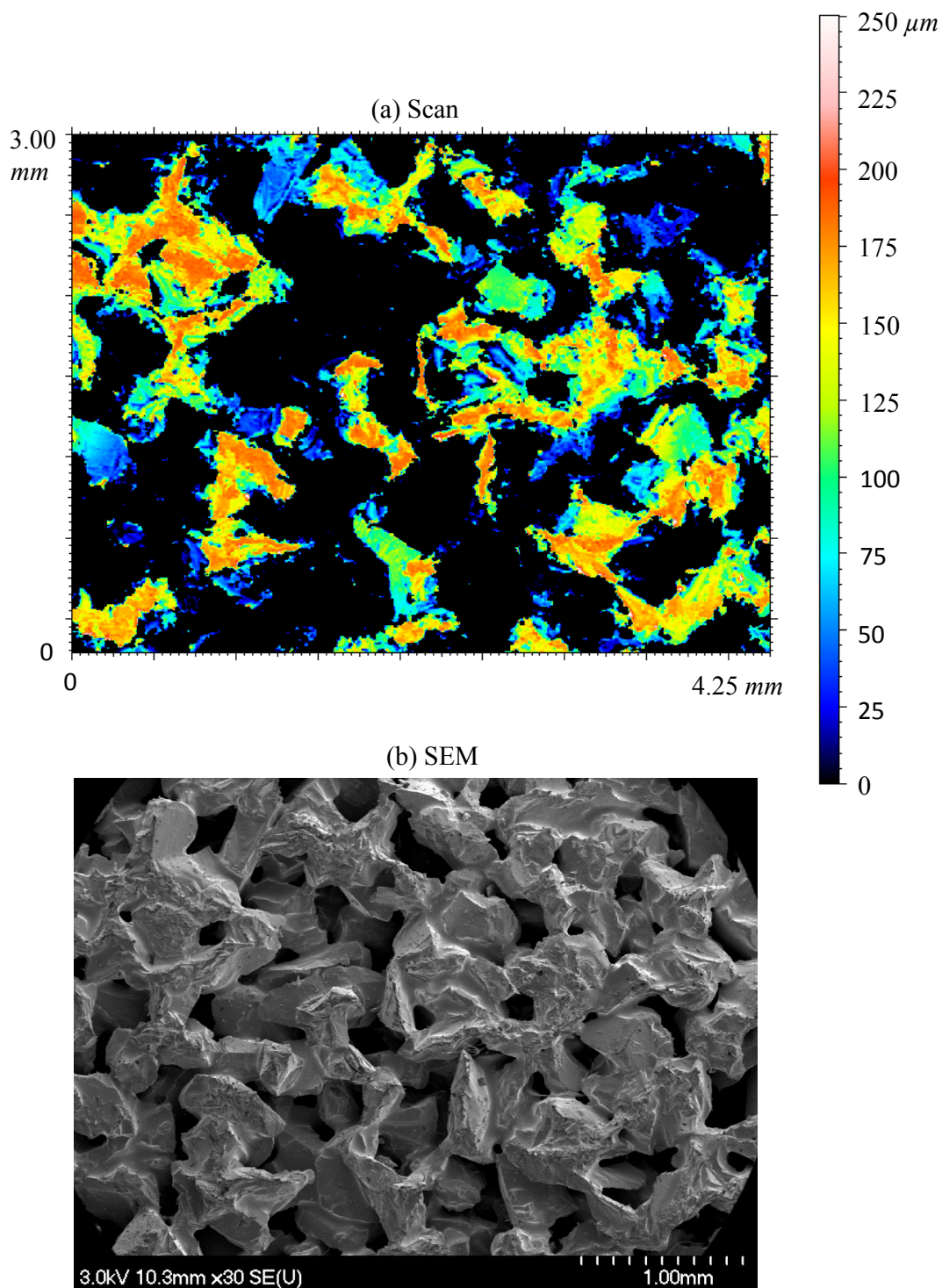
(a) Scan

(b) SEM

Figure 4.16 Comparison of (a) scanner measurement and (b) SEM image

The features in Figure 4.16 (a) can easily be seen in Figure 4.16 (b). The images from the SEM can be used to confirm that the measurements from the grinding wheel scanner are comparable. The area of three easily distinguishable features in the SEM were estimated using a pixel counting technique and then compared to the grinding wheel scanner measurements. Figure 4.17 shows the three distinguishable areas used in (a) Scanned area and (b) SEM.
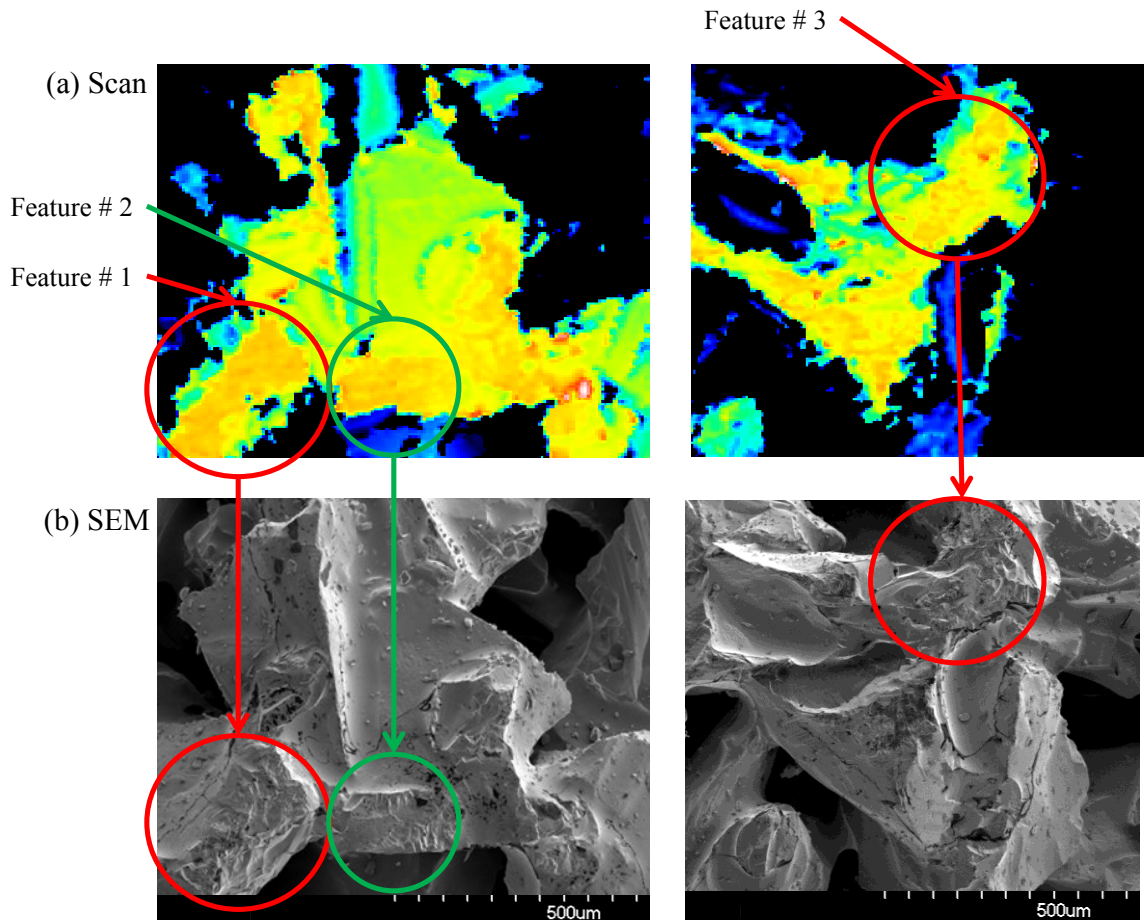

Figure 4.17 Distinguishable features used for area measurement comparison with (a) scan and (b) SEM

Digital Surf Mountains Software was was used to threshold the height of the scan so that only the feature of concern was visible. A surface area measuring algorithm was then used to compute the surface as shown in Figure 4.18, which depicts the measuring of

Feature #1. By selecting a set of points around the object of concern the program computes its surface area and volume.

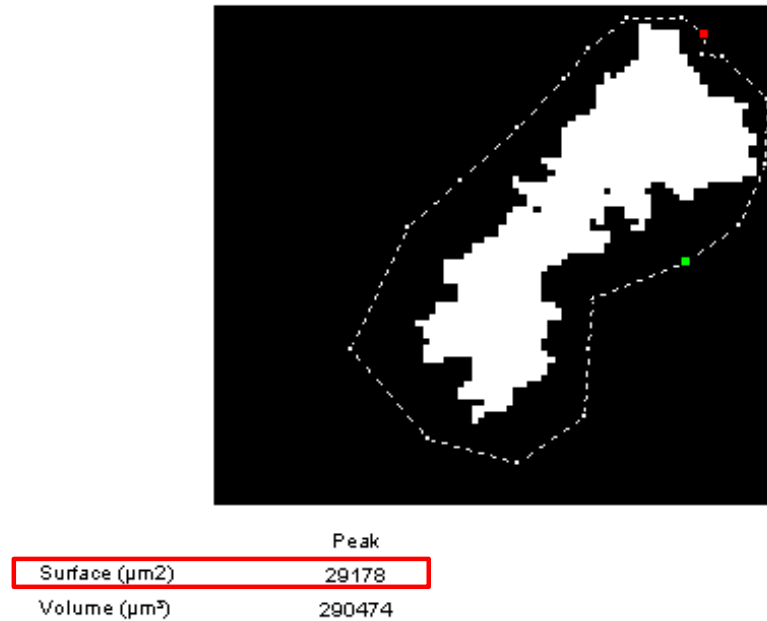|	Peak
Surface (µm2)	29178
Volume (µm³)	290474

Figure 4.18 Feature #1 example with Mountains Software surface area measurement tool

To compare the grinding wheel scanner data to the SEM, the areas of the same features must be measured using pixel counting. The large number of pixels in the image make this a difficult task. Overlaying a 10x10 pixel grid onto the SEM decreased the amount of time to count the pixels significanlty without affecting the results due to the total size of the area. Based on the maginification of the SEM each pixel was 1x1 μm, therefore each grid block contained a surface area of 100 μm^2. In order to measure the edges of the features, an approximation was made in ¼ increments. Essentially, if a small portion of the block contained the feature then only 25 μm^2 were added to the sum, and so on. Figure 4.19 demonstrates the grid counting technique used on an edge of Feature #1. In this example the different colours of grids correspond to the fraction of grain which was contained in that grid.
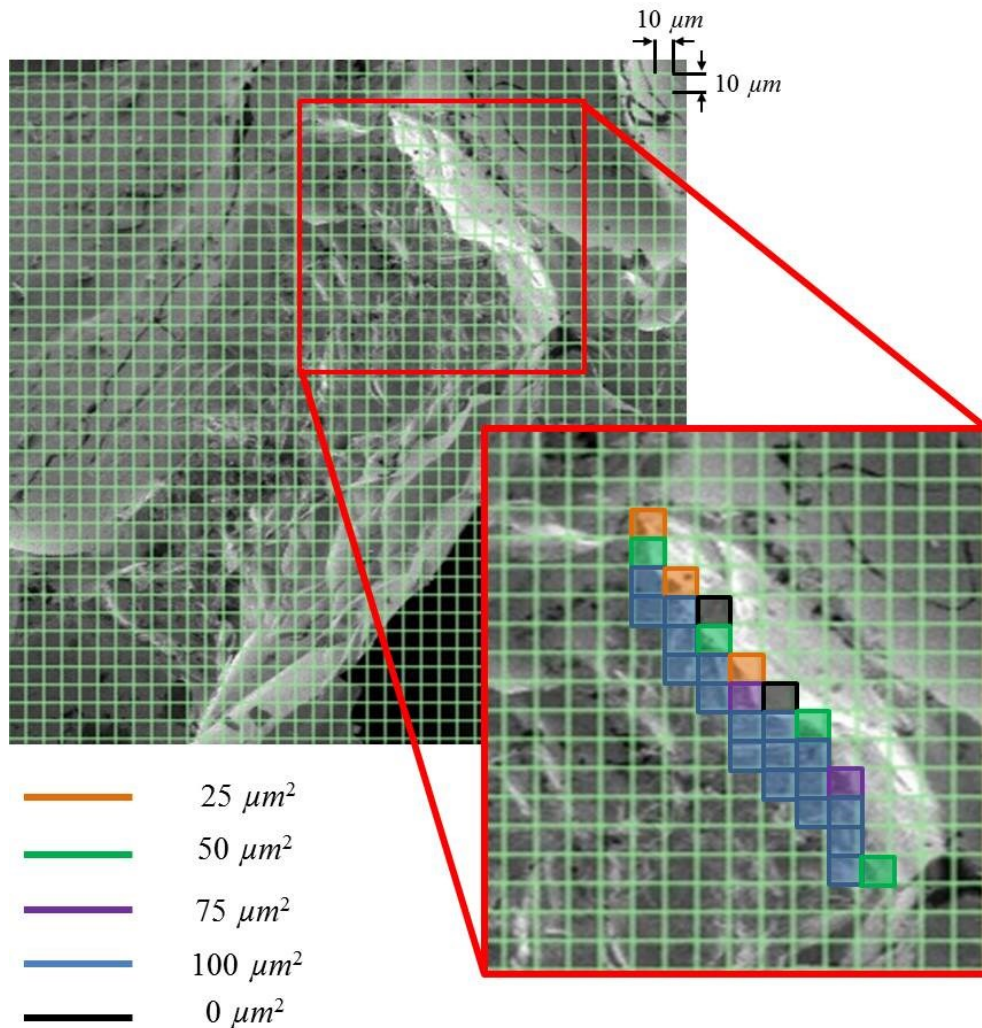
Figure 4.19 Grid counting method for Feature #1

The measurements of the three distinguishable features are summarized in Table 4.10. The average percent difference between them was 9.7%. This value is likely a result of the subjectiviity during the manual edge definition. Overall, the agreement between results confirm the scanners ability to measure the wheels surface accurately.

Table 4.10 Area comparison results

	Area measurements $[\times 10^4\ \mu m^2]$		
Feature	Grinding Wheel Scanner	SEM	% Difference
1	2.9	2.6	11
2	2.6	2.4	9
3	4.1	3.7	9

A comparison of worn and fresh grains can also be used to further validate the scanner's capabilities. The grinding parameters chosen for this experiment were selected based on the work of Lachance et al. [29]. The goal was to induce more attritious wear than fracture wear so that the tops of the grains could be used to validate the difference between worn and fresh grains. Figure 4.20 (a) shows worn and fresh grains with an SEM and the grinding wheel scanner. Commercially-available Mountains Software was then used to extract a profile along the grains to compare the difference seen in Figure 4.20 (b) and (c).
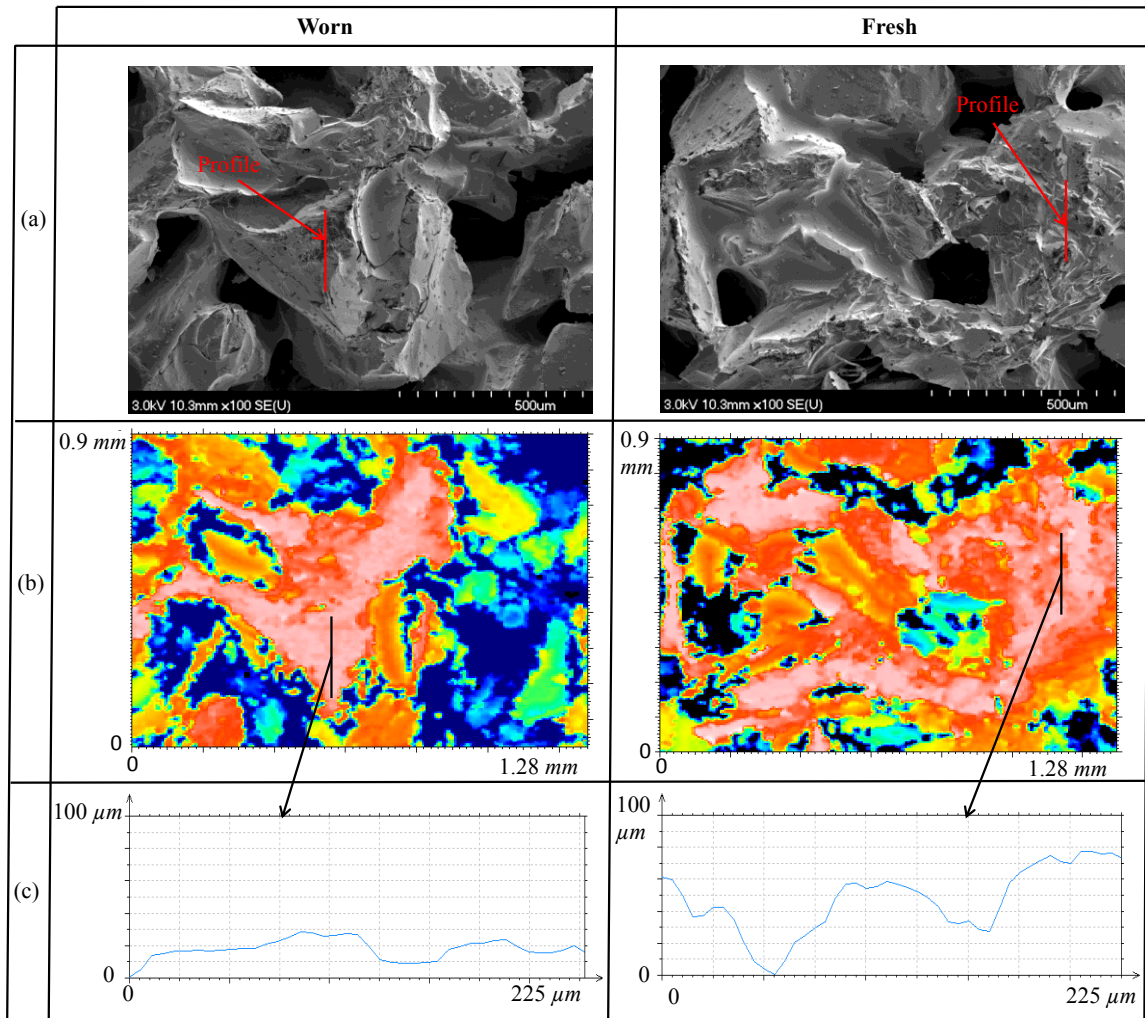
Figure 4.20 Grain comparison between worn and unworn with an (a) SEM and (b) grinding wheel scanner and (c) corresponding profiles

The worn grain in Figure 4.20 (a) appears to be much smoother than the fresh grain. The red line represents the profile that will be taken. Figure 4.20 (b) is the same area taken with the grinding wheel scanner. It is more difficult to clearly see the differences due to the large verticle scale. The profiles seen in Figure 4.20 (c) clearly show the differences between the two. By calculating the arithmatic average of the profiles the *Ra* values were obtained. The worn grain only varries within a range of 30 *μm* and has a *Ra* value of 2.03 *μm* while the fresh grain varies within a range 80 *μm* and has a *Ra* value of 6.21 *μm*. This

result demonstrates that the grinding wheel scanner is capable of measuring the difference between used and fresh grains.

The size of features and there morphology are important parameters, but the validation process has yet to examine the spacing between features which is analogous to the cutting edge spacing measurement. Fusing an image from the SEM with the grinding wheel scanner measurement can demonstrate, for illustration purposes, that the measurements are correct. Figure 4.21 shows the process of this fusion at different SEM transparency levels. The transparency level of the SEM image was decreased from 100 to 0% in increments of 20% throughout six images.
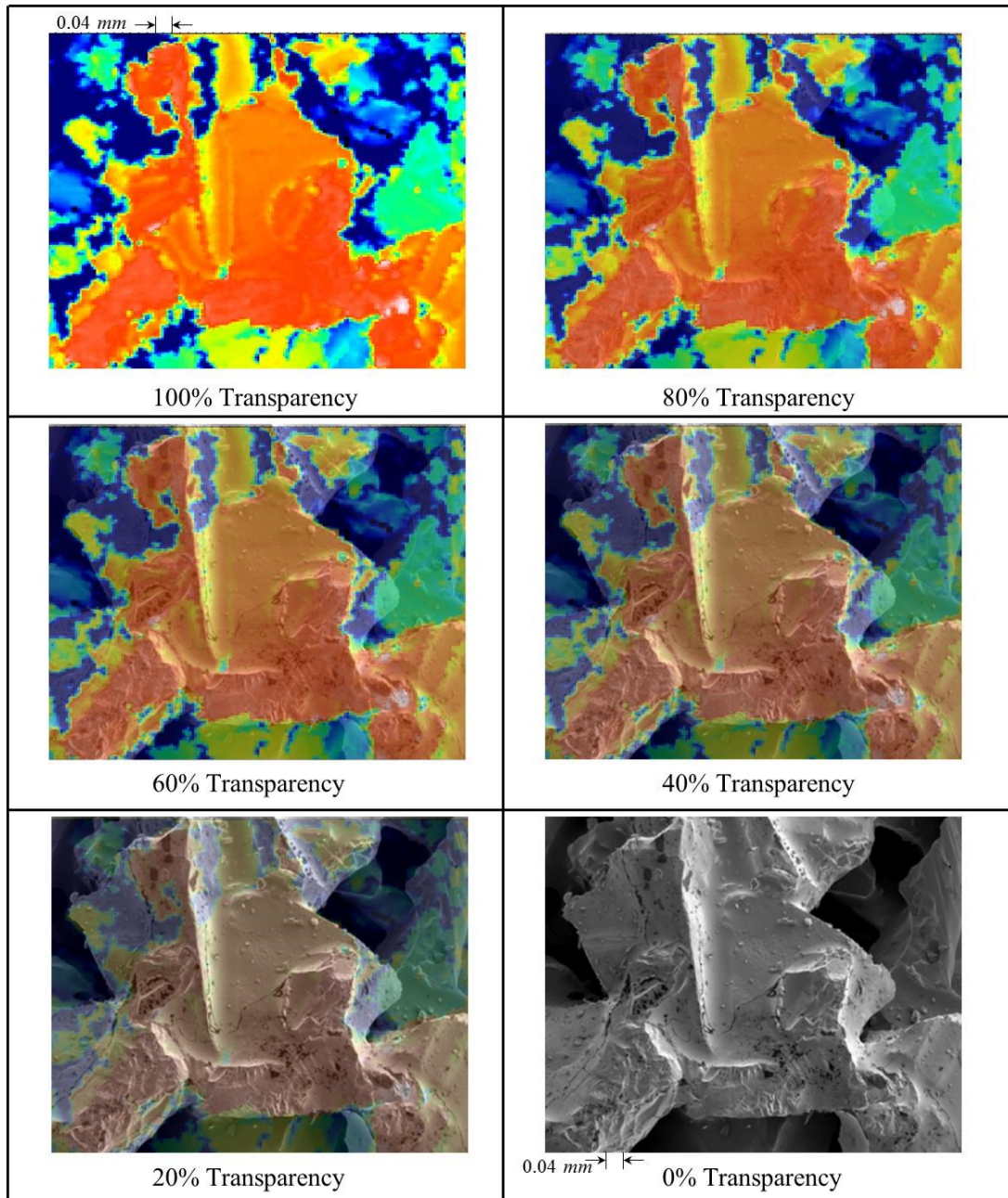
Figure 4.21 Fusion of grinding wheel scanner data and SEM

The transparency levels were decreased in order to emphasize the alignment of features. The red or high points in the scan seem to line up nearly perfectly with distintive ridges in the SEM image.

As grinding progresses, chips from the workpiece can become lodged in the wheel. This wheel loading is an unavoidable characteristic of grinding and it causes problems both in the process itself and also in measuring the grinding wheel surface. In particular, wheel contamination becomes an issue during scans when the object rests above the surface of the wheel. Figure 4.22 demonstrates this effect of wheel contaminate.

Figure 4.22 Effect of wheel contaminate on scanner measurements

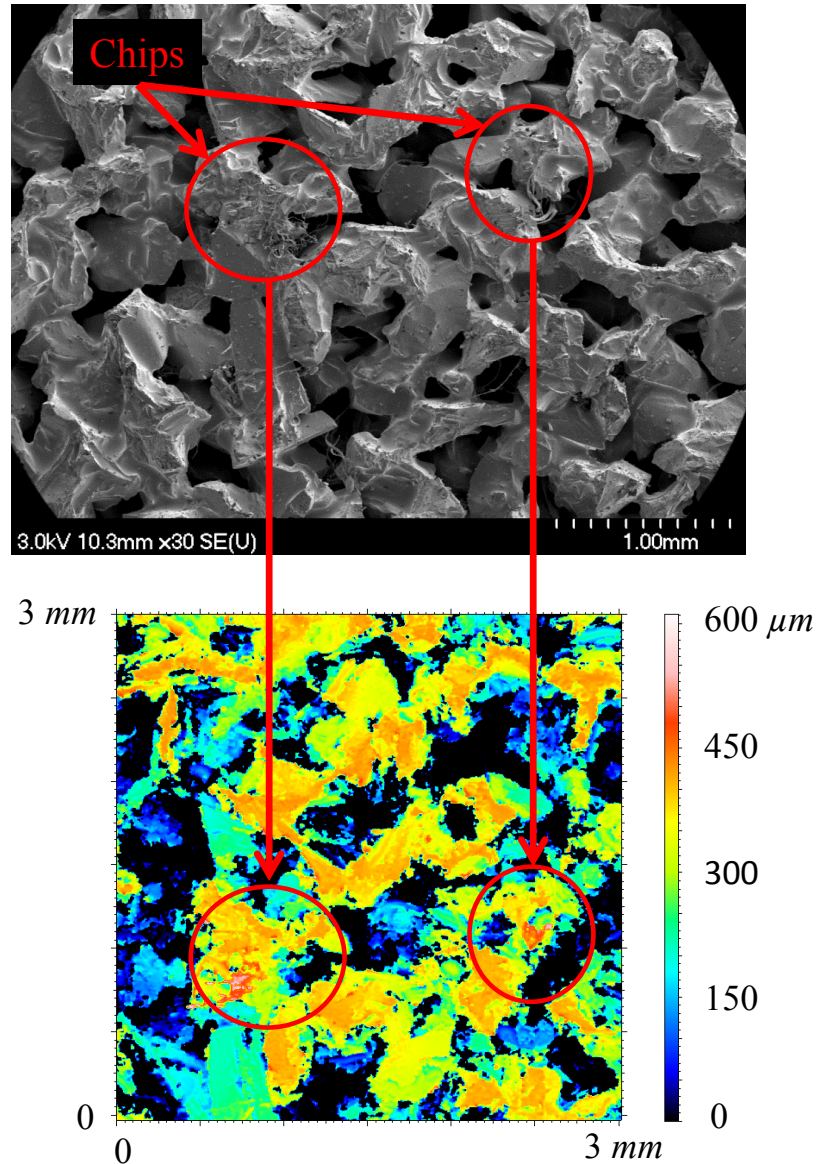The chips in the wheel are clearly visible from the SEM. Their effect on the scan can then be seen in the wheel surface colour map. Chips above the wheel surface will cause the sensor to detect a height that is not realistic. The tops of the grains shown in Figure 4.22 all lie at an approximate height of 400 μm. In the areas where chips are present the scan increases to a height of 600 μm. This sudden rise in height is not realistic and if a grain really had such a feature it would simply break rather than contribute to material removal. Regardless of the issue, this phenomena does contribute to the validation in the scanner as it proves that large spikes seen throughout the scan are not false measurements but are in fact workpiece chips.

4.4 Summary

This chapter presented the validation process for the grinding wheel scanner. A slip compensation algorithm was first developed for slippage seen in 2D profile measurements. It was discovered that the accuracy of the pen had a large effect on the slip correction results. Next a QR code was measured and the repeatability of the scanner was quantified using image analysis. When used with the 1200 μm pen, the scanner was able to measure the distance between features in the x and y directions with percent errors of 2.1 and 1.0%, respectively. The repeatability of its area measurements was found to be within 2% throughout the four measurements. Using the 130 μm pen had a small effect on the x and y distance measurments, resulting in percent errors of 1.3 and 0.8% for the x and y directions. The area measurements improved subtantially with the 130 μm with an error of 0.7%. Overall if compared to an average grain diameter of 300 μm these errors only account for a maximum of 3% of one grain. Using the QR code the homing was also validated and quantified to be repeatable with standard deviations of 27.6 and 19.3 μm for the x and y directions, respectively. A grinding wheel was then scanned with both pens and it was deemed accetable to perform grinding wheel scans with the 1200 μm pen. A aluminum oxide wheel was then ground and measured using the scanner. A manual pixel counting method was then used to compare SEM images to the grinding wheel scanner and they were found to be within 11% of each other. The surfaces of two grains, one worn and one fresh, were found to have Ra values of 2.0 and 6.2 μm, respectively. An SEM image was then overlayed onto a colour map from the scanner measurement and

the distinguishable features lined up exceptionally well. Spikes seen in the scanner measurements were then investigated using SEM images and it was found that they corresponded to chips lodged in the wheel.

Chapter 5. Wear Study

In this chapter the grinding wheel scanner was used to investigate the wear of grooved and non-grooved grinding wheels. Methods were developed in order to extract pertinent information from the grinding wheel scan including; number of particles, particle width and total surface area. The extracted parameters were then analyzed for both grooved and non-grooved wheels. A direct comparison of the radial and volumetric wear of the wheels was then performed using the extracted parameters. The extracted parameters also allowed for the comparison of cutting edge spacing for both wheels.

5.1 Grooved Grinding Wheels

Grooving the wheel surface has been proven to induce several beneficial characteristics in the grinding process. Nakayama et al. [47] were the first to perform an investigation with grooving, and found that a helically grooved wheel resulted in a 30% reduction in the grinding forces and consumed energy. Okuyama et al. [48] showed that by grooving a grinding wheel axially they were able to increase the maximum heat transfer coefficient. Mohamed et al. [49] reported a decrease of up to 61% in consumed power by grooving the wheel circumferentially. The circumferential groove was also proven to allow for up to 120% deeper cuts without damaging the workpiece or grinding wheel. Mohamed et al. also discovered that circumferentially grooved grinding wheels could grind for longer periods between dressing cycles [49, 50]. Considering all of the reported benefits of grooving the grinding wheel it was decided to use the grinding wheel scanner to investigate the wear of circumferentially grooved grinding wheels. Figure 5.1 shows the grinding wheels that were used for the study.
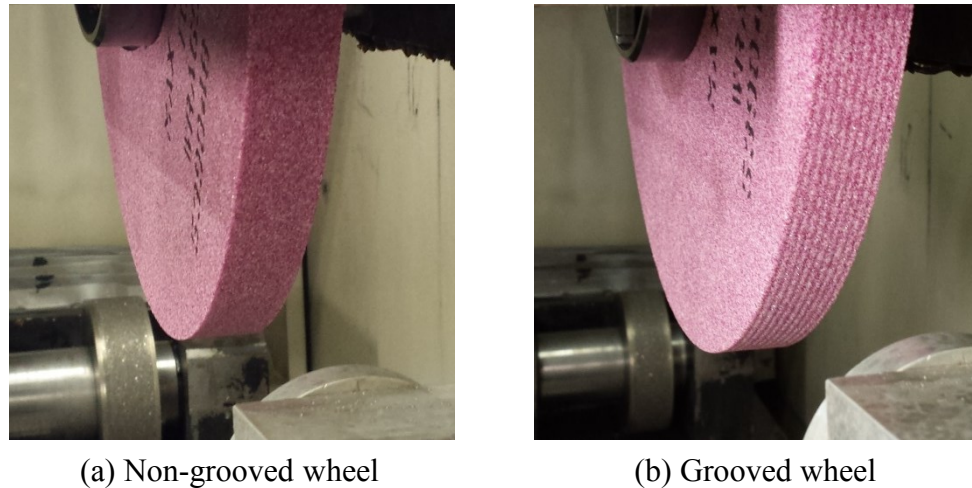
| (a) Non-grooved wheel | (b) Grooved wheel |

Figure 5.1 Grinding wheel surface for (a) non-grooved and (b) grooved wheels

The images shown in Figure 5.1 are of the same grinding wheel, but in Figure 5.1 (b) the wheel was grooved circumferentially using the method developed by Mohamed et al. [49]. The two main parameters used to describe the groove geometry are the groove width and depth, as shown in Figure 5.2.
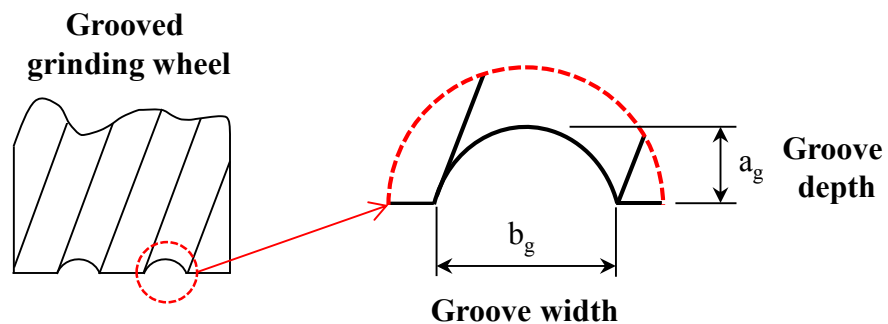

Figure 5.2 Groove geometry

Another useful term in discussing grooved grinding wheels is the "groove factor", which was introduced by Verkerk [51]. The groove factor represents the amount of non-grooved surface area remaining after the grooving process. For example, a grinding wheel which has not been grooved would have a groove factor of 100%.

5.2 Method

Grinding experiments were carried out on a Blohm-Planomat 408 creep-feed grinding machine with a Radiac Abrasives WRA 60-J5-V1 aluminum oxide grinding wheel. The wheel's grains had an average size of 0.220 *mm* and were held together with a vitrified bond. The groove parameters were selected based on the work of Mohamed et al. [49, 50]. A groove factor of 50%, groove depth of 0.0889 *mm* and groove width of 1.4 *mm* was reported to perform the best and therefore chosen for this study. Annealed AISI 4140 steel was used as the workpiece with a length of 153.9 *mm* and a width of 6.25 *mm*. Throughout all experiments, the grinding depth of cut, wheel speed, and workpiece speed were kept constant at 1.0 *mm*, 22.4 *m/s*, and 1.7 *mm/s*, respectively. A cutting-fluid concentration of 5.1% CIMTECH 310 was used and the fluid was delivered to the grinding zone at 50.4 L/min.

The grinding power was measured using a Load Controls Inc. PH-3A power transducer. A Kistler 9275B force dynamometer with a 5019B charge amplifier was used to measure the grinding forces. A system consisting of a National Instruments BNC 2120 connector block linked to a National Instruments PCI-MIO-16XE-10 data acquisition board controlled with a National Instruments LabVIEW code was used to collect all measurements at a sampling frequency of 500 *Hz*. The arithmetic mean surface roughness *Ra* of the workpiece was measured after every pass using a MahrFedral Inc. Pocket Surf.

The grinding wheel scanner was used to measure the same 7x7 *mm* area of the wheel surface after 4 and 8 passes for the non-grooved and grooved wheels, respectively. The scan size was selected to ensure that enough data was captured to fully represent a grinding wheel based on the work of Darafon et al. [38]. The scan increment was a tradeoff between scanning time and wheel wear rate. Each scan takes roughly 8 hours and then more time is required to perform the grinding and both setups.

5.3 Analysis

After performing the grinding experiments and collecting wheel topography measurements from the scanner it was essential to have a method of quantifying the differences seen between grinding wheels. Figure 5.3 shows scans of 4x7 *mm* sections of both wheels before and after the grinding experiments were performed.
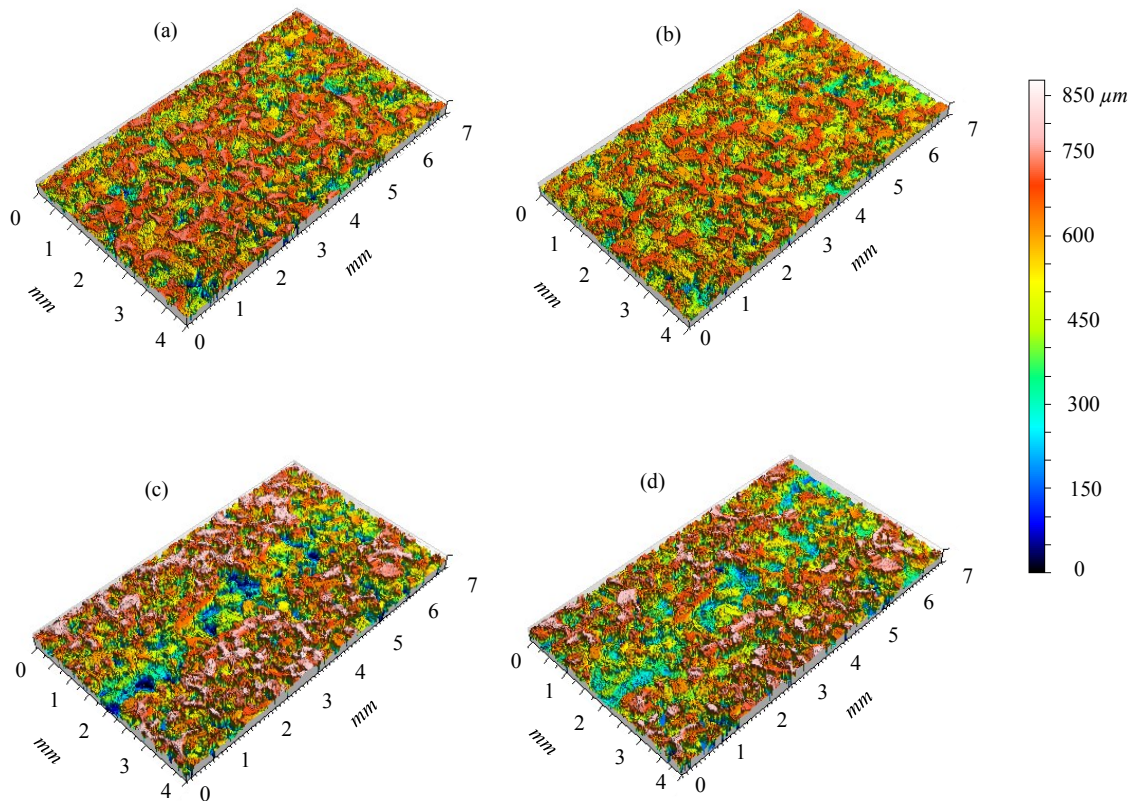

Figure 5.3 Grinding wheel surface topographies for (a) fresh non-grooved, (b) worn non-grooved, (c) fresh grooved and (d) worn grooved wheels

While the wheel surfaces are clearly different, it is difficult to quantify these differences without an automated analysis method. Darafon et al. [38] used the blob analysis method in which they were able to extract grain information from 3D grinding wheel scans. Blob analysis functions by applying a threshold plane to the scanned data. All features that are over the set threshold are turned into a binary image and can be analyzed using image

analysis techniques. Figure 5.4 demonstrates how blob analysis works with cone-shaped cutting edges. The method developed by Darafon et al. [38] has been modified for this research and now accepts an image with 16-bit colour depth rather than an 8-bit, allowing for a more detailed analysis. Figure 5.4 shows an example of the three parameters that were extracted from the scans, are as follows:

- Number of particles: The number of individual particles that are in the binary image.

- Average particle width b_p: The average width of all particles in the image.

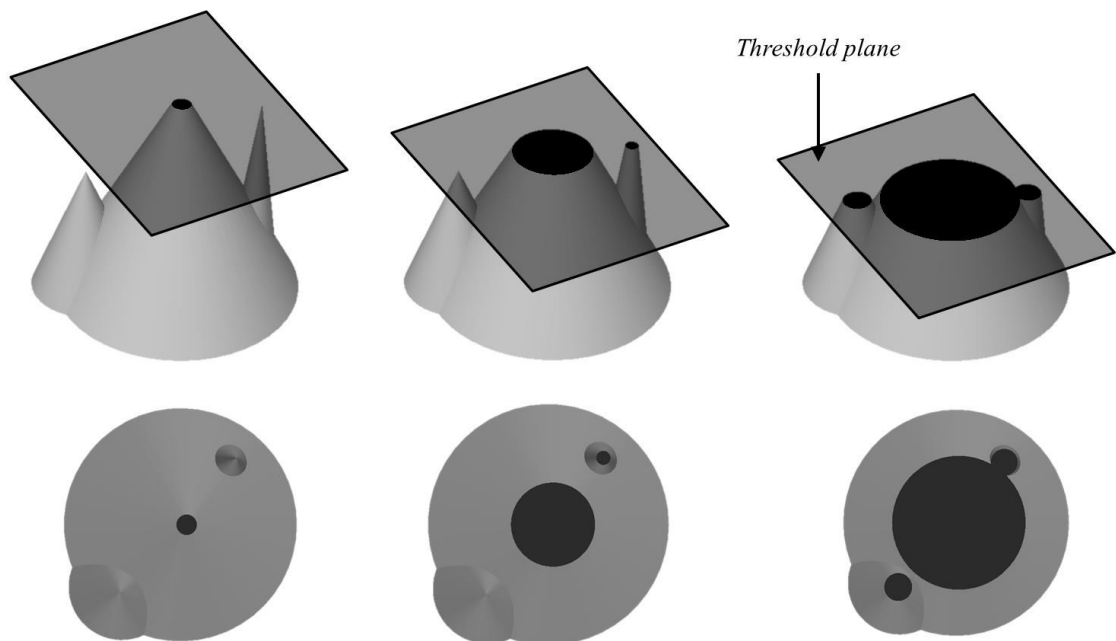- Total area: The total area of the particles in the image.

Figure 5.4 Blob analysis example with decreasing threshold plane

Figure 5.5 shows the effect of increasing threshold depth on the resulting binary image for the freshly dressed grooved wheel.
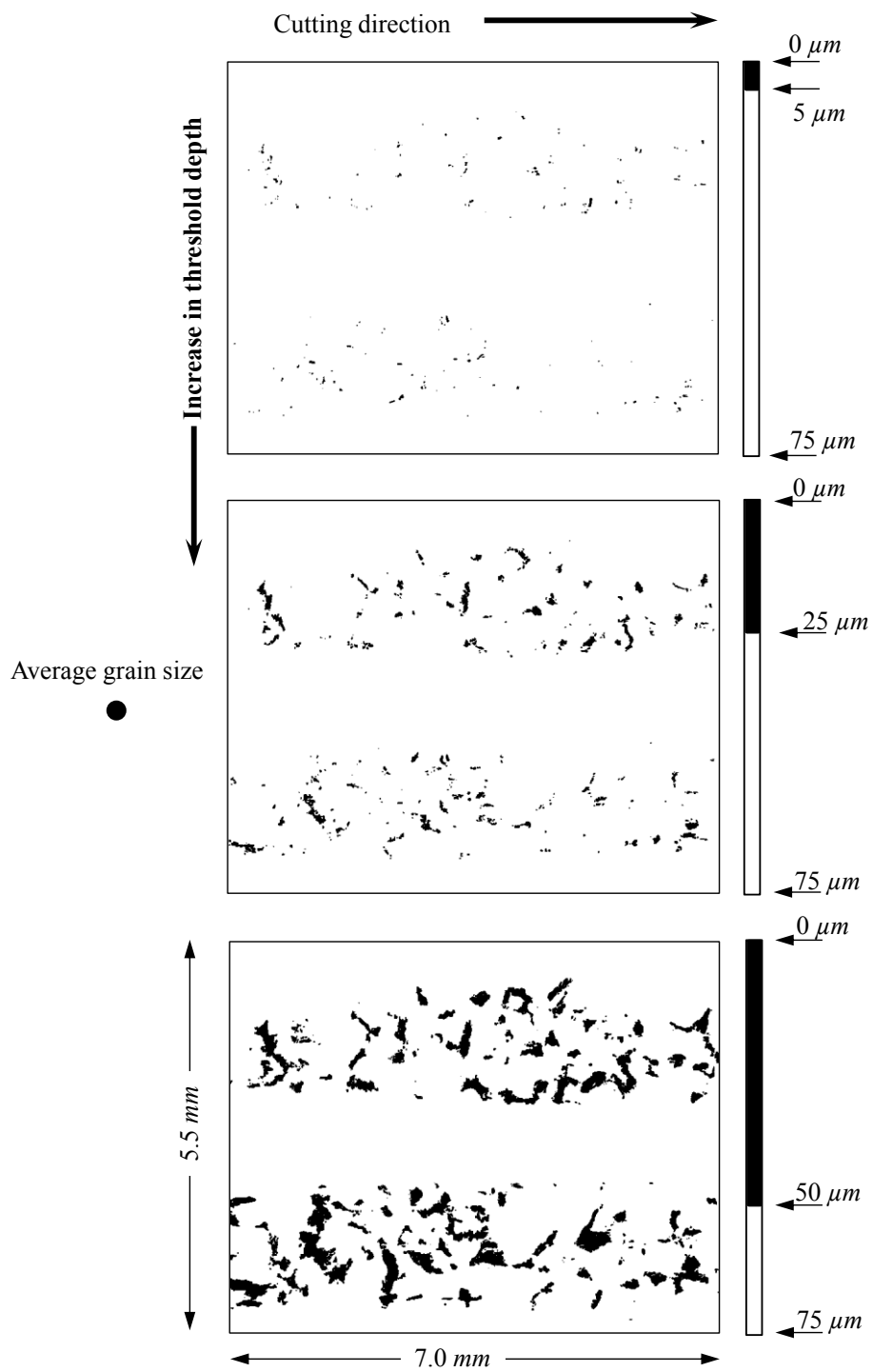
Figure 5.5 Thresholded scans at depths of 5, 25 and 50 *μm*

5.3.1 Filtering

Obtaining measurements from the chromatic sensor presents two major issues that that need to be corrected before the data can be used. First, noise from the sensor can form small peaks throughout the data which inherently has a large effect on the number of particles and average particle width. Secondly, as the wheel is used, debris such as workpiece chips can become clogged between the grains as shown in Section 4.3.2. Debris generally results in significant height differences in the measurement due to their shape. In order to address these issues, a series of filtering techniques were applied to the measurement data. A low-pass attenuating FFT filter was first used on the data to remove the peaks. This filter applies a linear attenuation to the data which is directly related the frequency. High frequencies are attenuated significantly while low frequencies see little to no effect. While this filter worked appreciably well, some erroneous measurements remained. A small particle filter would potentially remove the top of actual grains and therefore cannot be used. A custom filter was designed to remove all remaining erroneous measurements and is illustrated in Figure 5.6. The custom particle filter works by examining the edges of all particles under a set limit of area at each threshold height. If over 50% of the surrounding pixels of the examined particle result in a change of height over 200% of the particle's smallest dimension then the particle was considered to be unable to perform in the cutting operation and was removed from further analysis. For this study, any particle with an area less than 500 μm^2 was examined. For the example shown in Figure 5.6, the threshold height is at 100 μm and the minimum dimension of the particle is 1 pixel; therefore, 5 μm.
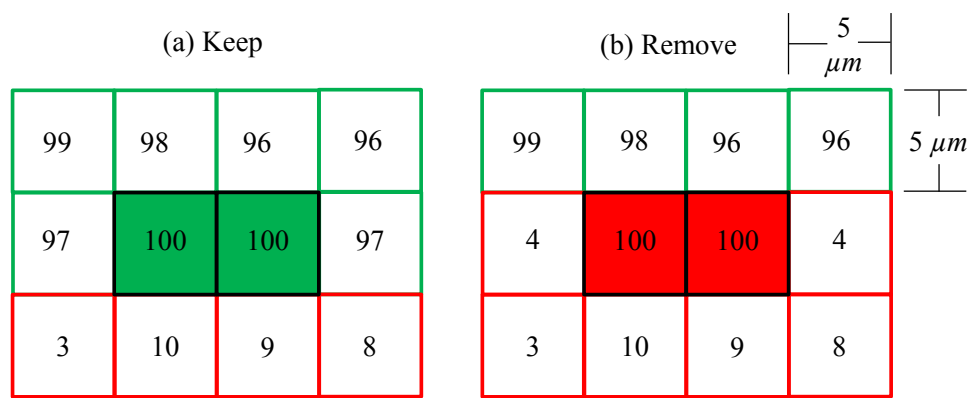
Figure 5.6 Custom filter example for (a) pass and (b) remove cases

Figure 5.6 (a) shows a particle that would have passed through the filter because 60% of its surrounding particles are within the 5 *μm* range. In Figure 5.6 (b) however, only 40% of the particles neighbours are within the limit and therefore due to its aspect ratio it is removed from further analysis. Figure 5.7 shows the effect of the two filters on the freshly dressed grooved wheel data at decreasing threshold levels.
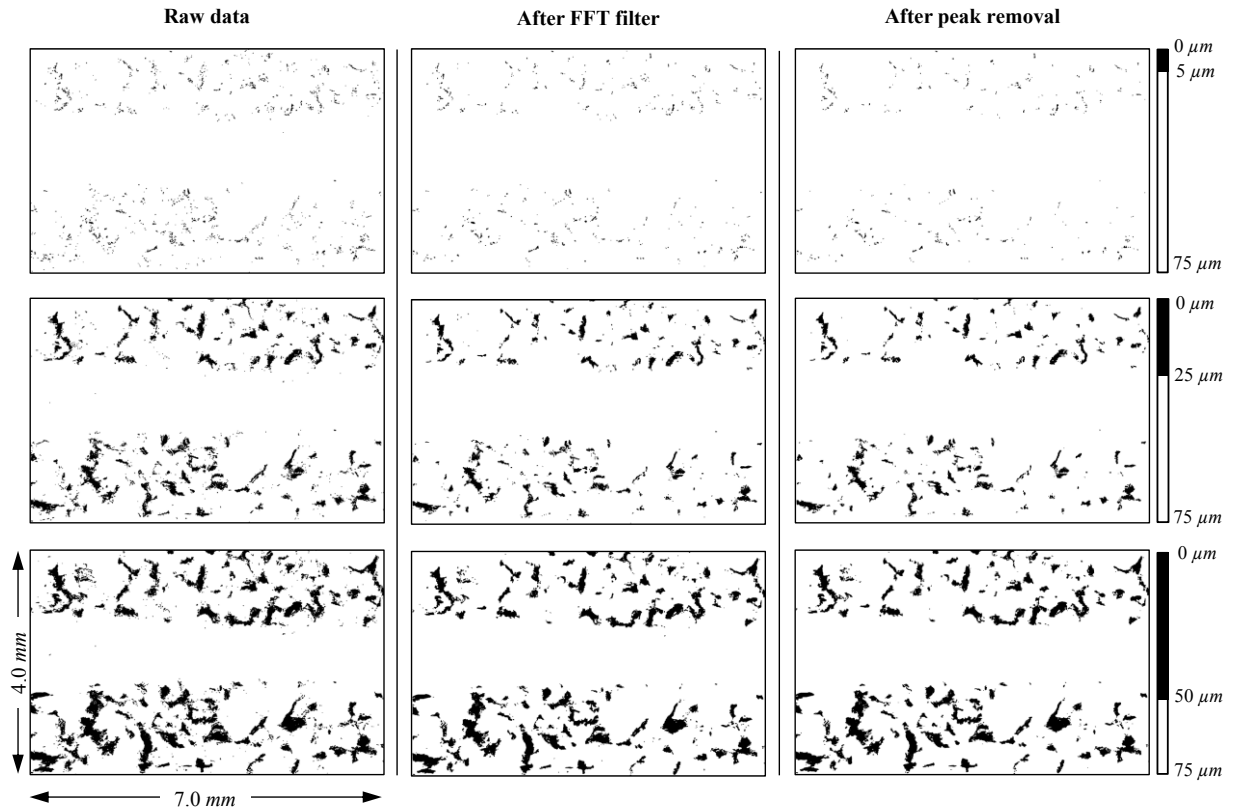
Figure 5.7 Filtering effect through decreasing threshold depth

It can be seen from Figure 5.7 that many of the small particles have been removed at all threshold depths. There are, however, some particles still remaining which is the benefit of the custom filter over a standard small particle filter. Figure 5.8 shows the filtering progression of one grain at a threshold depth of 40 *μm* and compares the results to a digital image of the grain.
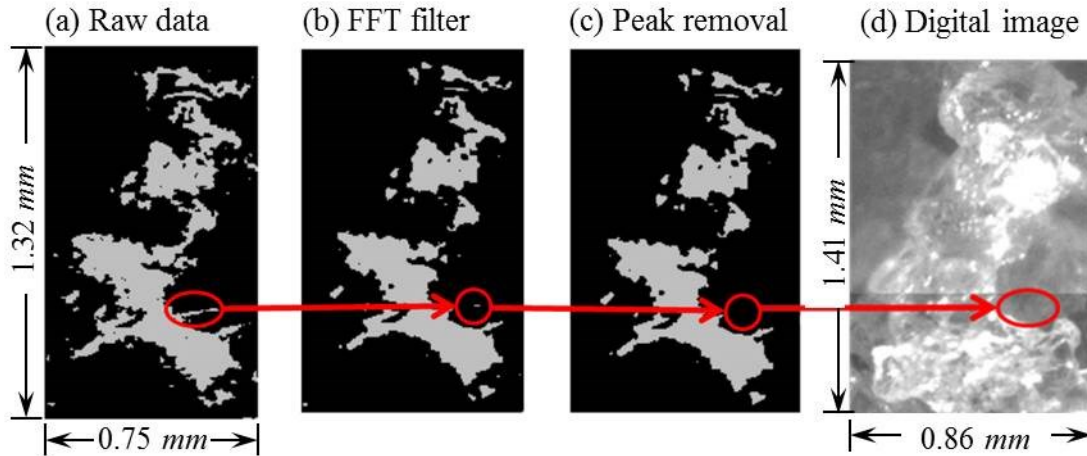
Figure 5.8 Filtering progression for (a) raw data, (b) FFT filter and (c) peak removal at a threshold depth of 40 μm with comparison to digital image

Based on Figure 5.8 it is clear that the removed area was probably not part of the grain but could have been wheel contaminate.

5.3.2 Height Referencing

In order to directly compare subsequent scans, it is crucial that the scans are referenced to the same baseline. Continuously removing and placing the wheel on the scanner resulted in some setup error. It is also important to note that due to the scans taking roughly seven hours each, full experiments can take months to complete and it is nearly impossible to ensure that the optical pen is not moved during that period.

A technique was developed in order to ensure that all the scans were referenced to the same height to account for the previously discussed issues. The method works by ensuring that the scan contains a portion of the wheel that had not been ground. This unground section of the scan was used as a reference surface. The scan is then processed in two separate portion: the unused or reference portion and the ground portion. Figure 5.9 depicts the reference portion for two scans taken at different periods during the experiment.
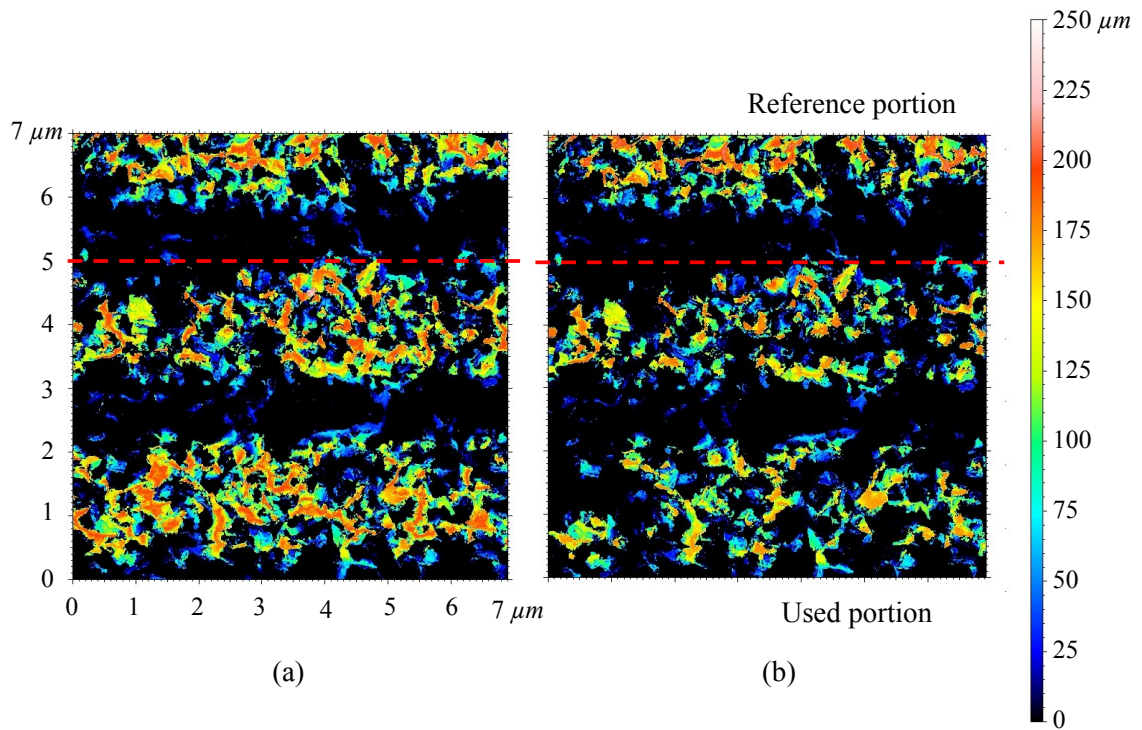
Figure 5.9 Reference section comparison for (a) fresh and (b) used wheel surfaces

In Figure 5.9 a dashed red line separates the two portions of the scan: above being the reference and below being the ground portion. Figure 5.9 (a) is a fresh grooved grinding wheel before any grinding had been performed and Figure 5.9 (b) is after 38100 mm^3 of workpiece material has been removed. The two reference portions are clearly very similar while notable change can be seen between the lower sections. To better demonstrate these differences, Figure 5.10 shows the reference and used sections of the scans for both the freshly dressed and used wheel at different threshold depths.
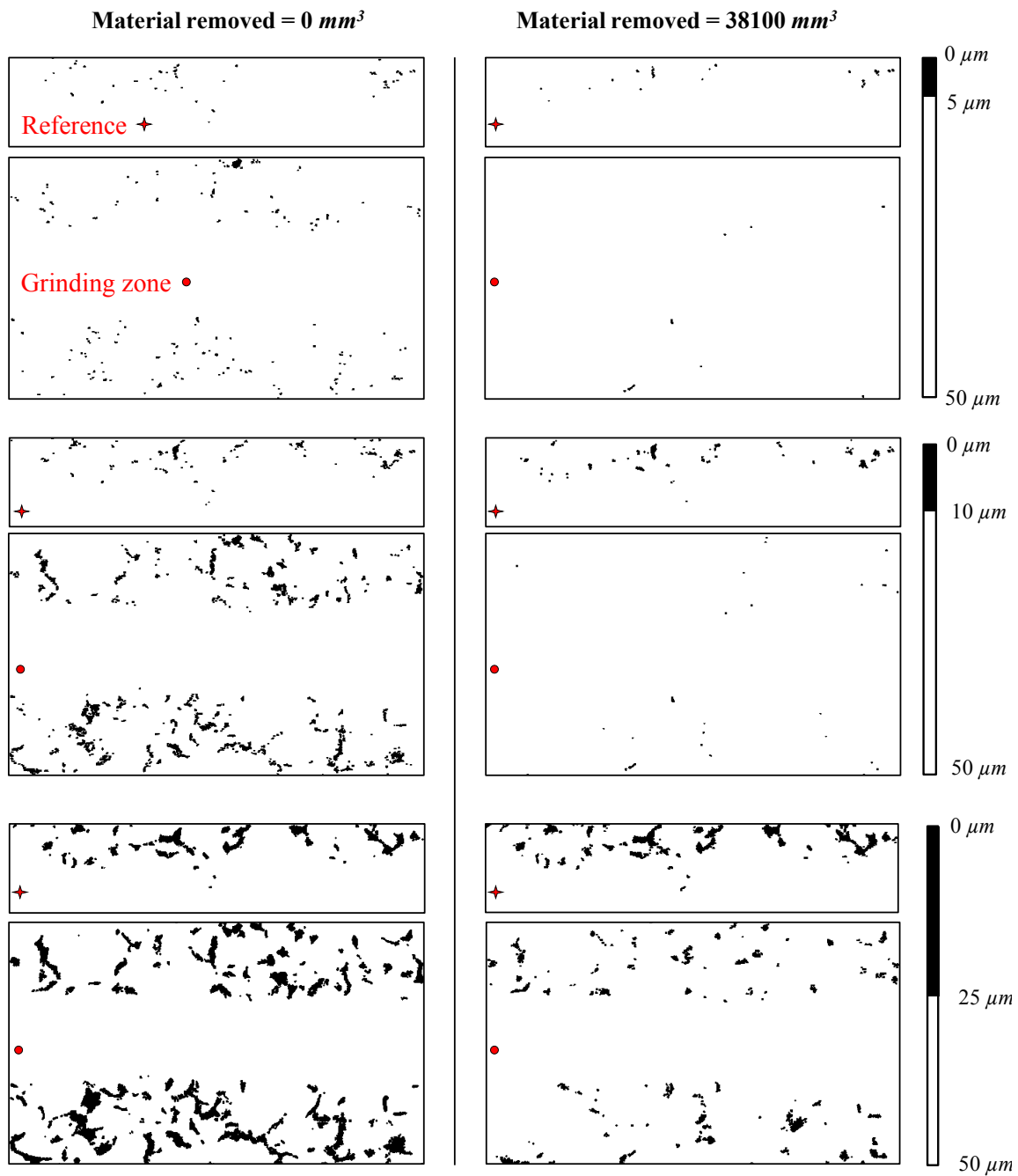
Figure 5.10 Referencing threshold plots

It can be seen throughout the threshold depths that the reference sections for the fresh and used wheel were more or less the same. By aligning the blob analysis results of the reference sections it ensures that all scans are being analyzed from the same starting

height. Significant differences can be seen in the grinding zone sections as a result of the wear of the grinding wheel. Abrasive wear has removed some grains from the wheel completely and attritious wear has lowered the surface of the wheel which is why there are practically no particles seen in the shallow depths of the used section. The small particles seen at a depth of 5 μm in the used wheel are likely wheel contaminate. This observation raises the question: What depth truly represents the surface of the wheel? Being able to determine where the surface of the wheel is located is critical for the analysis of grinding wheel wear. Although the filters removed much of the noise, some contaminate in the wheel cannot be filtered out due to its geometry. In order to try to differentiate the wheel surface from contaminate the rate of change of the total area was examined for the two grinding zone scans in Figure 5.10 and the results can be seen in Figure 5.11.
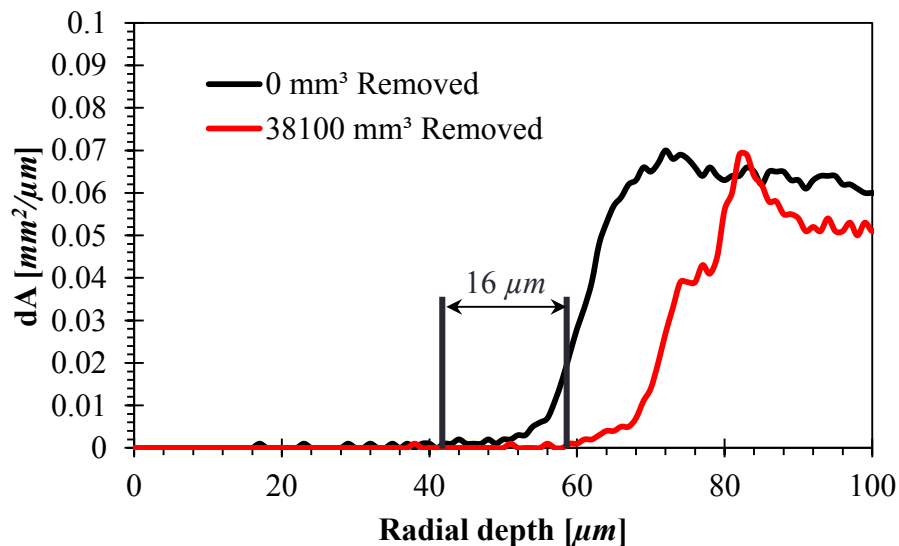
Figure 5.11 Rate of change of area as a function of threshold depth

A rate of change of 0 $mm^2/\mu m$ means that the particles at that depth are not getting wider as the radial depth increases, which is not realistic of a cutting edge and therefore can be disregarded. In order for a given height to truly represent the grinding wheel it cannot have a rate of change of zero. This observation leads to the conclusion that the height at which the surface of the wheel lies can be derived by finding the location at which the

rate of change becomes and remains a non- zero value. For the two scans shown in Figure 5.11, the surface of the wheel would be located at depths 42 and 58 μm for 0 and 38100 mm^3 of removed material respectively. The difference in the surface height indicates that the wheel has worn 16 μm. In order to compare results from the blob analysis consistently, the data must be shifted to ensure that all threshold planes begin at the surface of the wheel that is in contact with the workpiece for each scan.

5.4 Results

This section will present the results of the grinding experiments. Conventional grinding experiment measurements will be presented first. The blob analysis results will then be discussed for both non-grooved and grooved wheel measurements. A detailed analysis will then be performed to measure the effect of the grinding process on both wheels. Finally a direct comparison will be carried out to quantify the differences in wear between both wheels.

5.4.1 Conventional Measurements

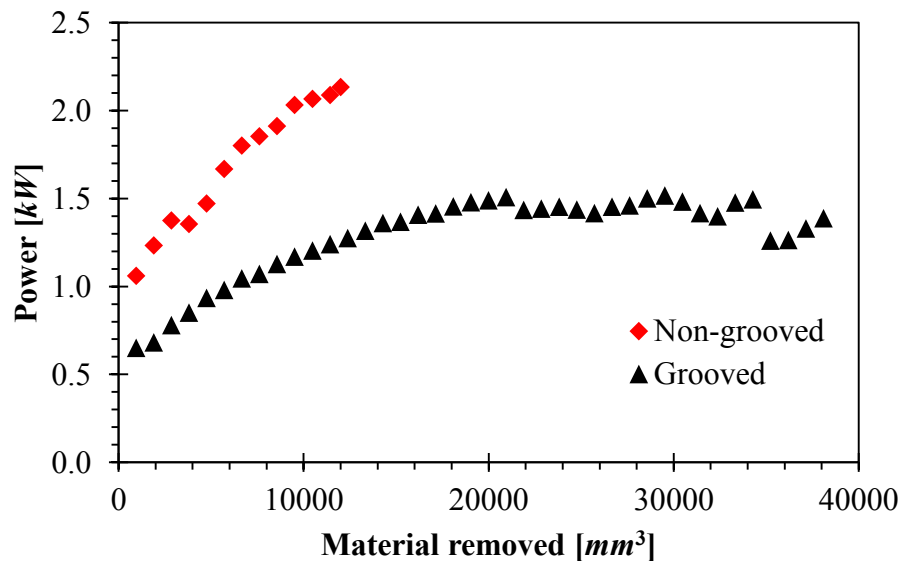Figure 5.12 shows the average spindle power consumed for both sets of experiments.

Figure 5.12 Consumed power for non-groove and grooved wheel experiments

When grinding with a non-grooved wheel the power consistently increases as more material is removed and the workpiece experienced burn at 12001 *mm*^{3} of removed material, at which point the experiment was stopped. During the experiments with the grooved wheel the power was consistently lower than with a non-grooved which agrees with literature [47, 49, 50]. The power seems to level off and at 21907 *mm*^{3} and it begins to fluctuate at 30480 *mm*^{3} of removed material. The forces are directly related to the power and surface topography as well. Figure 5.13 plots the normal and tangential forces for both the non-grooved and grooved grinding wheels.
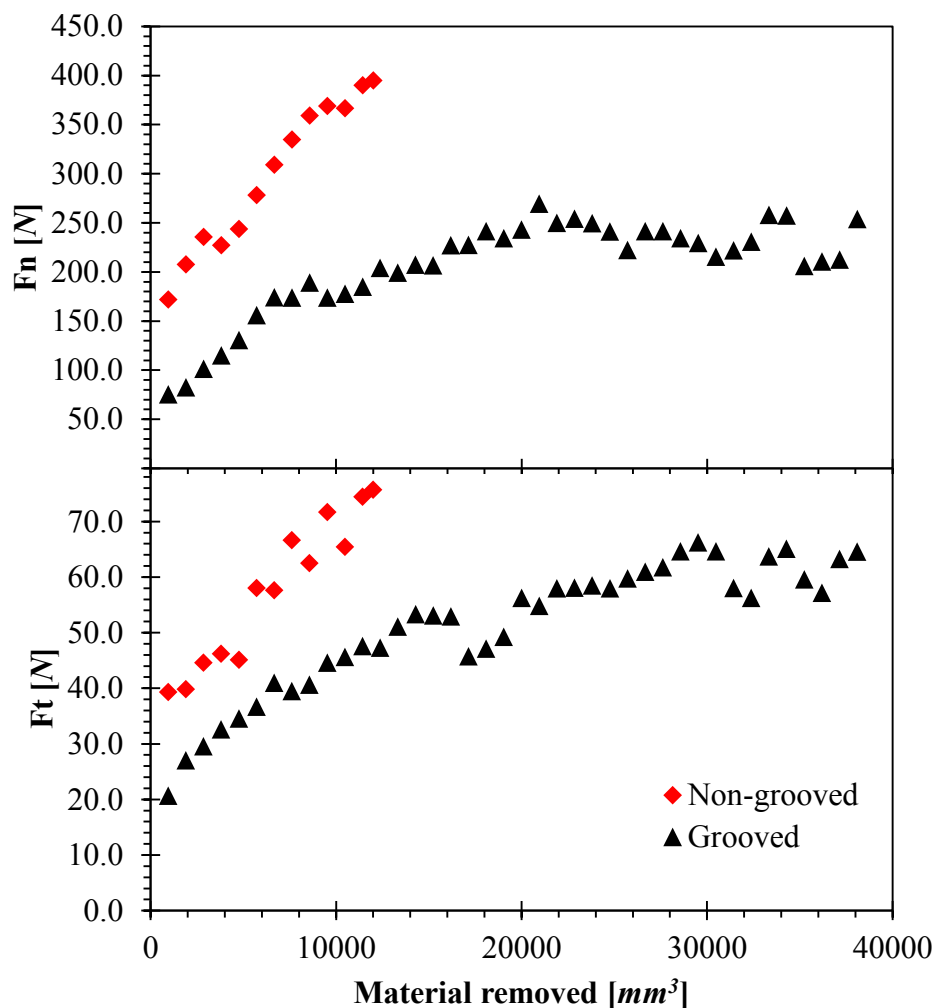

Figure 5.13 Normal and tangential forces for non-grooved and grooved wheel experiments

Both forces follow the same general trends as the power which is to be expected. The grooved grinding wheel is consistently lower than the non-grooved, and the fluctuations begin around 30480 mm^3 of removed material. The final conventional measure which was recorded was the workpiece surface roughness. The surface roughness is also directly correlated to the topography of the grinding wheel and is shown in Figure 5.14.
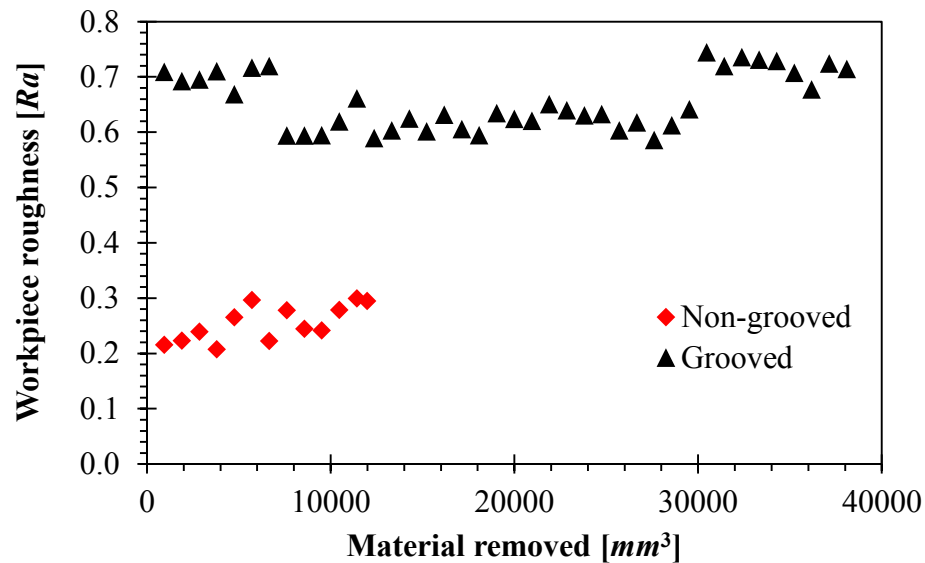
Figure 5.14 Surface roughness for non-grooved and grooved wheel experiments

The grooved wheel resulted in a consistently rougher surface but both wheels were below 1.6 μm which corresponds to an "average quality" surface finish [52]. The non-grooved surface roughness generally increases as more material is removed. The surface roughness for the grooved wheel roughness decreases from 0.7 to 0.6 μm at 6668 mm^3 of removed material and remains relatively constant until 29527 mm^3, after which it increases again.

5.4.2 Blob Analysis

The non-grooved wheel was examined first using blob analysis. The data was processed and aligned using the method previously discussed. A maximum depth of 50 μm into the

wheel was selected to be investigated. Figure 5.15 shows a comparison of the freshly dressed and worn wheels' resulting binary images for threshold depths of 5, 10 and 25 *μm.*

Material removed = 0 *mm³*   **Material removed = 11430 *mm³***
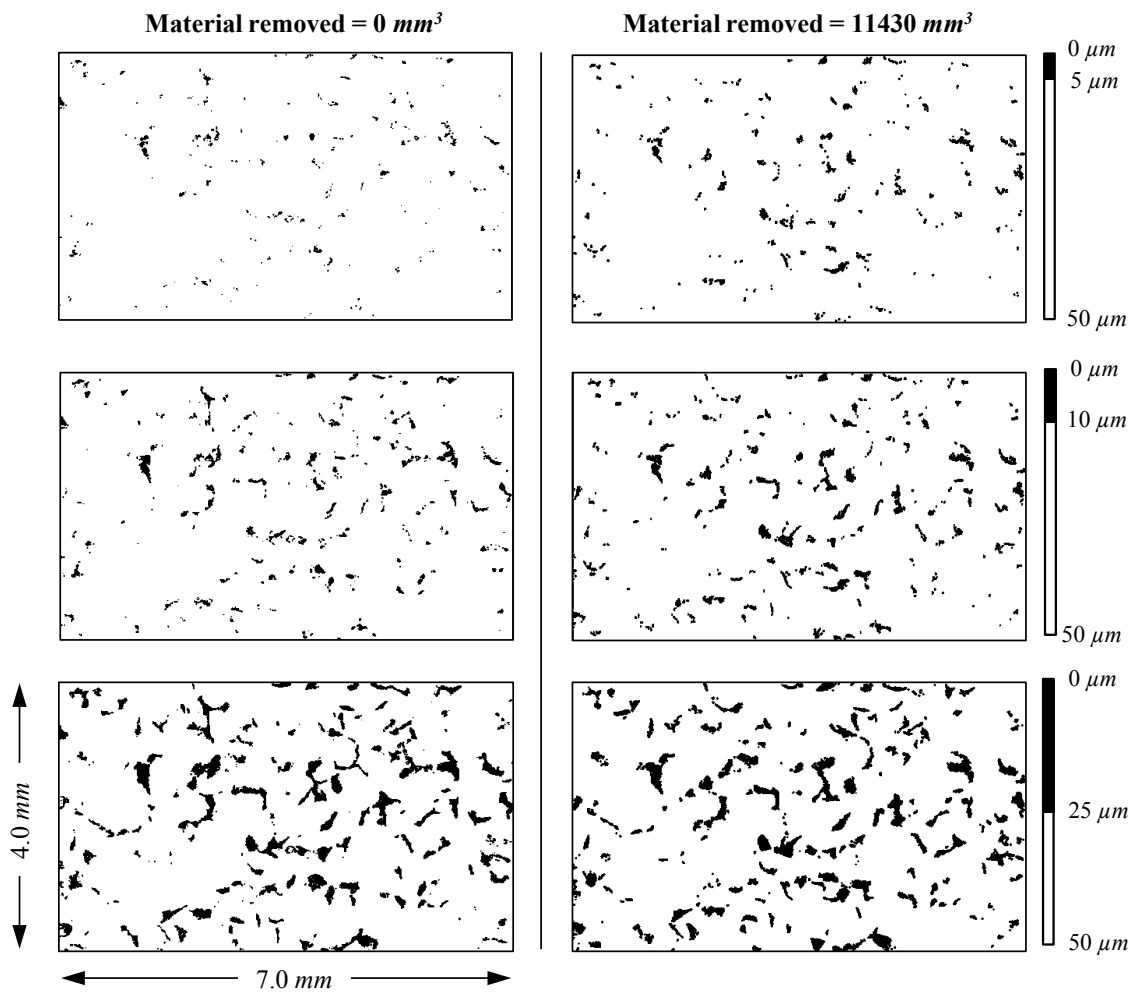
Figure 5.15 Non-grooved wheel topography with increasing threshold depth

A significant difference can be seen in the smaller depths. The particles appear to be larger for the worn wheel. Figure 5.16 shows the number of particles, particle width and total area as a function of depth for a non-grooved wheel throughout the experiments. This data will be analyzed further in later sections.
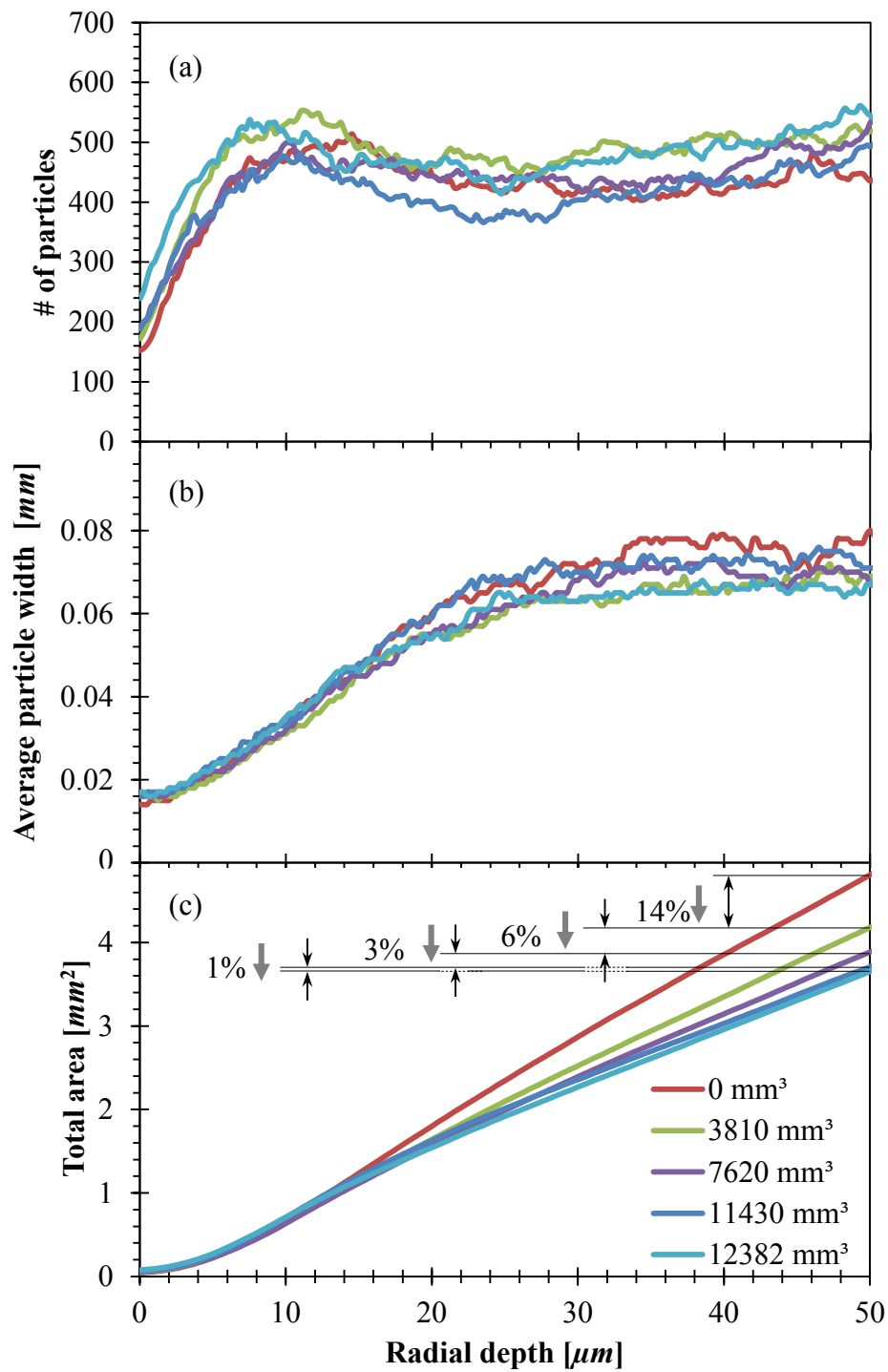
Figure 5.16 Non-grooved (a) number of particles, (b) particle width and (c) total area as a function of radial depth

All five scans in Figure 5.16 (a) can be seen to have the same general trend, which is to rise quickly and then fall slightly to a relatively steady state. The sharp rise at the beginning is due to the tips of cutting points being discovered at lower threshold depths. The peak is likely due to the fact that grains can have multiple cutting points and at deeper depths the cutting points that share a single grain amalgamate into their respective grains. By examining the difference throughout material removal it can be seen that the peaks are shifting to the left due to the wear of the individual cutting points.

It is difficult to distinguish large differences in the particle width shown in Figure 5.16 (b). It is clear however, that they follow a very similar trend. The width slowly increases until reaching an asymptote between 0.06 and 0.08 *mm*. Due to the sensor not being able to measure sharp angles, it is not expected that the entire grain diameter be measured. An asymptote between 0.06 and 0.08 *mm* is reasonable when considering the average grain diameter of the wheel is 0.220 *mm*.

Figure 5.16 (c) shows that the total area increased exponentially at low depths and then linearly throughout deeper depths. In the linearly increasing region, a fanning out trend can be seen with less and less area after each pass. The reduction in area is likely due to fracture wear in the wheel. An interesting characteristic of Figure 5.16 (c) is that in the deeper depths the difference between areas was decreasing as grinding progressed. At 50 *μm* into the wheel the reduction between successive scans decreased from 14% to 1% throughout the experiment. This higher initial wear agrees with literature [4].

The grooved wheel measurements were then subjected to the same analysis. Figure 5.17 shows the binary images from the freshly dressed and worn grooved wheel measurements at threshold depths of 5, 10 and 25 *μm*.

**Material removed = 0** *mm³*   **Material removed = 38100** *mm³*

Figure 5.17 Grooved wheel topography with increasing threshold depth
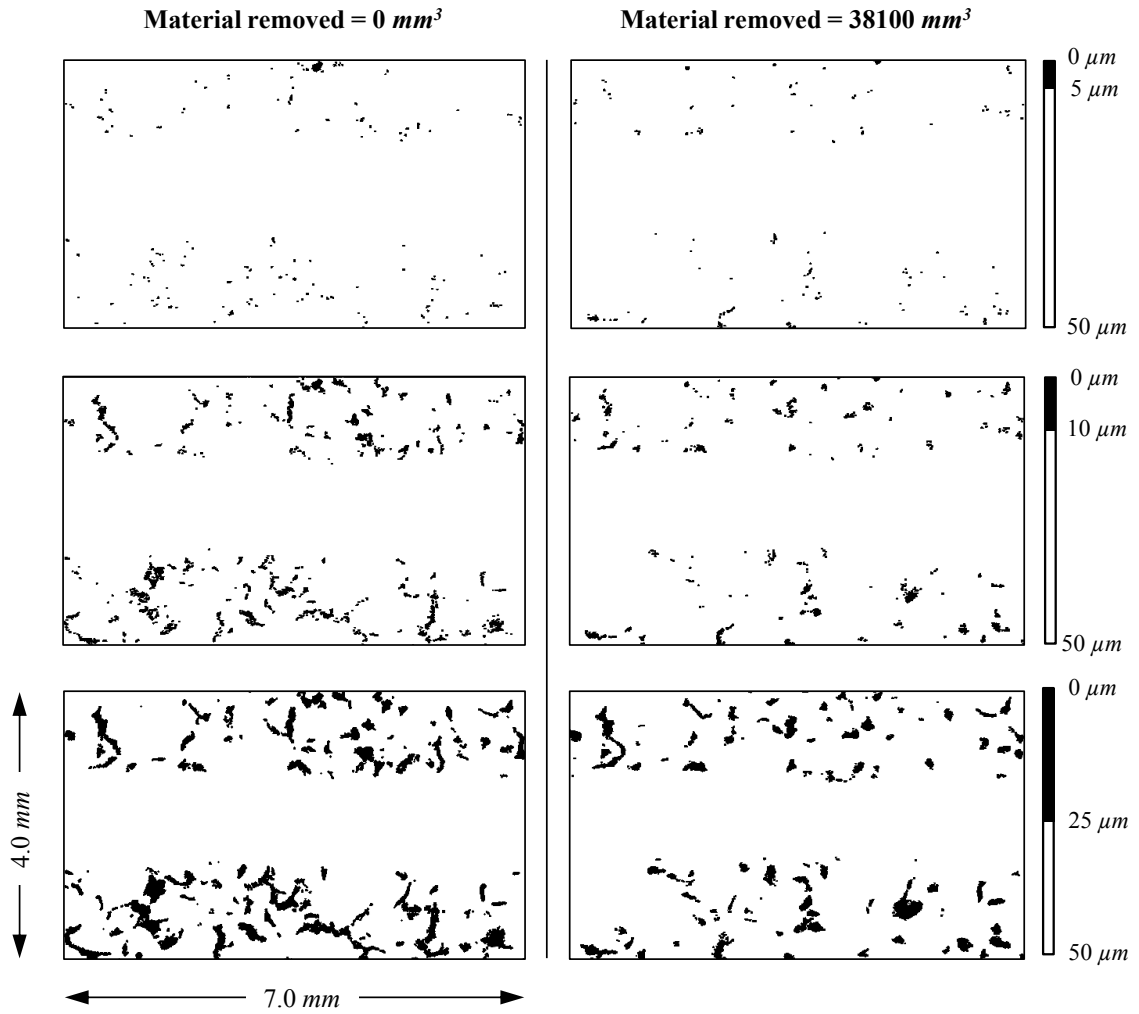
The groove is clearly visible throughout both sets of images. A noticeable decrease in the number of particles can be seen in the worn wheel at all threshold depths. Figure 5.18 shows the three extracted parameters as a function of threshold depth.
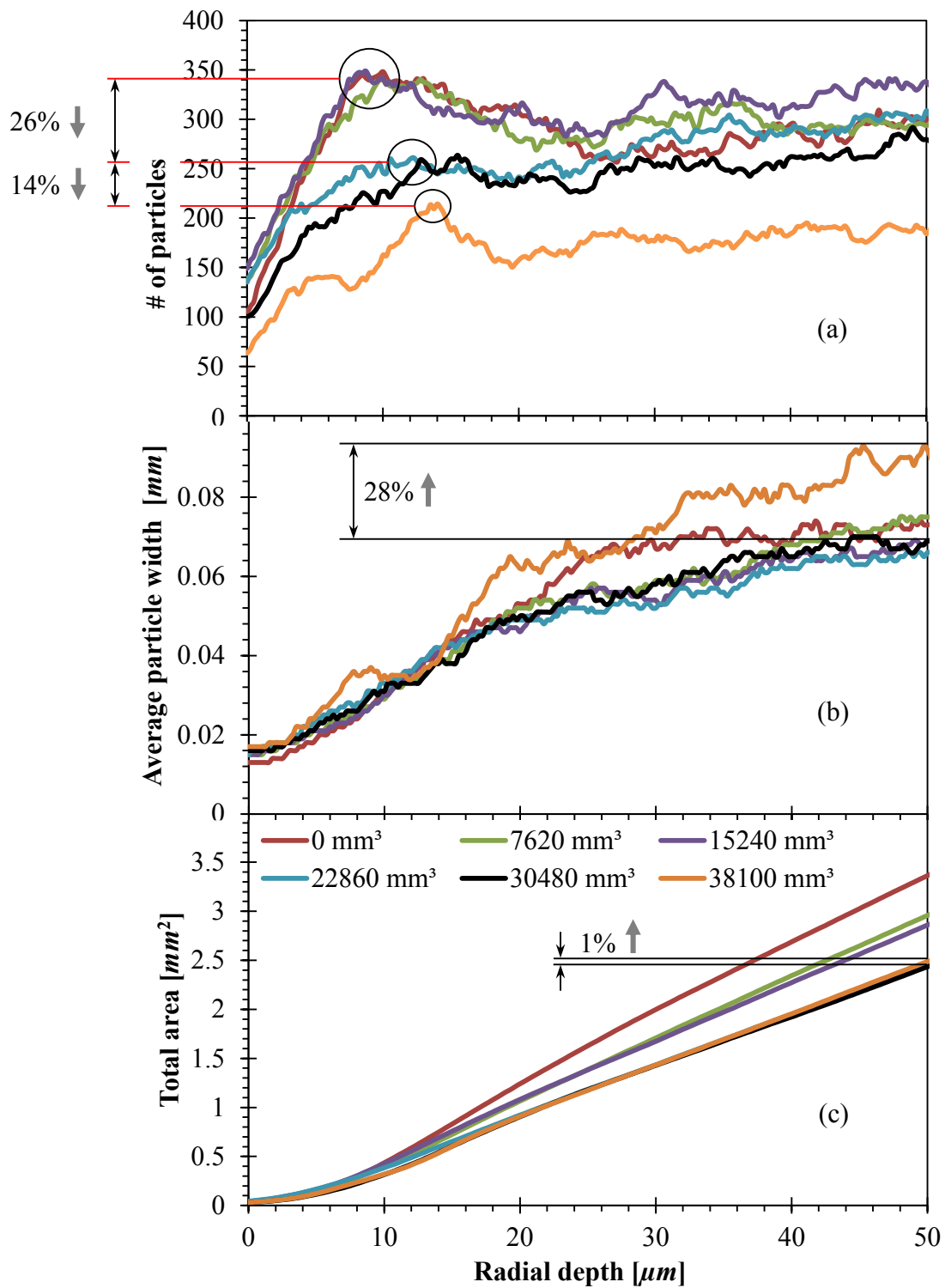
Figure 5.18 Grooved (a) number of particles, (b) particle width and (c) total area as a function of radial depth

The trend seen in the first three scans of Figure 5.18 (a) is similar to that seen in the corresponding non-grooved plot (Figure 5.16 (a)). The trend begins to degenerate at a removed volume of 22860 mm^3 when the number of particles at the peak decreased by 26% and then another 14% reduction seen at 38100 mm^3. The decrease seen in number of particles is likely due to one of two phenomenona. The first being cutting edges located on the same grain have amalgamated due to attritious wear. The second possibility is that accelerated fracture wear has occurred. Further investigation is required in order to determine which phenomenon is present.

The widths of particles also follow a similar trend to their non-grooved counterparts, leveling off between 0.06 and 0.08 mm except for the final scan. At 38100 mm^3 of workpiece material removed the width of particles increased 28 % from the previous scan, at a depth of 50 μm. This result is a significant increase compared to the changes seen throughout the experiment. It is still not possible to determine whether or not the wheel has undergone cutting edge amalgamation or accelerated fracture wear at this point.

Considering all three plots together is necessary for determining the leading wear mechanisms in the final scan. The combination of the significant decrease in number of particles with the increase in particle width suggests that the cutting edges could have amalgamated. This theory is further supported by the total area in Figure 5.18 (c), if further breakdown did occur then a reduction in area would have been seen, when in fact the area increased by 1% at a depth of 50 μm.

Thus far, the blob analysis has indicated that the grains of both wheels were behaving similarly in the early stages of material removal. Significant differences were seen as the grinding continued. In the later phase, the results showed the grooved wheel likely underwent massive fracture wear, whereas the non-grooved wheel did not.

5.4.3 Wheel Surface Analysis

Analyzing the data as a function of radial depth showed several major aspects such as the difference in areas and particle widths throughout the depths. Many of the differences however, were observed at deeper depths into the wheel. In the shallower depths the plots were generally indistinguishable, leading to no differences being easily seen. The fact that the differenced were seen at deeper depths indicates that the differences were due to fracture wear. In order to quantify the attritious wear of the grains it is necessary to examine the wheel at shallower depths. Comparing the top 5 μm of the wheel throughout the experiment allows for an in depth analysis of the attritious wear. Slices will be taken in increments of 1 μm for the first 5 μm of each scan. Figure 5.19 shows the number of particles at a function of workpiece material removed for the top 5 μm of the non-grooved wheel.

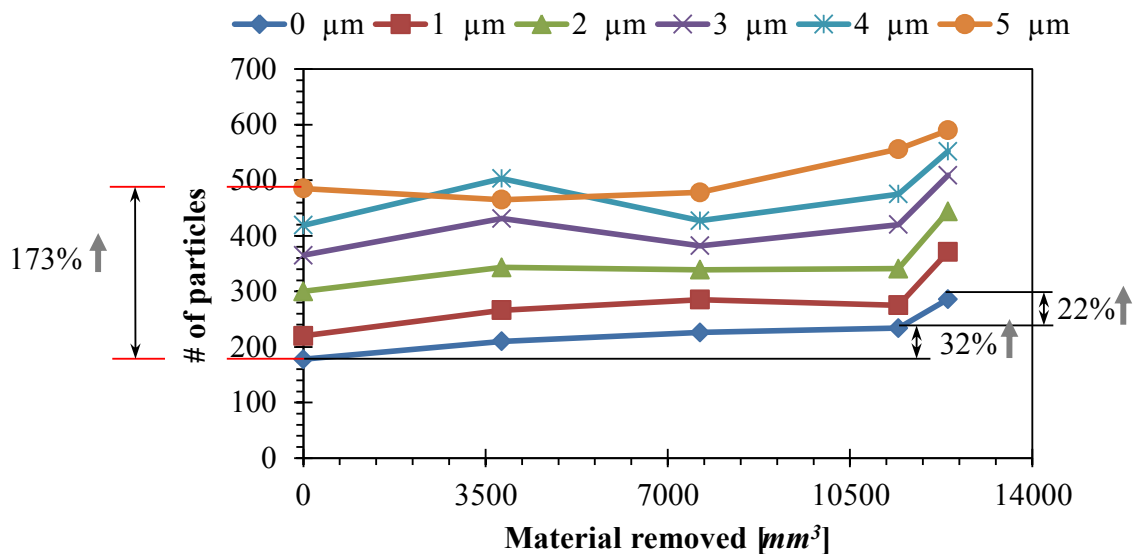Figure 5.19 Number of particles at non-grooved wheel surface

Generally, the number of particles rises as the depth into the wheel increases. Before the wheel was used, the amount of particles increased 173% between 0 and 5 μm. This increase is expected due to the fact that the grains and cutting edges are not all located at the same height. As the wheel is worn the number of particles also increases slightly and,

at the surface of the wheel, an increase of 32% is seen in the first 11430 mm^3 of removed material. The increase in particles as material was removed is also due to the grains being located at different depths. Attritious wear of the wheel lowers the surface and therefore the following scans are actually looking into a slightly deeper level. The final scan showed a 22% increase of particles over one pass, which is likely a result of increased wear rate from the workpiece burn. In order to provide further information of the wear of the wheel Figure 5.20 shows the particle width for the first 5 μm throughout the experiments.
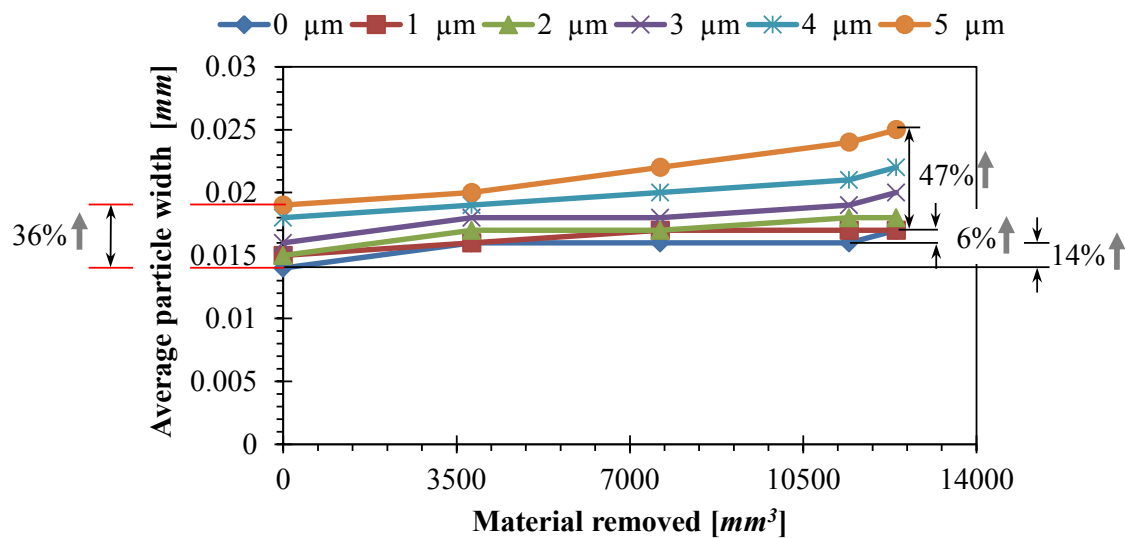

Figure 5.20 Particle width at non-grooved wheel surface

As depth into the wheel increases, more of the cutting edge area is being exposed, which can explain why Figure 5.20 shows a consistent increase throughout the depths. The same reasoning can explain why the difference seen between the width at the surface and a depth of 5 μm increased from 36% to 47% throughout the experiments. At the surface of the wheel the particles show a 14% increase in the first 11430 mm^3 of removed material with a 6% increase in the final 986 mm^3. The higher increase in the last pass is again, likely a result of the workpiece burn. The total area for the top 5 μm is shown in Figure 5.21.
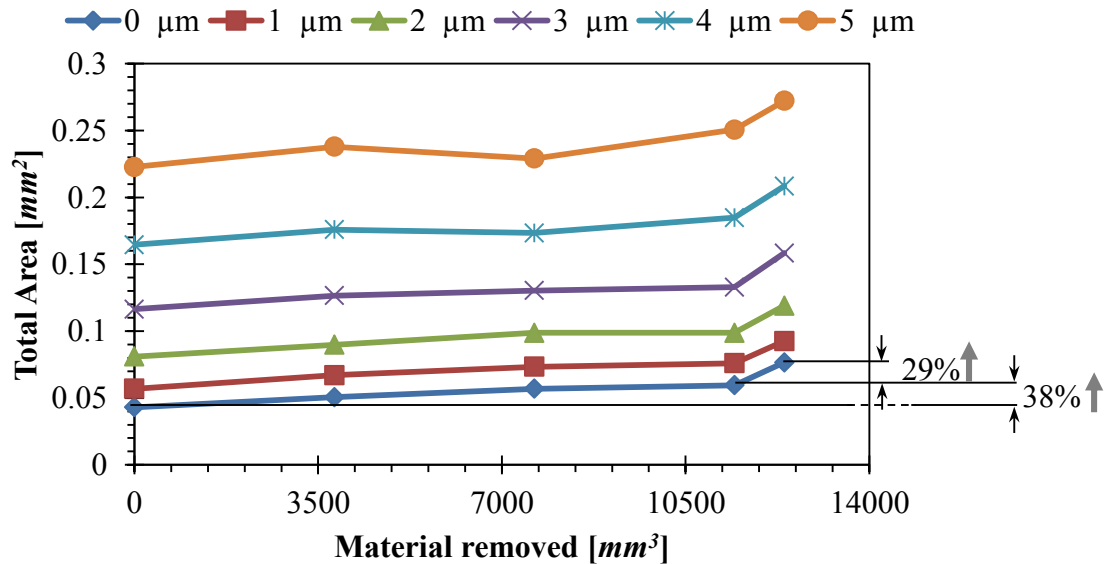
Figure 5.21 Total area at non-grooved wheel surface

The area throughout the top 5 μm of thewheel follows the same increasing trends as the previous two parameters. The final scan once again had a significant shift as a result of the workpiece burn. Before the burn occurred the area at the surface had increased by 38% over 11430 mm^3 removed and the final 986 resulted in a 29% increase.

By analyzing deeper depths it is possible to see the effect from fracture wear. As previously mentioned, the total area seemed to be clearly depicting fracture wear and therefore is the sole parameter analyzed for deeper depths. Four more slices were taken at depths of 10, 15, 25 and 50 μm. The resulting data can be seen in Figure 5.22 along with the measure at a depth of 5 μm for reference.
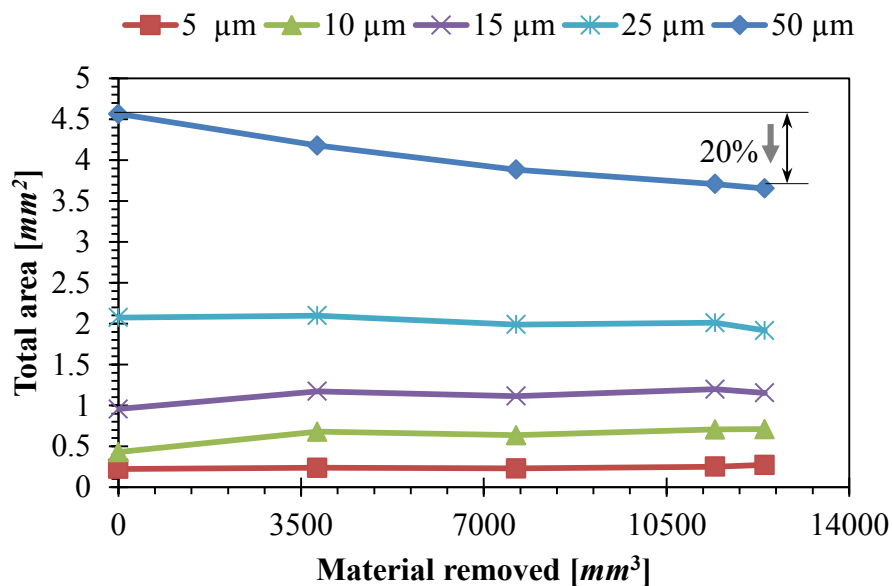
Figure 5.22 Total area of non-grooved wheel

Looking at the total area seen throughout a wider range of depths shows an interesting trait. As seen in Figure 5.21 and with the top 15 μm in Figure 5.22, the total area increases as the wheel wears. At 25 μm it can be seen that the active area stays relatively constant, with even a small decrease throughout the grinding process. At 50 μm there is a significant declining trend seen. The 20% decrease during experimentation indicates that the wheel is fracturing, whether it be grain or bond fracture is impossible to determine from blob analysis only. Figure 5.23 shows an example of the different wear mechanisms measured at different depths into the wheel with a comparison to a digital image.
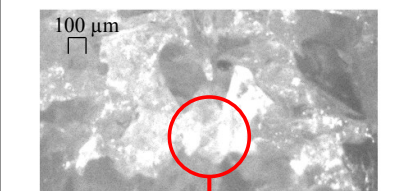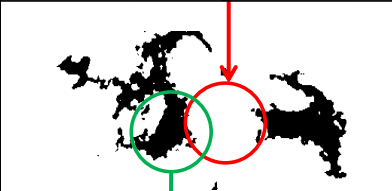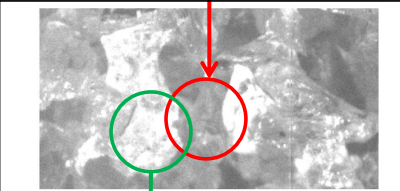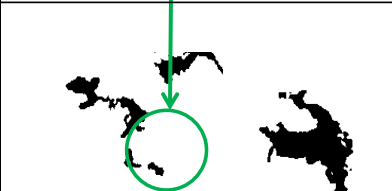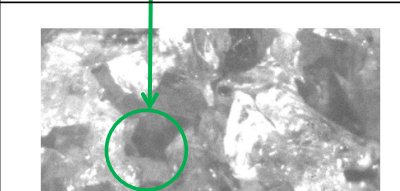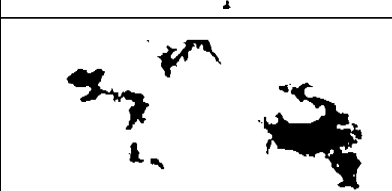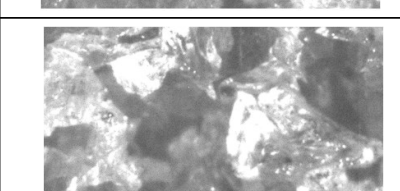
Removed material	5 μm	50 μm	Digital image
0 mm^3			
3810 mm^3			
7620 mm^3			
11430 mm^3			

Figure 5.23 Wheel wear mechanisms throughout depths

The two depths being examined are 5 and 50 μm. By looking at the change in the grain at a depth of 5 μm it is clear that as the wheel wears, its cutting edges become larger. This confirms the notion that the increase seen in the parameters is from attritious wear. It should be noted that this type of wear is very difficult to see or quantify from the optical image. At a depth of 50 μm bond and grain fracture can be observed. The red and green circles show examples of the fracture wear that occurred. The digital image confirms that grain or bond fracture has occurred.

As with the non-grooved wheel, a detailed analysis of the top 5 μm will be performed on the grooved grinding wheel measurements in order to better quantify the wear.
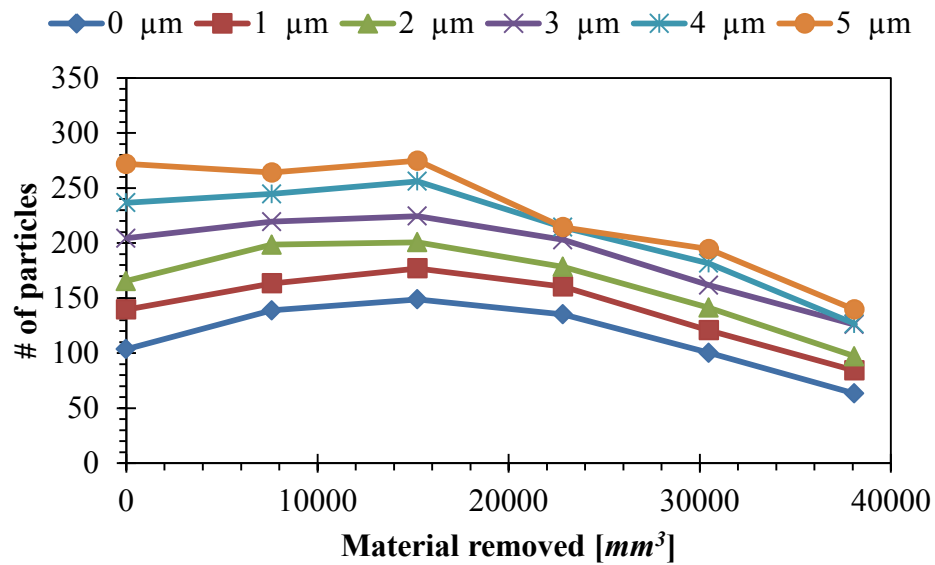
Figure 5.24 Number of particles at grooved wheel surface

The first thing to note in Figure 5.24 is the initial reduction in particles when compared with non-grooved data, the reason being the groove itself. Before any workpiece material was removed the grooved wheel had 103 particles at the surface and 272 at a depth of 5 μm. The non-grooved wheel data, previously shown in Figure 5.19, contained 178 and 485 particles at the same depths, respectively. Although a groove factor of 50% was used, the scan contained one groove; therefore, approximately 1/3 of the scan is simply a groove or nothing. The 1/3 missing from the scan directly correlates to the 42% and 44% decrease in number of particles seen at 0 and 5 μm, respectively. During the early stages of the experiment the number of particles followed very similar trends to the non-grooved wheel. After 15240 mm^3 of removed material the number of particles consistently decrease, which suggests either cutting edge amalgamation or accelerated fracture wear is occurring.
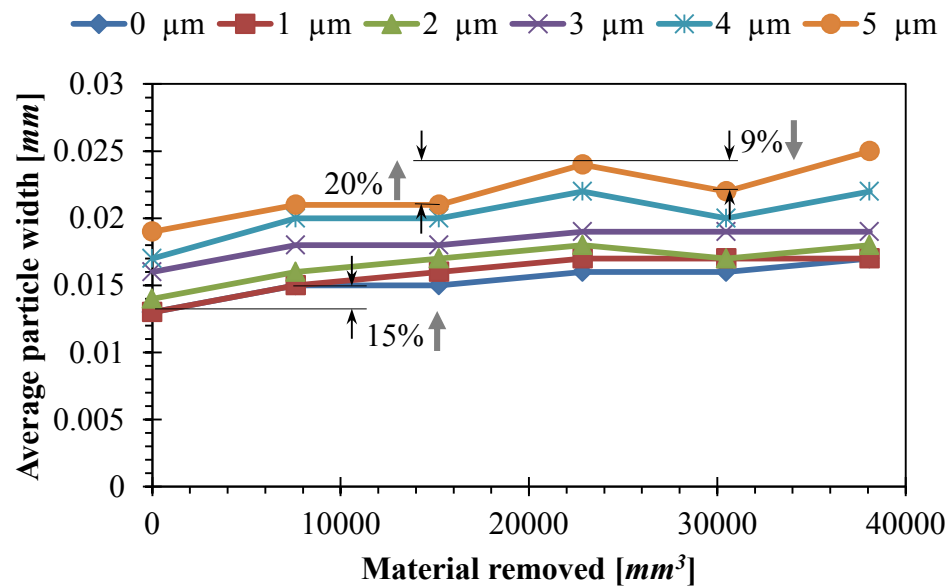
Figure 5.25 Particle width at grooved wheel surface

Figure 5.25 shows a similar increasing trend seen in its non-grooved counterpart shown in Figure 5.20. Over the first 7620 mm^3 of removed material, the grooved wheel's cutting edges at the surface increased by 15%. This value is appreciably close to the 14% increase seen in the non-grooved wheel after the same removed volume. The agreement of size increase suggests the grains are initially undergoing the same amount of attritious wear. Recalling that Figure 5.24 showed a significant drop in number of particles at 22860 mm^3 of removed material, it is interesting to note that the width of particles increased by 20% at the same point, which indicates that the cutting edges may have amalgamated from attritious wear. The next 7620 mm^3 however, resulted in a 9% decrease in particle width, implying that fracture wear occurred.
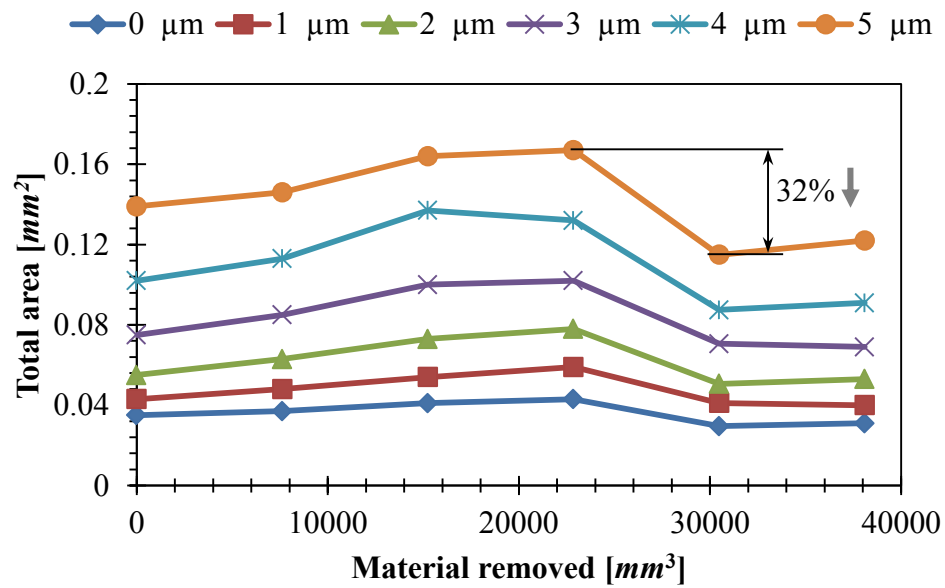
Figure 5.26 Total area at grooved wheel surface

The initial total area at a depth of 5 μm seen in Figure 5.26 is equal to 0.139 mm^2 while the non-grooved had an initial area of 0.222 mm^2. This 37% reduction is once again, likely a result of the groove. An interesting aspect of Figure 5.26 is the 32% decrease in area seen at 30480 mm^3 of removed material. The fact that a drop of this magnitude is seen throughout the top 5 μm of the grinding wheel strongly supports the hypothesis that fracture wear did occur at this point. Figure 5.21 also further supports the fact that although Figure 5.24 showed a decrease in particle numbers at 22860 mm^3 of removed material, it is was likely due to attritious wear rather than fracture since the area continued to increase during that period.
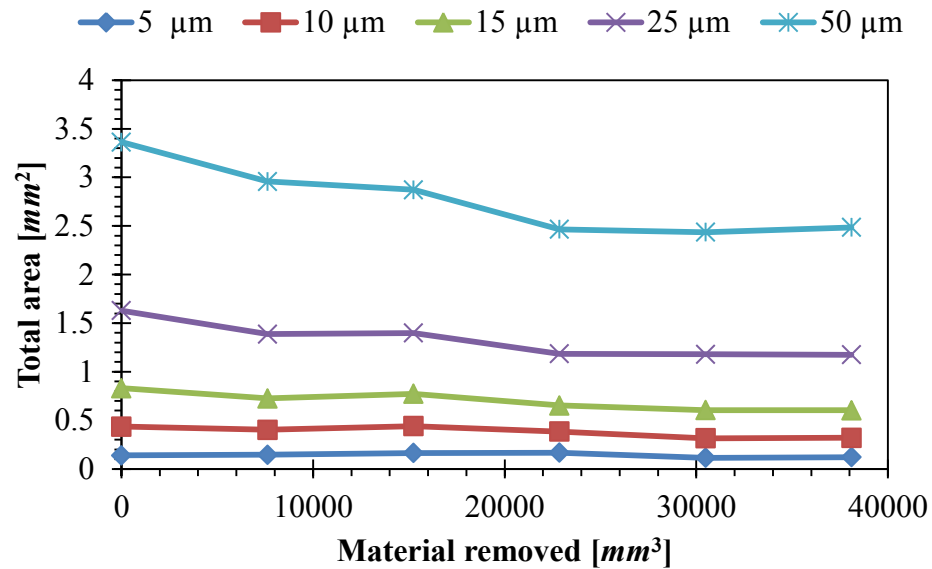
Figure 5.27 Total area of grooved wheel

Figure 5.27 shows that losses in the total area can be seen at lower depths into the wheel. The non-grooved wheel data only exhibited a negative slope after a depth of 15 *μm* whereas the grooved wheel data in Figure 5.27 shows negative slopes beginning at 10 *μm*. The negative slope could simply be an added effect of scanning a groove or it could indicate that grooved grinding wheels have a higher possibility of fracture wear. The effect of accelerated fracture wear on the blob analysis can be seen by comparing the same area for a fresh and used grinding wheel. Figure 5.28 shows a 2.75 × 2.75 *mm* patch at depths of 5 and 50 *μm*. The depths are compared for a fresh wheel and after the total removal of 38100 *mm*³ of workpiece stock. A digital image is also included to verify that the grain removals did occur.
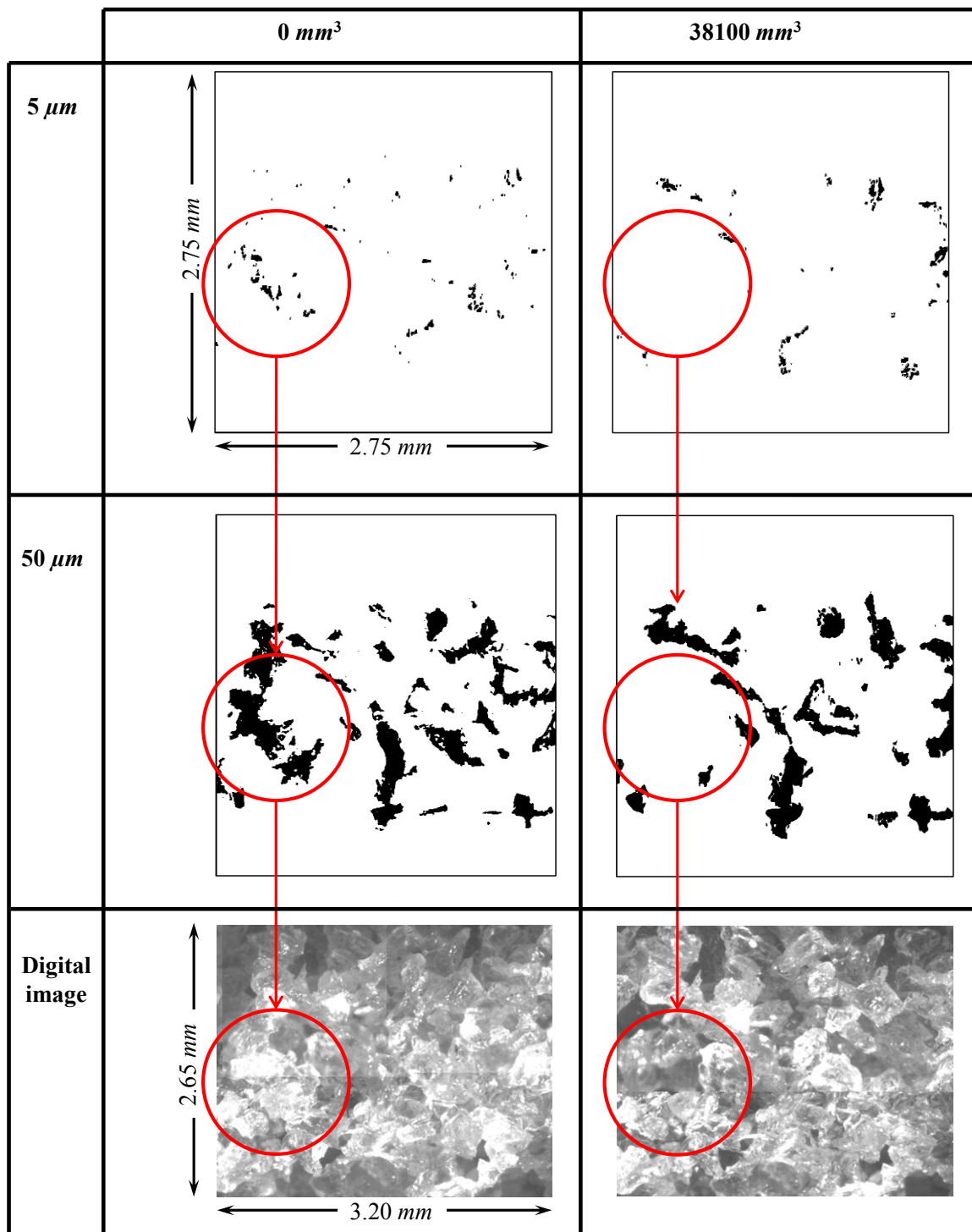
Figure 5.28 Blob analysis of massive fracture wear

The red circles in Figure 5.28 point out a section where significant change can be seen at both depths. By visually comparing the results at a depth of 5 μm it can be seen that the fresh wheel contained noticeably more cutting edges throughout. Many of the fresh cutting edges at 5 μm were very small in comparison to the worn wheel. At a depth of 50 μm a similar effect can be seen. There are very few small cutting edges remaining in the used wheel.

In general, the surface analysis has further proven the notion that the wheels were behaving similarly in the early stages of grinding. A significant increase in all three extracted parameters was seen in the final scan of the non-grooved wheel, which is indicative of workpiece burn. In the final scans of the grooved wheel, the top 5 μm showed a significant decrease in number of particles and total area which was likely due to accelerated fracture wear.

5.4.4 Comparison

A comparison using more conventional grinding parameters, all derived from the measured data, will now be performed. The parameters being compared are the radial and volumetric wear of the wheels, cutting edge spacing, and uncut chip thickness. As previously mentioned in Section 5.3.2, measuring the difference in surface heights for the reference and ground portions allows for the observation of radial wheel wear. Figure 5.29 depicts the amount of height reduction measured from the top of the wheel surface.
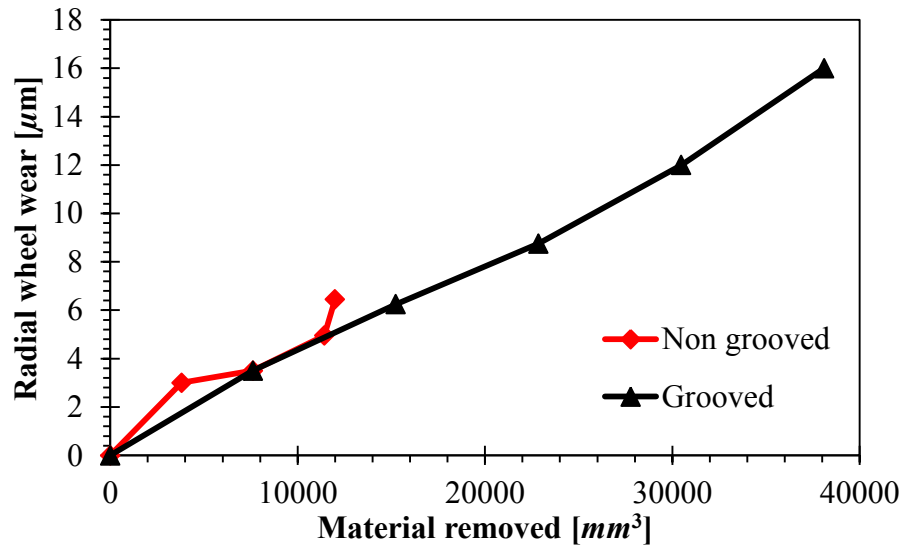
Figure 5.29 Radial wear comparison of non-grooved and grooved wheel

The two wheels were wearing at relatively similar rates before the non-grooved wheel was subject to workpiece burn. The similar height reductions further imply the wheels were wearing at comparable rates.

By performing a summation of the area measurements extracted from blob analysis it is possible to calculate the volume of the grinding wheel surface. Combining a volume measurement with the radial wear of the grinding wheel allows for a further comparison. For example, if the wheel was measured to have been reduced by 4 μm throughout the grinding, then the volume contained in the previous measurement's top 4 μm can be assumed to have been worn away. In order to ensure the volumetric wear is representative of the entire wheel circumference, a factor must be applied based on the ratio of scan area to grinding wheel surface area. Figure 5.30 was generated by calculating the volume removed from the entire wheel for all scans.
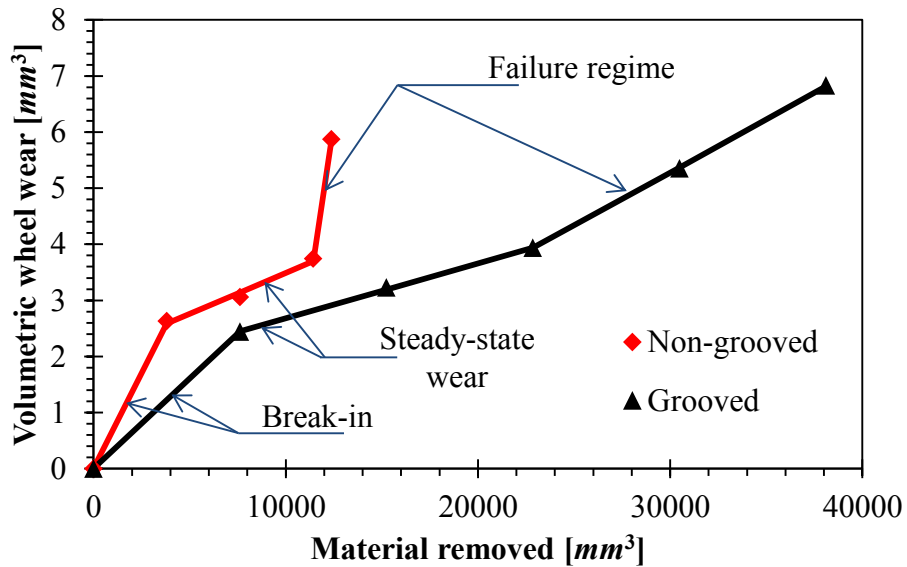
Figure 5.30 Volumetric wear comparison of non-grooved and grooved wheel

Figure 5.30 clearly shows that the grooved wheel performed better than the non-grooved wheel. Both curves show a similar trend to general tool wear [53]. The three regions of tool wear are the break-in period, steady state wear region, and the failure region, which are characterized by changes in the slope and highlighted in Figure 5.30 [53]. A common performance index known as the grinding ratio (G-ratio) can be derived from the information in Figure 5.30. The G-ratio is the volume of material removed per unit volume of wheel wear. During the steady-state wear regimes it is appropriate to calculate the G-ratio based on the slope of Figure 5.30 [4]. Table 5.1 contains the four calculated G-ratios. During the steady state regime the grooved grinding wheel was performing 50% better than the non-grooved wheel. This observation makes sense seeing as throughout the analysis and comparison the grains of both wheels were wearing similarly, and the grooved grinding wheel only has 50% of the volume of grains performing the cutting. During the failure regimes the non-grooved and grooved grinding wheels decreased 93 and 48% respectively.

Table 5.1 G -ratios for non-grooved and grooved grinding wheels

	Steady-state region	Failure region
Grooved	10215	5265
Non-grooved	6849	447

Typically, reported G-ratios in the literature are much smaller than the values found in this study. G-ratios of 1.5-5 have been reported when grinding tungsten carbide with a diamond wheel [54, 55]. When grinding with an aluminum oxide wheel, as in this study, G-ratios of 6.5-20 were reported when used on hardened steel [56], and 100 when used on boron steel [57]. The reason for the lower G-ratios is that in the past researches have calculated it by measuring the radial wear and then assumed that the entire volume encompassed in that depth has been removed. This approach means that the porous volume of the wheel was included in the wear of the grinding wheel, whereas this research is only measuring the loss of actual grain material. If the same method was applied to this research as the others, then the G-ratio would be roughly 160 and 61 for the steady state wear regimes of the grooved and non-grooved wheels, respectively.

Using the extracted measures of number of particles and particle width, the cutting edge spacing can be calculated. Assuming that at the surface of the wheel the measured particles are the cutting edges then the cutting edge density C can be calculated using Equation (5.1).

$$C = \frac{\# \: of \: particles}{Scan \: Width \: \times Scan \: Length} \qquad (5.1)$$

By considering an area with only one cutting edge, the width would be equal to the width of the cutting edge or particle b_p, and the length would be equal to the cutting edge spacing L [4].

$$C = \frac{1}{Lb_p}$$
$$(5.2)$$

With the cutting edge density and width known, Equation (5.2) can rearranged to solve for the spacing, as in the following [4]:

$$L = \frac{1}{Cb_p}$$
$$(5.3)$$

Figure 5.31 shows the cutting edge spacing for both non-grooved and grooved grinding wheels. There are two plots for the grooved wheel, one looking only at the non-grooved area of the wheel and the second includes the groove. In order to compensate for the groove in the results, a factor of 2/3 was applied to the grooved wheel data since 1/3 of the scan contained the groove. Since 50% of the wheel surface had been grooved, the average cutting edge spacing would double. The grooved wheel's non-grooved portion's average spacing was then doubled in order to calculate the average cutting edge spacing with the groove incorporated. The results shown are for a depth of 1 μm into the wheel surface, assuming that all points at this depth are acting in the cutting process.
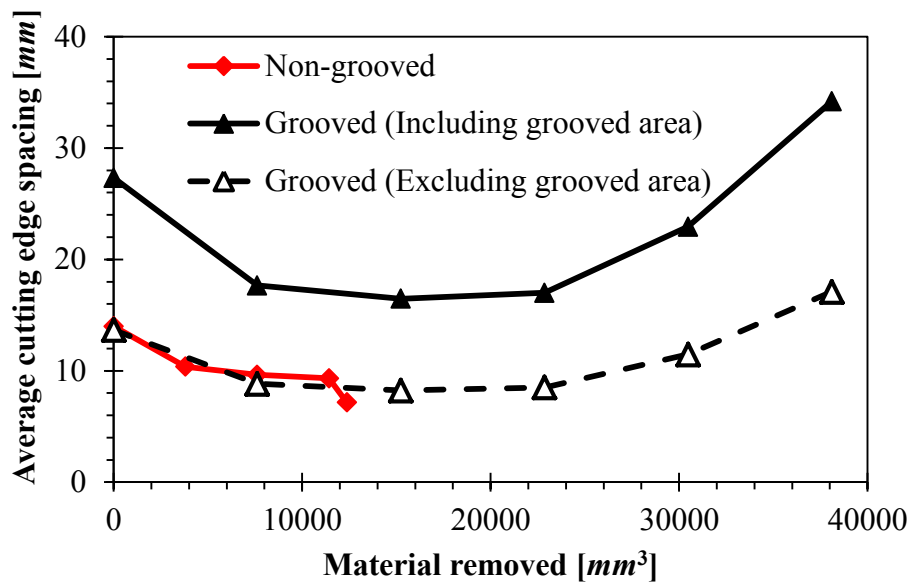
Figure 5.31 Cutting edge spacing comparison for non-grooved and grooved wheels

When looking at non-grooved area only, the spacing between cutting edges was 14.0 and 13.7 *mm* for the non-grooved and grooved wheel, respectively. This similarity is due to fact that the wheels were conditioned using the same parameters. By including the grooved area, the cutting edge spacing for the grooved wheel doubles due to the 50% groove factor. Figure 5.31 also shows that the two measures continue to follow similar trends, until workpiece burn occurred with the non-grooved wheel. At this point the non-grooved cutting edge spacing saw a noticeable decrease. The decrease could be an effect from accelerated attritious wear or workpiece material that was adhered to the wheel could have been measured. The cutting edge spacing of the grooved wheel seems to level off before reaching its failure point. The spacing then increases at a high rate, which agrees with the notion that wheel breakdown is occurring during this period. The grinding wheel once again appeared to last double the duration of the non-grooved wheel before failing.

With the cutting edge spacing known, it is now possible to use Equation (2.2) in order to solve for the uncut chip thickness. Figure 5.32 shows the uncut chip thickness for the top 1 *μm* of the non-grooved and grooved grinding wheels. In order to obtain an accurate representation of the grooved wheel's uncut chip thickness, the grooved area was included in the calculation.
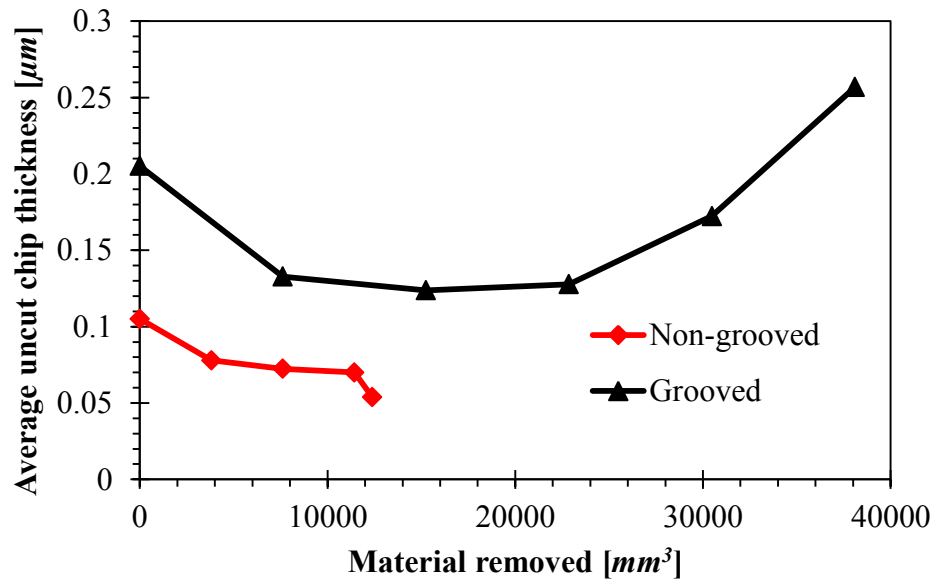
Figure 5.32 Uncut chip thickness comparison for non-grooved and grooved wheel

The uncut chip thickness follows identical trends to the cutting edge spacing for both non-grooved and grooved, which makes sense as it is heavily dependent on the kinematics of the grinding which were the same throughout the experimentation. The uncut chip thickness for the grooved wheel is constantly higher than the non-grooved wheel. Mohamed et al. [58] compared SEM images of the chips formed from both, non-grooved and grooved wheels, and reported that there was an increase in chip size when using the grooved wheel.

It is important to ensure that the information being extracted from the blob analysis agrees with the data measured directly from the grinding experiments. Recalling some noticeable features from the conventional measurements shown in Figure 5.12 to Figure 5.14, the non-grooved wheel steadily increased in power and forces until the workpiece was burnt. The radial and volumetric wear shown in Figure 5.29 and Figure 5.30, showed a steady wear rate until reaching the failure point which agrees with the conventional measures. Figure 5.31 showed that the cutting edge spacing was also decreasing at a steady state before the burn occurred. As for the grooved wheel, the power and force curves leveled off around 20955 mm^3 of removed material. During this period the radial

and volumetric wear measures were showing signs of steady state wear and the cutting edge spacing was levelling off as well. At a removed volume of 30480 mm^3 the power and forces began to fluctuate. This point directly matches the point at which the grinding wheel scanner began to measure significant signs of fracture wear. The radial and volumetric wear plots entered their failure regime and the cutting edge spacing began to increase. The increase in cutting edge spacing leads to larger chip thickness and therefore the cutting forces and power would be expected to lower due to the size effect. At the same time the rubbing and plowing forces would be expected to increase due to the significant decrease in sharp cutting edges, the two effects put together can be used to explain the force and power fluctuations seen. The workpiece surface roughness also increased significantly at precisely 30480 mm^3 of removed material, which is likely another result from the increase in cutting edge spacing measured.

Due to the scanning interval of 8 passes or 7620 mm^3 of removed volume, throughout the blob analysis it appeared as though the grooved grinding wheel was lasting twice as long as the non-grooved. Based on the power and surface roughness measurements however, it appears as though the grooved grinding wheel only began to fail after a removed volume of 29527.5 mm^3, which is roughly 167% greater than the total removed volume the a non-grooved wheel.

The near perfect alignment between noticeable features in the scanner measurements and of the conventional measurements has warranted further investigation with the parameters obtained thus far. The uncut chip incorporates both topographical data as well as the process kinematics and therefore was selected to tie together all aspects of this study. Figure 5.33 shows the conventional force and power measurements plotted as a function of uncut chip thickness.
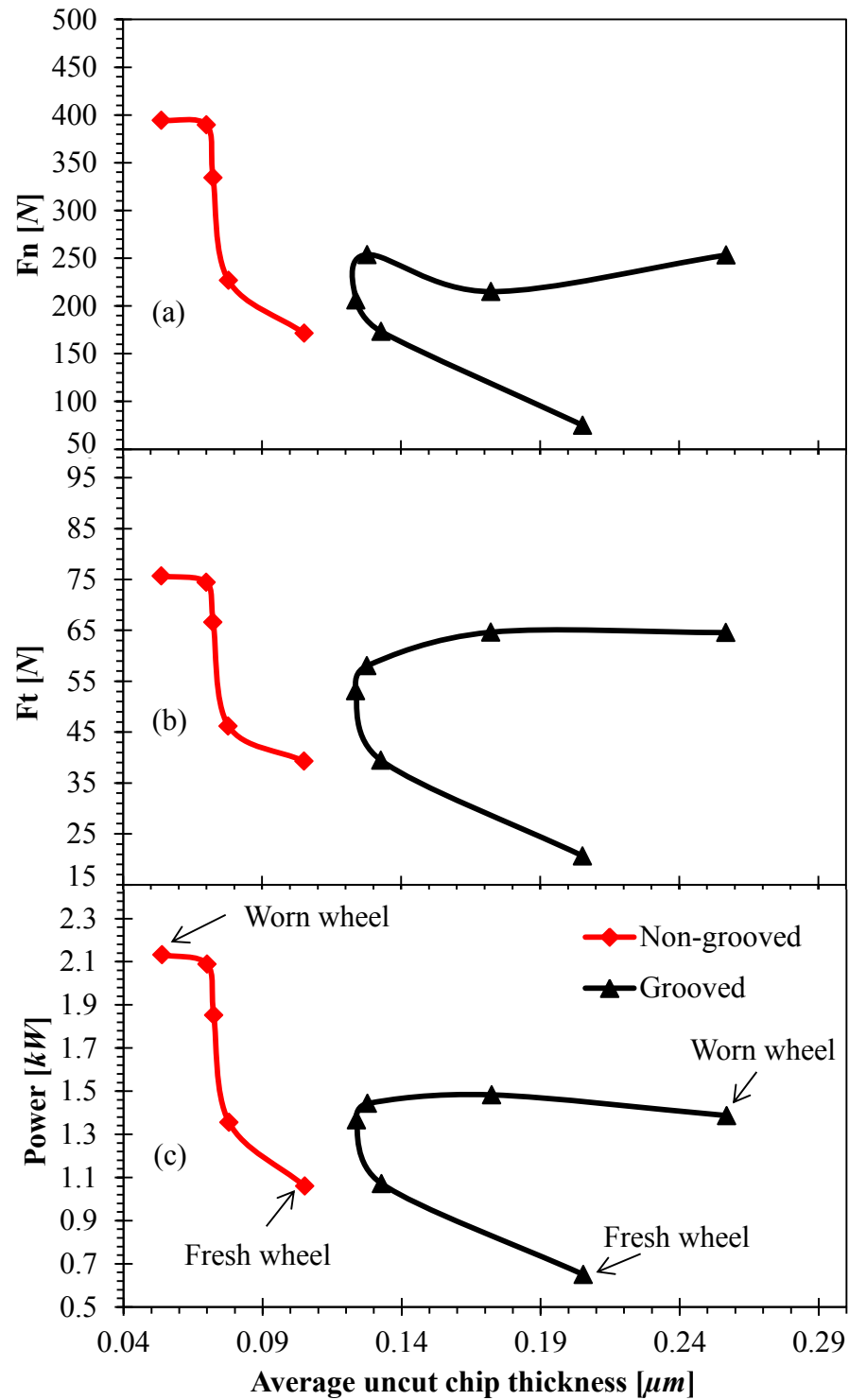
Figure 5.33 (a) Normal force, (b) tangential force and (c) power as functions of uncut chip thickness for non-grooved and grooved wheels.

All three plots in Figure 5.33 show the same general trend of increasing power with a smaller uncut chip thickness. Once the wheels failed however, their trends differed significantly as a result of their failure modes. The non-grooved wheel failed due to workpiece burn which led to further reducing its uncut chip thickness and therefore an increase in forces and power. The grooved wheel broke down, leading to a reversal in the curve. During breakdown the loss of grains increased the uncut chip thickness and the power decreased slightly due to the size effect.

5.5 Summary

This chapter presented experimental results from a wear study of grooved and non-grooved grinding wheels. First, an analysis method developed to extract useful parameters from a scanner measurement was described. The parameters extracted from the scanner measurements were number of particles, average particle width and total area. A series of filters were implemented in order to remove noisy data and confirmed with the use of a digital image. With measurement noise removed, it was possible to reference all scans to the same point by aligning the blob analysis results from unused sections of the scans and applying the same difference to the used sections. This reference allowed for the radial wear of the wheel to be measured which was then used to calculate the amount of volumetric wear that the wheels had incurred. The G-ratios were then calculated to be 10215 and 6849 for the grooved and non-grooved wheels' respectively, during the stable grinding regime. The cutting edge spacing and uncut chip thickness were then calculated from the extracted parameters and it was found that in the non-grooved area of the wheels they were similar during the steady-state wear regimes. Incorporating the groove into the results doubled both the cutting edge spacing and uncut chip thickness due to the 50% groove factor. A comparison of the scanner measurements to the conventional measurements was then performed and there was a very strong agreement between all methods of measurements. The blob analysis was able to detect a significant difference in the extracted parameters at the same point that the conventional measures began to show signs of wheel breakdown. The scanner measurements indicated a 100% increase in the total workpiece material removed. The conventional measurements suggested that the grooved grinding wheel was able to remove 167% more

workpiece material than the non-grooved grinding wheel. This difference was due to the scanning interval. Overall, the grinding wheel scanner was proven to be able to consistently measure the wear of grinding wheels by its exceptional alignment with noticeable traits in the conventional measurements. The near perfect alignment warranted further investigation which was performed by consolidating the conventional measurements with the scanner measurements. By comparing the uncut chip thickness to the consumed power and forces the effect of the wheels failure modes was evident, and the size effect could be seen clearly.

Chapter 6. Conclusion

6.1 Thesis Summary

The first objectives upon beginning this work were to improve the grinding wheel scanner's resolution, reliability, and to design and implement a homing system for the scanner. The resolution was improved by placing an additional encoder on the friction wheel drive motor. By doing so, the resolution of the scanner's x-direction was improved from, a worst case scenario of 26.5 μm to a constant 0.65 μm. The reliability of the scanner was improved by implementing a designated, real-time controller, which sole priority is the control of the scanners components. A vision based homing system was also designed, and using sub-pixel approximation, is able to track the position of the grinding wheel to within 2 μm.

The next objective was to quantify the new system's positional repeatability, and validate its capability to measure the grinding wheel surface. The validation began with a 2D profiles and it was discovered that slippage was occurring in the contact zone of the friction and grinding wheels. A slip compensating algorithm was then written which was able to correct for the slip to within 5.7 μm and 2 μm for the 1200 μm and 130 μm, respectively. These differences confirmed that the algorithm was working to within the sensor resolutions of 4 μm and 1.4 μm for the 1200 μm and 130 μm pens, respectively. Next, 3D scans were taken of a QR code to quantify the positional repeatability of the scanner. It was found that the 1200 μm was able to measure the distance between features in the x and y direction within percent errors of 2.1 and 1.0%, respectively. The repeatability of its area measurements was found to be within 2%. Using the 130 μm pen had a small effect on the x and y distance measurments, resulting in percent errors of 1.3 and 0.8% for the x and y directions. The area measurements improved subtantially with the 130 μm with an error of 0.7%. The QR code analysis also confrimed that the homing system was able to home the within to within standard deviations of 27.6 μm and 19.3 μm in the x and y directions. Finally, by comparing the sizes of features in the scanned measurements to SEM images of the grinding wheel it was found that the feature sizes

were within 11% of each other. By overlaying an SEM image onto a scanned measurement, the near perfect alignment of the two was demonstrated.

The final objective was to use the grinding wheel scanner to investigate the wear of grooved and non-grooved wheels. A wear study was performed and in order to analyze the scanner measurements an analysis method was developed. The analysis method allowed for the monitoring of radial wheel wear, which further led to the volumetric wear. G-ratios of the two wheels were then calculated to be 10215 and 6849 for grooved and non-grooved wheels, respectively. A comparison of the non-grooved portions cutting edge spacing and uncut chip thickness was then performed, and showed noticeable similarities during the steady-state wear regime. By combining the conventional measurements with the scanner measurements using a calculated uncut chip thickness, the effect of the different failure modes was shown and it also allowed for the size effect to be seen.

6.2 Recommendations

The grinding wheel scanner can be used to further strengthen of the link between the grinding process and the wheel topography. The development of a simulation which uses the scanned surface topography would be beneficial in determining the true uncut chip thickness and therefore the depth which should be analyzed. The scanner could be used to investigate the wear of different grinding wheels, the effect of different workpieces and or coolant delivery systems on the wheel, and the effect of process parameters such as depth of cut and feed rate on the wear of the wheel. One further improvement to the scanner which could be implemented is to replace the optical pen's manual stage with an automatically actuated one. This automated stage would ensure the pen is consistently moved to the same standoff distance for each scan, allowing the 130 μm pen to be more effectively implemented into the research. By automatically controlling the stage, profiled grinding wheels could then be measured as well, which would further widen the scope of possible research with this tool.

References

[1] D. M. Marinescu, W. B. Rowe, B. Dimitrov and I. Inasaki, Tribology of Abrasive Machnining Processes, Norwich, NY: William Andrew Inc., 2004.

[2] ANSI Standard B74.13-1990 (R2007), Markings for Identifying Grinding Wheels and Other Bonded Abrasives, New York: Unified Abrasives Manufacturers' Association, 1990.

[3] M. P. Groover, Fundamentals of Modern Manufacturing, Third Edition, Hoboken, NJ: John Wiley & Sons, Inc., 2007.

[4] S. Malkin, Grinding Technology: Theory and applicationsof machining with abrasives, Dearborn, Michigan: Society of Manufacturing Engineers, 1989.

[5] H. Chen, W. B. Rowe, B. Mills and D. R. Allanson, "Analysis and Simulation of the Grinding Process - Part IV: Effects of Wheel Wear," *International Journal of Machine Toold and Manufacturing,* vol. 38, no. 1-2, pp. 41-49, 1998.

[6] S. Malkin and N. H. Cook, "The Wear of Grinding Wheels. Part I, Attritious Wear," *Journal of Engineering for Industry,* vol. 93, pp. 1120-1128, 1971.

[7] S. Malkin and N. H. Cook, "The Wear of Grinding Wheels. Part II - Fracture Wear," *Journal of Engineering for Industry,* vol. 93, pp. 1129-1133, 1971.

[8] H. Yoshikawa, "Fracture Wear of Grinding Wheels," in *Production Engineering Conference*, 1963.

[9] H. Yoshikawa and T. Sata, "Study on Wear of Grinding Wheels," *Journal of Engineering for Industry,* vol. 85, pp. 39-43, 1963.

[10] J. F. G. de Oliveira, R. T. Coelho and C. K. Neto, "Development of an Optical Scanner to Study Wear on the Working Surface of Grinding Wheels," *Machining Science and Technology,* vol. 3, no. 2, pp. 239-253, 1999.

[11] A. T. Nguyen and D. L. Butler, "Correlation of grinding wheel topography and grinding performance: A study from a viewpoint of three-dimensional surface characterisation," *Journal of Materials Processing Technology,* vol. 208, pp. 14-23, 2007.

[12] D. L. Butler, L. A. Blunt, B. K. See, J. A. Webster and K. J. Stout, "The characterisation of grinding wheels using 3D surface measurement techniques," *Journal of Materials Processing Technology,* vol. 127, pp. 234-237, 2002.

[13] D. L. Butler, "The Topographic Characterisation of Grinding Wheels- A Proposed Measurement Strategy," *Advanced Materials Research,* vol. 1017, pp. 686-691, 2014.

[14] K. Nadolny, W. Sienicki and M. Wojtewicz, "The effect upon the grinding wheel active surface condition when impregnating with non-metallic elements during internal cylindrical grinding of titanium," *Unknown.*

[15] J. Xie, J. Xu, Y. Tang and J. Tamaki, "3D graphical evaluation of micron-scale protrusion topography of diamond," *International Journal of Machine Tools & Manufacture,* vol. 48, pp. 1254-1260, 2008.

[16] M. C. Shaw and R. Komanduri, "The Role of Stylus Curvature in grinding Wheel Surface Characterization," *CIRP Annals,* vol. 25, pp. 139-141, 1977.

[17] P. M. Lonardo, H. Trumpold and L. De Chiffre, "Progress in 3D Microtopography Characterization," *CIRP Annal,* vol. 45, pp. 589-598, 1996.

[18] K. Syoji, L. Zhou and S. Matsui, "Studies on truing and dressing of diamond wheels (1st report). the measurement of protrusion height of abrasive grains by using a stereo pair and the influence of protrusion height on grinding performance," *Bulletin of the Japan Society of Precision Engineering,* vol. 24, p. 124, 1990.

[19] W. R. Backer, E. R. Marshall and M. C. Shaw, "The Size Effect in Metal Cutting," *Trans. ASME,* vol. 74, p. 61, 1952.

[20] S. G. Red'ko, "The Active Grits on Grinding Wheels," *Machines and Tooling,* vol. 31, no. 12, p. 11, 1960.

[21] T. W. Liao, K. Li, S. B. McSpadden, Jr and L. J. O'Rourke, "Wear of diamond wheels in creep-feed grinding of ceramic materials I. Mechanisms," *Wear,* vol. 211, pp. 94-103, 1997.

[22] K. Nakayama, "Grinding Wheel Geometry," in *Proceedings of the International grinding Conference*, Pittsburgh, 1972.

[23] J. Verkerk, "Final report concering CIRP Cooperative work on the characterization of grinding wheel topography," *Annals of the CIRP,* vol. 26.2, pp. 385-395, 1977.

[24] A. M. Besuyen and J. Verkerk, "Scanning Electron Microscope Observation of Grinding Grains," *Annals of CIRP,* vol. 21.1, pp. 65-66, 1971.

[25] Y. Matsuno, H. Yamada, M. Harada and A. Kobayashi, "The Microtopography of the Grinding Wheel Surface with SEM," *Annals of the CIRP,* vol. 24.1, pp. 237-242, 1975.

[26] H. Tsuwa and H. Yasui, "Micro-structure of Dressed Abrasive Cutting Edges," in *Proceeding of the International Grinding Conference*, Pittsburgh, 1982.

[27] W. Kaplonek and K. Nadolny, "Assessment of the grinding wheel active surface condition using SEM and image analysis techniques," *Journal of the Brazilian Society of Mechanical Sciences and Engineering,* vol. 35, pp. 207-215, 2013.

[28] O. Tuovinen, T. Bjorkqvist and P. Fardim, "Reconstruction and characterization of grinding wheel and grit topography from scanning electron microscopy stereo micrographs with digital photogrammetry," *O Papel,* vol. 74, no. 4, pp. 51-58, 2013.

[29] S. LaChance, A. Warkentin and R. Bauer, "Development of an Automated System for Measuring Grinding Wheel Wear Flats," *Journal of Manufacturing Systems,* vol. 22, no. 2, 2003.

[30] Z. Feng and X. Chen, "Image processing of grinding wheel surface," *International Journal of Advanced Manufacturing Technology,* vol. 32, pp. 27-33, 2007.

[31] K. Fathima, A. Senthil Kumar, M. Rahman and H. S. Lim, "A study on wear mechanism and wear reduction strategies in grinding wheels used for ELID grinding," *Wear,* vol. 254, pp. 1247-1255, 2003.

[32] J. Xie, J. Xu, Y. Tang and J. Tamaki, "3D graphical evaluation of micron-scale protrusion topography of diamond grinding wheel," *International Journal of Machine Tools & Manufacture,* vol. 49, pp. 1254-1260, 2008.

[33] R. L. Hecker, I. M. Ramoneda and S. Y. Liang, "Analysis of Wheel Topography and Grit Force for Grinding Process Modeling," *Journal of Manufacturing Processes,* vol. 5, no. 1, pp. 13-23, 2003.

[34] Q. Zhao and B. Guo, "Ultra-precision grinding of optical glasses using mono-layer nickel electroplated coarse-grained diamond wheels. Part 1: ELID assisted precision conditioning of grinding wheels," *Precision Engineering,* vol. 39, pp. 56-66, 2015.

[35] Q. Zhao and B. Guo, "Ultra-precision grinding of optical glasses using mono-layer nickel electroplated coarse-grained diamond wheels. Part 2: Investigation of profile and surface grinding," *Precision Engineering,* vol. 39, pp. 67-78, 2015.

[36] L. Yan, Y. M. Rong, F. Jiang and Z. X. Zhou, "Three-dimension surface characterization of grinding wheel using white light interferometer," *Internation Journal of Advanced Manufacturing Processes,* vol. 55, no. 1, pp. 133-141, 2011.

[37] A. M. Tahvilian, Z. Liu, H. Champliaud, B. Hazel and M. Legace, "Characterization of grinding wheel grain topography under different robotic grinding conditions using confocal microscope," *Internation Journal of Advanced Manufacturing Processes,* vol. 80, no. 5, pp. 1159-1171, 2015.

[38] A. Darafon, A. Warkentin and R. Bauer, "Characterization o fgrinding wheel topography using a white chromatic sensor," *International Journal of Machine Tools & Manufacture,* pp. 22-31, 2013.

[39] T. W. Liao, F. Tang, J. Qu and P. J. Blau, "Grinding wheel condition monitoring with boosted minimum distance classifiers," *Mechanical Systems and Signal Processing,* vol. 22, pp. 217-232, 2008.

[40] W. L. Weingaertner and A. L. Boaron, "A Quick-Test Method to Determine the Grinding Wheel Topography Based on Acoustic Emission," *Advanced Materials Research,* vol. 325, pp. 282-286, 2011.

[41] STIL, "Non-contact "point" sensors," [Online]. Available: http://www.stilsa.com/catalog2/pdf/STILSA_Initial_CCS_CHR.pdf. [Accessed 06 2015].

[42] AEOUSA, "White Light Axial Chromatism Sensor Technology," 2015. [Online]. Available: http://www.aeousa.com/#!confocal-chromatic-sensing/c1w2q. [Accessed 06 2015].

[43] N. M. D. Lab, "Rotary Encoder," 2 2 2010. [Online]. Available: http://hades.mech.northwestern.edu/index.php/Rotary_Encoder. [Accessed 6 2015].

[44] Edmund Optics Inc., "Imaging Resource Guide," 2014. [Online]. Available: http://www.edmundoptics.com/capabilities/imaging-optics/imaging-resource-guide/. [Accessed 08 2014].

[45] National Instruments, "Definition of an Edge," 06 2011. [Online]. Available: http://zone.ni.com/reference/en-XX/help/372916L-01/nivisionconcepts/edge_detection_concepts/. [Accessed 2014].

[46] National Instruments, "NI LabVIEW for CompactRIO Developer's Guide," National Instruments, 2014. [Online].

[47] K. Nakayama, J. Takagi and T. Abe, "Grinding wheel with helical grooves—an attempt to improve the grinding performance," *Manufacturing Technology, 27th General Assembly of CIRP,* pp. 133-138, 1977.

[48] S. Okuyama, Y. Nakamura and S. Kawamura, "Cooling action of grinding fluid in shallow grinding," *International Journal of Machine Tools and Manufacture,* vol. 33, pp. 13-23, 1993.

[49] A.-M. O. Mohamed, R. Bauer and A. Warkentin, "Application of shallow circumferential grooved wheels to creep-feed grinding," *Journal of Materials Processing Technology,* pp. 700-706, 2013.

[50] A.-M. O. Mohamed, R. Bauer and A. Warkentin, "A novel method for grooving and re-grooving aluminum oxide," *The International Journal of Advanced Manufacturing Technology,* vol. 73, no. 5, pp. 715-725, 2014.

[51] J. Verkerk, "Slotted wheels to avoid cracks in precision grinding," in *Proc. Annu. Abrasive Engineering Society Conference/Exhibition*, Pittsburgh, Pennsylvania, 1979.

[52] J. Davis, "ASM Internation Handbook Committee," in *ASM Handbook Volume 16*, Machining, ASM International, 2010.

[53] N. Cook, "Tool Wear and Tool Life," *Journal of Engineering for Industry,* vol. 95, no. 4, pp. 931-938, 1973.

[54] L. D. Beju, P. D. Brindasu and S. Vulc, "Grinding Tungsten Carbide Sued for Manufacturing Gun Drills," *Jounal of Mechanical Engineering,* vol. 61, no. 10, pp. 571-582, 2015.

[55] S. B. McSpadden Jr. and G. R. Hughes, "Oak Ridge National Laboratory," 2001. [Online]. Available: http://web.ornl.gov/~webworks/cppr/y2001/pres/116758.pdf. [Accessed 23 11 2015].

[56] M. Izumi and A. Ochi, " American Society for Precision," 2004. [Online]. Available: http://www.aspe.net/publications/Annual_2004/POSTERS/5PROC/1GRIND/1573. PDF. [Accessed 11 23 2015].

[57] W. R. Backer and E. J. Krabacher, "New Techniques in Metal-cutting Research," *ASME,* vol. 76, p. 1497, 1956.

[58] A.-M. O. Mohamed, R. Bauer and A. Warkentin, "Uncut chip thickness and coolant delivery effects on the performance of circumferentially grooved grinding wheels," *International Journal of Advanced Manufacturing Technology,* pp. 1-10, 2015.